Structural Correlation and Magnetic Effects in Ferecrystalline Materials

I n a u g u r a l - D i s s e r t a t i o n
zur
Erlangung des Doktorgrades
der Mathematisch-Naturwissenschaftlichen Fakultät
der Universität zu Köln

vorgelegt von
Maria Katharina Hentschel
aus Köln

Köln, 2018

Berichterstatter/in: Dr. Sabrina Disch
Prof. Dr. Uwe Ruschewitz

Tag der letzten mündlichen Prüfung:14.01.2019

"What are the three most important rules of the chemist?"
This I knew from Ben. "Label clearly. Measure twice. Eat elsewhere."
Patrick Rothfuss, The Name of the Wind

Acknowledgements

I would like to thank all the people that supported and helped me during this work and by this made it possible to produce this thesis.

First of all I would like to thank my advisor Dr. Sabrina Disch for the continuous support of my Ph.D study and research, for her patience, motivation, enthusiasm, and immense knowledge.

I would like to thank Prof. Dr. David C. Johnson of the University of Oregon for giving me the opportunity to work in his research laboratory, as well as the advice and support he has provided not only during my stays in Eugene but during my whole Ph.D study.

I would also like to thank Prof Dr. Uwe Ruschewitz for being my co advisor and his constructive comments during the seminars.

Prof. Dr. Axel G. Griesbeck for being the chair of my thesis committee.

I thank Dr. Stefan Roitsch for providing assistance with my ER-C proposal, documents and being our contact while Sabrina was on maternity leave. I would also like to thank him for being a member of my thesis committee.

Special thanks to my colleagues Dominique Dresen, Dominika Zákutná, Yannic Falke and Flore Mees for their assistance at beamtimes, helpful suggestions, discussion, proof reading, code, coffee and Kinder chocolate. I would like to thank especially Dominique Dresen for the time and effort he put into programming code for data reduction and analysis. Thanks for all the fun we have had in the last four years it was a pleasure working with you.

I would like to thank the whole Johnson group for friendly reception in the group. Special thanks to Dr. Suzannah R. Wood, Dr. Sage R. Bauers for their assistance during beamtimes and for making my time in Eugene entertaining and educational. I would like to acknowledge Dr. Jeffrey Ditto and Dr. Devin R. Merrill for their work in transmission electron microscopy at the Center for Advanced Materials Characterization in Oregon (CAMCOR) and the Pacific Northwest National Laboratory (PNNL). I would also like to acknowledge Dr. Suzannah R. Wood, Dr. Devin R. Merrill, Dr. Matthias Falmbigl and Omar K. Hite for providing the samples used in chapter 4.

I would like to thank the work group of Prof. Annette M. Schmidt for their support and friendship.

Special thanks go out PD Dr. Oleg Petracic, Dr. Xiao Sun, Dr. Markus Waschk and Annika Stellhorn at the Jülich Centre for Neutron Science (JCNS) for their assistance, discussions and expertise while using the SQUID magnetometer.

I would like to thank to Dr. Roberto Felici, Dr. Willem G. Onderwaater and Dr. Francesco Carla for providing assistance in using beamline ID03 at the European Synchrotron Radiation Facility (ESRF).

Furthermore, I would like to thank Dr. Stefan Mattauch and Dr. Alexandros Koutsiompas from the Jülich Centre for Neutron Science (JCNS) at Heinz Maier-Leibnitz Zentrum for their assistance with polarized neutron reflectometry measurements at the MARIA instrument.

Dr. Evguenia Karapetrova from the Advanced Photon Source for her assistance in X-ray diffraction analyses at Beamline BM-33-C.

Dr. Andras Kovacs from the Ernst Ruska-Centre at Jülich Centre for Neutron Science (JCNS) for his work in transmission electron microscopy.

I would like to thank the German Excellence Initiative for founding my research.

Finally, I must express my very profound gratitude to my family, Elke, Bernhard, Erika and Alexander and my partner Christoph for providing me with unfailing support and continuous encouragement throughout my years of study and through the process of researching and writing this thesis. To them I dedicate this thesis. This accomplishment would not have been possible without them. Thank you.

Abstract

Nanolaminates are an excellent model system to study the correlation of structural and magnetic disorder in magnetic nanomaterials in one dimension because they offer precise control over the structure on a sub-Ångström length scale. Ferecrystals are nanolaminate compounds of the misfit-layer family with the general formula $[(MSe)_{1+\delta}]_m(TX_2)_n$ (M = Pb, Sn, Bi, or rare earth metal; X = S, Se, Te; T = transition metal) where the individual constituents are stacked and rotationally disordered along the c-axis. Since m and n are tunable, they are excellent candidates to systematically investigate surface and finite size-induced structural distortions in nanomaterials.

Detailed knowledge of the atomic structure and the structural correlation of nanomaterials is essential to predict and explain structure-property relations. Reciprocal space maps revealed interlayer correlations in ferecrystals with the structure $[(MSe)_{1+\delta}]_1(TSe_2)_1$ opposed to the typical observed turbostratic disorder. Those results suggest that preferential nucleation and layer alignment during nucleation occur in ferecrystals and show that, at least for some 1:1 ferecrystals, ordered domains are present.

Moreover, a new set of ferecrystalline materials with the general structure $[(Cu_xCr_ySe_z)_{1+\delta}](NbSe_2)_n$ has been prepared. By varying the annealing temperature of these compounds, it was possible to form four different heterostructures. This is the first set of ferecrystals which gives access to multiple heterostructures by varying the annealing temperature. The different heterostructures have been analyzed by out-of-plane and in-plane diffraction as well as STEM/EDX imaging.

Rietveld refinements have been used with different starting models to gain better understanding of the structure in the $Cu_xCr_ySe_z$ layer. The $Cu_xCr_ySe_z$ layer was best described by a symmetric variation of $CuCrSe_2$ structure. Also the effect of the annealing temperature on the atomic layering and site occupancies has also been investigated via Rietveld refinement.

By replacing traditional MX rock salt with a $Cu_xCr_ySe_z$ layer, the first magnetic ferecrystals have been prepared. The $Cu_xCr_ySe_z$ layer serves as the magnetic constituent and is separated by layers of a nonmagnetic 'spacer' constituent ($NbSe_2$). Macroscopic magnetization measurements revealed a significant magnetic moment despite the only small magnetic volume. By tuning the number of spacer layers, we can systematically alter the magnetic properties of the ferecrystals and investigate the magnetic interlayer coupling with n.

Kurzzusammenfassung

Nanolaminate sind ein exzellentes Modellsystem, um Korrelationen von struktureller und magnetischer Unordnung in eindimensionalen magnetischen Nanolaminaten zu untersuchen, da sie eine präzise Kontrolle der Struktur auf atomarer Größenordnung ermöglichen. Ferekristalle sind Nanolaminate aus der Familie der Misfit-Verbindungen und haben die allgemeine Strukturformel $[(MX)_{1+\delta}]_m(TX_2)_n$ (M = Pb, Sn, Bi, oder Metall der seltenen Erden; X = S, Se, Te; T = Übergangsmetall). Die einzelnen Bestandteile MX und TX_2 sind entlang der c-Achse übereinander angeordnet, jedoch in der Ebene turbostratisch verdreht. Da m und n beliebig variiert werden können, sind Ferekristalle ein exzellenter Kandidat für systematische Untersuchungen von Oberflächeneffekten sowie strukturellen Fehlordnungen aufgrund von Effekten der begrenzten Ausdehnung in Nanomaterialien.

Detaillierte Kenntnisse über die atomare Struktur und strukturelle Wechselwirkungen sind ein wichtiger Schritt, um strukturell bedingte Eigenschaften zu erklären und vorherzusagen. Reziproke Gitterkarten zeigen für $[(MSe)_{1+\delta}]_1(TSe_2)_1$ strukturelle Wechselwirkungen zwischen den Schichten, was im Gegensatz zu der normalerweise beobachteten turbostratischen Verdrehung steht. Diese Ergebnisse deuten an, dass eine bevorzugte Nukleation und eine Ausrichtung der Schichten während der Nukleation stattfinden und zeigen, dass zumindest in manchen 1:1 Ferekristallen geordnete Domänen vorhanden sind.

Ein neues Set ferekristalliner Materialen mit der allgemeinen Strukturformel $[(Cu_xCr_ySe_z)_{1+\delta}]_1(NbSe_2)_n$ wurde erfolgreich hergestellt. Durch Variation der Glühtemperatur ist es möglich, vier verschiedenen Heterostrukturen zu bilden. Dies sind die ersten Ferekristalle, die durch Variation der Glühtemperatur verschiedene Heterostrukturen bilden. Die verschiedenen Heterostrukturen wurden mittels Röntgendiffraktion in und außerhalb der Ebene sowie durch STEM/EDX Abbildungen untersucht.

Verschiedene Startmodelle wurden genutzt, um mittels Rietveld-Methode ein besseres Verständnis über die Struktur in der $Cu_xCr_ySe_z$-Schicht zu erhalten. $Cu_xCr_ySe_z$ lässt sich am besten durch eine symmetrische Variation der $CuCrSe_2$ Struktur beschreiben. Der Einfluss der Glühtemperatur auf die atomare Struktur und Besetzung wurde ebenfalls mittels Rietveld-Methode untersucht.

Durch Ersetzen der Kochsalzverbindung MX mit einer $Cu_xCr_ySe_z$-Schicht konnten die ersten magnetischen Ferekristalle hergestellt werden. Hierbei dient die $Cu_xCr_ySe_z$-

Schicht als magnetische Komponente und wird durch eine nichtmagnetische Trennschicht ($NbSe_2$) separiert. Makroskopische Magnetisierungsmessungen zeigen ein signifikantes magnetisches Moment, obwohl die Proben ein sehr kleines magnetisches Volumen besitzen. Durch Variation der Trennschicht Wiederholungseinheit n konnte eine systematische Variation der magnetischen Eigenschaften erzielt werden. Der Zusammenhang von magnetischen Wechselwirkungen zwischen den Schichten und n wurde untersucht.

Contents

Abstract **III**

Kurzzusammenfassung **V**

1. Introduction **2**

2. Scientific aims **4**

3. Theory **6**

3.1. Ferecrystals 6
3.2. MER method 7
3.3. Crystal structure of $CuCr_2Se_4$ 9
3.4. Structure of transition metal dichalcogenides 11
3.5. X-ray and neutron reflectometry 13
3.5.1. Polarized neutron reflectometry 18

4. Interlayer correlations in 1:1 ferecrystals **20**

4.1. Introduction and aims 20
4.2. Evidence of interlayer correlation 20
4.3. Higher order reflections 25
4.4. Reciprocal space maps along MSe and TSe_2 reflection series 26
4.5. Potential candidates for interlayer correlations 29
4.6. Summary 34

5. $[(Cu_xCr_ySe_z)_{1+\delta}]_1(NbSe_2)_3$ ferecrystals **36**

5.1. Introduction and aims 36
5.2. Sample calibration and preparation 36
5.3. Annealing study 39
5.4. Heterostructure formation in a broader set of samples 42
5.5. Structural investigation of the in-plane structure 46
5.6. Scanning transmission electron microscopy 48
5.7. Summary 53

6. Structural investigation of the $Cu_xCr_ySe_z$ constituent **56**

6.1. Introduction and aim 56
6.2. Comparison of different models for the $Cu_xCr_ySe_z$ layer 56

6.3. Structural differences in heterostructure A and B 63
6.4. Preparation of $[(Cu_xCr_ySe_z)_{0.5}]_{1+\delta}(NbSe_2)_3$ 65
6.5. Structure of $[(Cu_xCr_ySe_z)_{0.5}]_{1+\delta}(NbSe_2)_3$ 66
6.6. Summary 68

7. $[(Cu_xCr_ySe_z)_{1+\delta}]_1[NbSe_2]_n$ ferecrystals 70
7.1. Introduction and aims 70
7.2. Sample preparation 70
7.3. Structural investigation of set 3 with $n = 1$ - 5 70
7.4. Magnetic Properties of $CuCr_2Se_4$, $CuCrSe_2$, and $CrSe_2$ 73
7.5. Macroscopic magnetization 75
7.6. Polarized neutron reflectometry 81
7.7. Summary 83

8. Conclusion and summary 86

9. Experimental section 88
9.1. Sample preparation 88
9.2. Instruments 88
9.2.1. Bruker AXS D8 88
9.2.2. ID03 89
9.2.3. BM-33-C 89
9.2.4. Electron probe microanalyzer 90
9.2.5. XRF 90
9.2.6. MARIA 90
9.2.7. STEM 91
9.2.8. STEM and EDX at PNNL 91
9.2.9. STEM and EDX at ER-C 91
9.2.10. SQUID 92
9.3. Programs 93
9.3.1. Layer thickness 93
9.3.2. aps slicereduce 93
9.3.3. Le Bail fits and Rietveld refinements 93
9.3.4. Fits 93
9.3.5. Refinement of X-ray reflectivity data 94
9.3.6. Diamond 94

Appendix **96**

A. Interlayer correlations in 1:1 ferecrystals **96**
A.1. Le Bail and Rietveld refinement 96
A.2. Reciprocal space maps and Gaussian fits 102
A.3. X-ray diffraction patterns of ferecrystals with m, n $\neq$ 1 104

B. $[(Cu_xCr_ySe_z)_{1+\delta}]_1(NbSe_2)_3$ ferecrystals **106**
B.1. Total thickness and c-lattice parameter of the 1:3 samples 106
B.2. Le Bail fit of $hk0$ data 107
B.3. XRF data of 1:3 data 109

C. Structural investigation of the $Cu_xCr_ySe_z$ constituent **110**
C.1. Rietveld refinement of 1:2 sample of set 3 annealed at 350 °C 110
C.2. Le Bail fit and Rietveld refinement of $00l$ data of 1:3 samples of set 3 . 113
C.3. Le Bail fit and Rietveld refinement of $00l$ data of sample 6 114
C.4. Le Bail fit of $hk0$ data of 6 116

D. $[(Cu_xCr_ySe_z)_{1+\delta}]_1[NbSe_2]_n$ ferecrystals **118**
D.1. c-lattice parameters 118
D.2. Le Bail fit of $hk0$ data 119
D.3. XRF data of 1:n data 125

E. Rebinning algorithm of aps slicereduce **126**

F. Abbreviations **140**

References **144**

Eidesstattliche Erklärung **158**

1. Introduction

Thin films with nanosclae thickness have already been used in ancient Egypt for decorative coatings. They prepared leaf gold with 100 - 300 nm thickness to coat, for example, wood, papyrus, and metal objects.[1] In 1903, Emil Broch handed in a patent for a transparent mirror using a thin metal film.[2] Nowadays thin metal films are used to give materials a metal like appearance. Besides decorative coatings, thin films are usually used to modify surfaces and improve the properties of a substrate.[3] Mechanical properties like the hardness can be improved with coatings of diamond like layers.[4] Whereas thin film with a high hydrophilicity has an anti-fogging effect on the substrate.[5]

In optical lenses, multiple alterations of the properties like low reflectance, physical durability, and high transmission are desired. These are achieved by stacking multiple thin films into a multilayer system.[6] Multilayered nano films made of two or more materials are also called nanolaminates. Nanolaminates offer a large structural diversity and with that many properties that are not accessible with the corresponding bulk materials.[7] Their improved or new chemical and physical properties make them potential materials for optical and electrical devices like X-ray optics,[8,9] memory storage (thin film magnetic recording media),[10–12] energy storage,[13,14] gas,[15,16] and moister[17] diffusion barrier.

The individual layer thickness ranges between few Å and several tens of nm.[7] To control and modify the properties of nanolaminates, a precise control of layer thickness, composition, and crystal structure is necessary. The thickness of the films influences properties like catalytic activity, gas absorption, and diffusion. In optoelectronic thin films, a high crystallinity is essential for optimal performance of the devices.[18]

Magnetic nanomaterials are intensely investigated with fundamental as well as technological aspects due to their potential applications in catalysis, information technology, and medical applications.[19–22] Their unique physical properties, including enhanced magnetic anisotropies and superparamagnetism, are closely related to finite size effects induced by the material surface.[20] The nanoparticle magnetization is related to structural disorder leading to spin disorder, not only at the surface but also in the core of magnetic nanoparticles.[23]

The modulated elemental reactants method (MER),[24–26] established by Johnson *et al.*, enables the preparation of atomic scale precise films. The composition of prepared precursors is close to the desired product reducing the diffusion length and enabling the production of products that are kinetically stabilized.[27] This enables the pro-

duction of heterostructures that are not accessible by usual inorganic synthesis.[28] Ceder *et al.* proved, via the data-mined ionic substitution algorithm,[29] that besides the observed polymorphs there are more than 10 potential polymorphs in rock salt compounds.[30] The low diffusion ranges and annealing temperatures in the MER method have the potential to access various local free-energy minima. Therefore, ferecrystalline materials prepared by the MER method are ideal systems to prepare new heterostructures.

This work aims to investigate various multilayered materials prepared by the MER method and to prepare the first magnetic ferecrystals. The effect of correlation, stacking, composition, and annealing condition on the crystal structure and magnetic properties is the main object of this thesis.

2. Scientific aims

The present work is structured in four chapters. In the first part, the interlayer correlations in 1:1 ferecrystals are studied by reciprocal space mapping. Samples with $m \neq n \neq 1$ are analysed to find the origin of the interlayer registrations. Ferecrystals are generally rotationally disordered in plane.[31,32] In contrast to that, recently studied $m = n = 1$ ferecrystals indicate directionally dependent interlayer registration.[33] A detailed analysis of the structure by in-plane and out of-plane diffraction is provided.

The second part of this work focuses on $[(Cu_xCr_ySe_z)_{1+\delta}]_1(NbSe_2)_3$ ferecrystals. Johnson *et al.* showed that $CuCr_2Se_4$ thin films can be prepared by the MER method. New ferecrystalline materials were prepared by replacing the rock salt MX with $CuCr_2Se_4$ and inserting $NbSe_2$ as paramagnetic spacer. Here, a number of precursors were prepared with $n = 3$ $[(Cu_xCr_ySe_z)_{1+\delta}]_1(NbSe_2)_3$ to probe the potential formation of different heterostructures. Samples with different elemental composition of the $Cu_xCr_ySe_z$ layer were prepared. The elemental compositions of the different heterostructures are investigated by XRF. The effect of annealing time and temperature on the formation of different heterostructures is studied by in-plane and out of plane diffraction as well as STEM-EDX.

The objective of the third part is to solve the atomic layering in the $Cu_xCr_ySe_z$ layer. Rietveld refinements using three potential atomic arrangements as starting models were performed. Which model is appropriate to describe the data, will be discussed. In a second step, the derived model is used to determine the change in structure by decreasing the annealing temperature from 400 to 350 °C.

In the fourth part, the effect of the magnetic layer separation in $[(Cu_xCr_ySe_z)_{1+\delta}]_1(NbSe_2)_n$ with $n = 1$ - 5 is studied. The systematic variation of n provides the opportunity to study the impact of n on the structure and magnetic interlayer interactions. First, a detailed analysis of the systematic change in structure with n by out of-plane and in-plane diffraction is provided. The effect of n on the magnetic properties of $Cu_xCr_ySe_z$ has been analyzed by temperature dependent magnetic susceptibility measurements, field dependent magnetization, and polarized neutron reflectometry.

3. Theory

3.1. Ferecrystals

Misfit layer compounds (MLC) are thermodynamically stable nano laminates of rock salt materials and dichalcogenides with the general structure $[(MSe)_{1+\delta}]_m(TSe_2)_n$ with M = Pb, Sn, Bi, or rare earth metal; X = S, Se, Te; T = transition metal, δ the misfit parameter (Figure 3.1, left).[34] They are usually prepared in high temperature synthesis, making only energetically favourable products (m, n = 1 - 3) accessible. The c-axis of the multilayered material is normal to the constituent layers. The layers are aligned along the b-axis and do not have a commensurate a-axis, yielding a strained material with a complex superlattice structure. The incommensurate in-plane structure leads to a difference in in-plane packing density, which is given by the misfit parameters δ. Due to the termination of the 3D rock salt structure, a puckering along $(00l)$ is observed.[35]

The stability of MLC is not yet understood as usually an alloy material would be expected to be more stable. There are three different theories explaining the stability of MLCs. The charge transfer between the constituent layers might result in ionic interaction.[36–38] Another possibility is that interlayer covalent bonds are the source of the high stability.[39–41] *Ab initio* electronic structure calculations showed that nonstoichiometric substitution of Ta into the PbS layer have a stabilizing effect.[42]

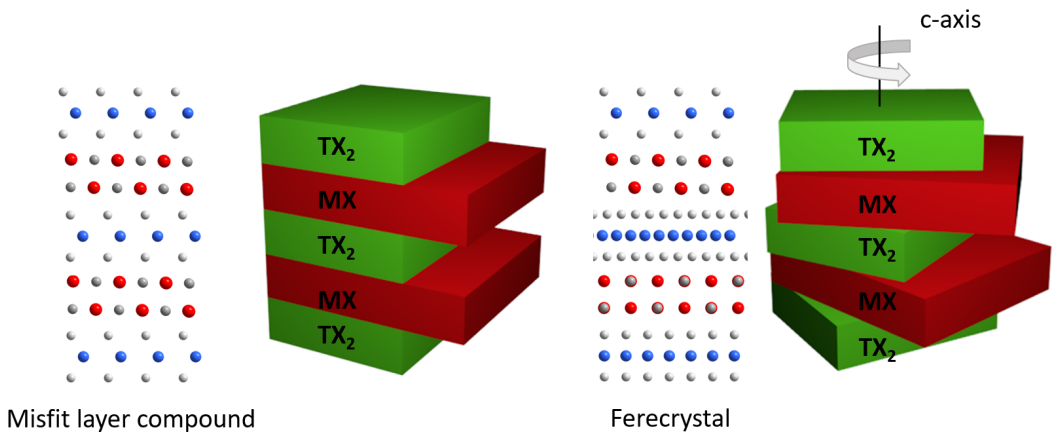

Figure 3.1: Crystal structure of a MLC (left) and ferecrystal (right) with a schematic representation of the layering.

Ferecrystals are MLC which are rotational disordered in-plane but like normal MLC

stacked along the c-axis (Figure 3.1).[28,43] Due to the rotational disorder, the materials lack a 3D crystallinity and therefore are called ferecrystals (named after '*fere*' lat. for '*almost*'). Ferecrystals are prepared by the modulated elemental reactant (MER) method (chapter 3.2) and make a vast variation of m and n accessible.[20,28,44] The binary layers are structurally non-interacting (*i.e.*, epitaxial strain-free) and thus can be regarded as individual nanostructures,[45] whereas their coherent stacking enables application of electron microscopy and diffraction techniques towards investigation of their structural profile. Due to the preferred orientation along the c-axis, X-ray diffraction perpendicular to the film gives exclusively $(00l)$ reflections and allows the determination of the c-lattice parameter. In-plane diffraction of ferecrystals give exclusive $(hk0)$ reflections of the two constituent phases because of the turbostratic disorder.

3.2. MER method

Ferecrystalline materials are prepared by a physical vapour deposition (PVD) named modulated elemental reactant (MER) method[26,44] using a custom-built physical vapour deposition chamber by *Thermionic*.[25] A schematic sketch of the used chamber can be seen in Figure 3.2.

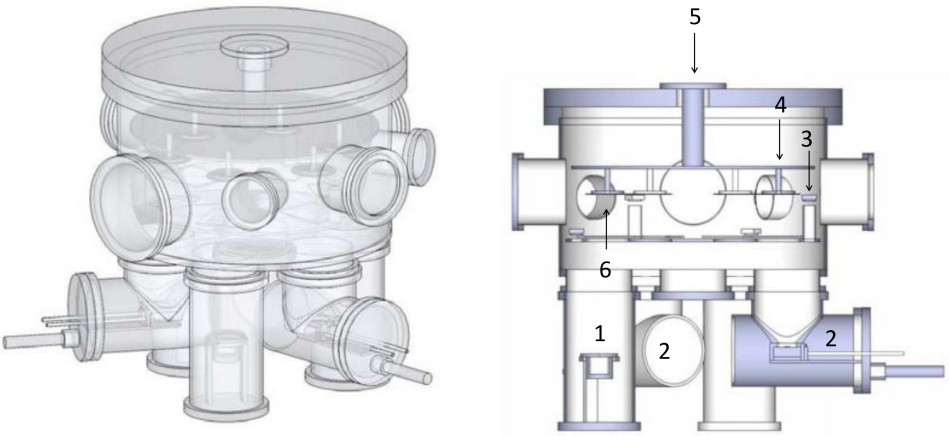

Figure 3.2: Schematic representation of the deposition chamber used. Se effusion cell (1), electron guns (2), crystal monitor (3), sample carousel (4), motor (5) and sample (6). (Modified from M. Anderson, University of Oregon, 2011.)[46]

The chamber is operated with a pressure of $7{\cdot}10^{-5}$ to $7{\cdot}10^{-6}$ Pa which is achieved by a cryogenic pump. The selenium source material is evaporated with an effusion cell, chromium, niobium, and copper are evaporated with electron guns (1 and 2 in Figure 3.2). For chromium a bending magnet raster is used to expand the lifetime of the source material as chromium does not melt but sublimates. Therefore the electron

beam creates a hole in the source material. The choice of the source form has a large impact on the reproducibility of the chromium samples. A good source material requires a smooth surface and has to be slightly convex in shape. (100) silicon can be used as substrate and is placed in a motorized carousel which can be rotated above the sources (4 and 6 in Figure 3.2). Pneumatic shutters are used as a physical barrier between source and substrate, (Figure 3.3). With the aid of quartz micro balances (crystal monitor) (3 in Figure 3.2) the deposition rate is determined. Thickness values which are monitored by the crystal monitor are not accurate Å values and therefore are referred to as Fåkestroms (Få). The rates are usually in the range of 0.2 - 0.5 Få. The crystal monitor (3 in Figure 3.2) and the substrate (6 in Figure 3.2) can not have the same orientation to the source (1 and 2 in Figure 3.2). These geometry variations result in different amounts of atoms hitting the substrate than the crystal monitor and are represented by the tooling factor. By keeping a constant deposition rate and controlling the opening times of the shutters, the amount of deposited material can be controlled. A custom-made LabVIEW program controls the deposition rates of the electron guns by the supplied energy, the movement of carousel, the opening times of shutters, and the deposited sequence. After deposition, the system is flushed with nitrogen until the chamber has atmospheric pressure. After sample exchange and optionally source replacement the chamber is pumped to vacuum for the deposition of the next set of samples.

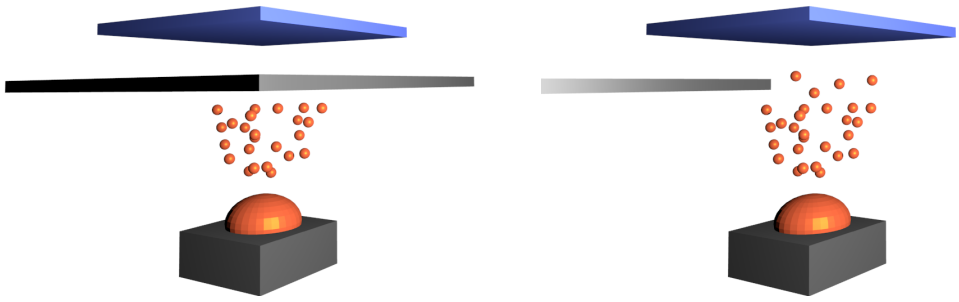

Figure 3.3: Schematic representation of the shutter system.

The nucleation is the rate determining step in the MER method.[24,31,47] The layering of the deposited elements has to mimic the desired product. As the precursors layering and atomic composition is close to the product only low energies are needed to form the desired product. If the precursor has a high deviation in atomic layering and composition then more energy would be necessary to form the compound. On this way it is possible to form metastable compounds if the energy for the nucleation is below the energy which is needed for a rearrangement and the formation of a thermodynamic stable compound.[24] A precise precursor calibration allows the MER

method the formation of compounds that are not accessible by a classic synthesis,[48] *i. e.*, a kinetic control of solid state synthesis.[49]

The deposition order for $[(MX)_{1+\delta}]_m(TX_2)_n$ would be X-M-X-T, with M = Pb, Sn, Bi, or rare earth metal; X = S, Se, Te; T = transition metal. If TX_2 is more oxidation sensitive than MX the order can be reversed. The layers need to contain roughly the right amount of atoms per subunit. For preparation of such sample, slight selenium excess is usually used as typical annealing temperatures are above the evaporation temperature of selenium.[43] The modulated precursors have atomically thin layers with a low degree of crystallinity already in the as deposited material.[47] The order has to be repeated until the desired total thickness is achieved. To change m or n only the number of layer in deposition order has to be changed without further calibration.[44] Different arrangements of m and n give theoretically access to over 20.000 different compounds with m and $n \leq 10$.[28]
Johnson *et al.* prepared $[(M1Se)_{1+\delta}]_m[(T1Se_2)_{1+y}]_n[(M2Se]_{1+\delta}]_m(T2Se_2)_n$ samples with three different constituent layers (M1 $\neq$ M2 or T1 $\neq$ T2) increasing the amount of possible compounds to 130 million.[27,50,51] Doping the T-Se or M-Se layer with another T or M allows the alteration of electrical properties.[52–55] Therefore the MER method allows the preparation of theoretical designed highly complex structures that have enhanced properties.

3.3. Crystal structure of $CuCr_2Se_4$

$CuCr_2Se_4$ crystallizes in a normal cubic spinel structure ($Fd\bar{3}m$) with an a-lattice parameter of 10.337(6) Å.[56] The tetrahedral sites are occupied by copper and 1/8 filled (Figure 3.4, left). Chromium occupies the octahedral sites (1/2 filled, Figure 3.4, right).
Previous work showed that $CuCr_2Se_4$ has a preferred orientation in thin films (Figure 3.5, left), with the [111] direction perpendicular to the substrate.[46,57–59] The cleavage surface of $CuCr_2Se_4$ is also the (111)[60] plane, indicating a low surface energy for (111). Twins tend to nucleate off the (111) plane[61] of $CuCr_2Se_4$. The growth parallel to a twin plane is energetically favourable.[62]
For analysis of ($hk0$) data, we transformed the cubic structure into the hexagonal subgroup $R\bar{3}m$ (Figure 3.5, right). Due to the transformation, the c-lattice changes to $\sqrt{3}c = 17.84$ Å. The atomic positions and lattice parameters for the cubic space group and hexagonal transformation are given in Table 3.1.
Diffusions of niobium through the selenium layer is slow, preventing the formation of

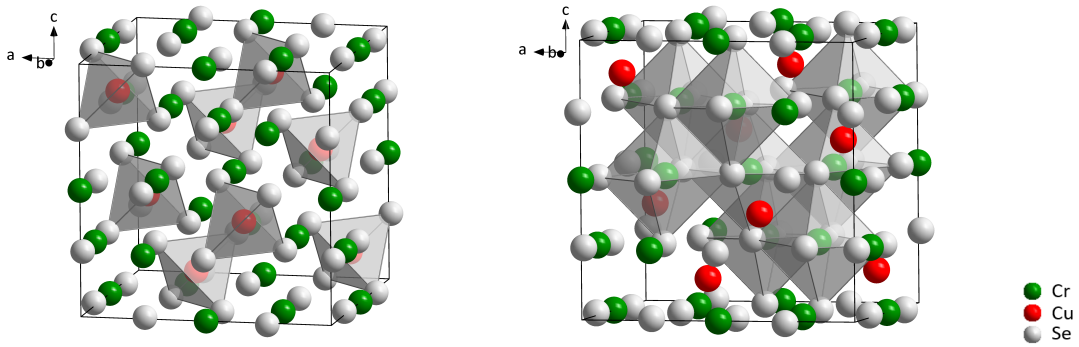

Figure 3.4: Spinel structure of $CuCr_2Se_4$ Cu sits within the tetrahedral sites (left) and Cr within the octahedral sites (right). For clearness not all octahedral sites are drawn.[56]

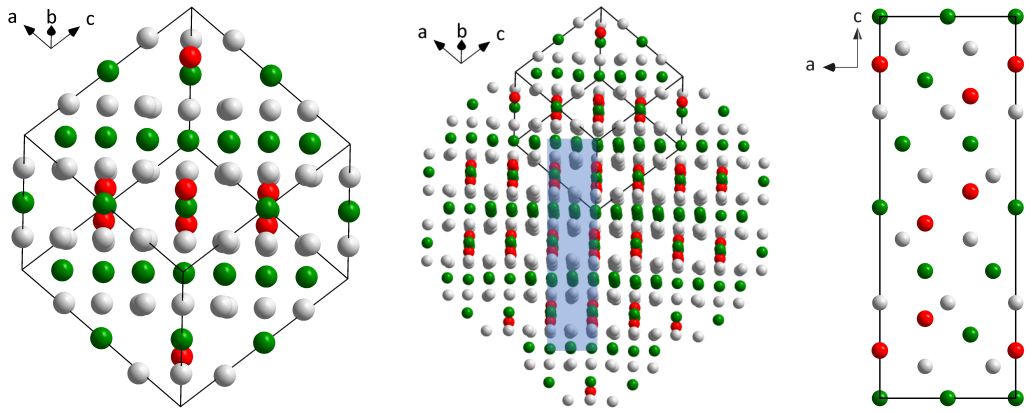

Figure 3.5: Spinel structure of $CuCr_2Se_4$ along the [111] (left) with filled coordination sphere and marked (blue) are for hexagonal transformation (middle). Hexagonal projection of $CuCr_2Se_4$ view along b-axis (right).

higher order product.[63] Gupta *et al.* found that, at low reaction temperatures below 300 °C, the formation of $CuCrSe_2$ is favoured as opposed to $CuCr_2Se_4$.[64]
As copper diffusion is a known issue,[65,66] especially in thin films,[67–69] controlling the copper content in the $CuCr_2Se_4$ layer is challenging and the copper content in the crystalline $CuCr_2Se_4$ layer might be lower than in the precursor. The phase diagram of $CuCr_2Se_4$ and $CuCrSe_2$ (Figure 3.6) shows that with increasing copper content the formation of $CuCrSe_2$ is more likely.

Table 3.1: Cell, atomic parameters and Wyckoff positions for the cubic spinel and the hexagonal transformation.

	$Fd\bar{3}m$	Wyckoff	$R\bar{3}m$	Wyckoff
c [Å]	10.377(6)		17.84	
a [Å]	$= c$		7.31	
Cu1	1/8 1/8 1/8	8a	0 0 1/8	6c
Cr1	1/2 1/2 1/2	16d	0 0 1/2	3b
Se1	1/4 1/4 1/4	32e	0 0 1/4	6c
Cr2	-		1/2 0 0	9e
Se2	-		1/2 1/2 1/2	18h

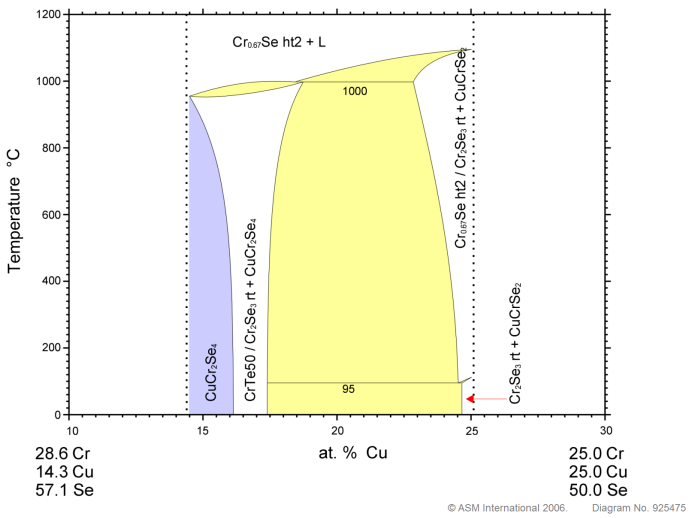

Figure 3.6: Binary section of the ternary phase diagram for Cu-Cr-Se. ASM Alloy Database.[70]

3.4. Structure of transition metal dichalcogenides

Transition metal dichalcogenides (TMDs) TX_2 of group IV, V, VI and VII transition metals have a layered structure.[71] The individual layers are stacked along the c-axis and bond by weak van der Waals interactions. These weak van der Waals bonds allow the exafolation of TMDs down to single layers.[72] In-plane, the TMDs are connected by strong covalent bonds.[73] The layers are hexagonally packed and have a thickness of 6 - 7 Å. The two dichalcogenides layers of the TMD can stack aligned AbA, giving a trigonal prismatic coordination (D_{3h}) of the metal atom. The trigonal prismatic coordination is referred to as 2H (1H in a single layer). The layering of the two polytypes along the c and b-axis is shown in Figure 3.7. Alternatively, one of the layers can be shifted giving an AbC layering. Due to the shifted layer, the metal is octahedrally coordinated (D_{3d}), referred to as 1T polytype.[73–76] The two

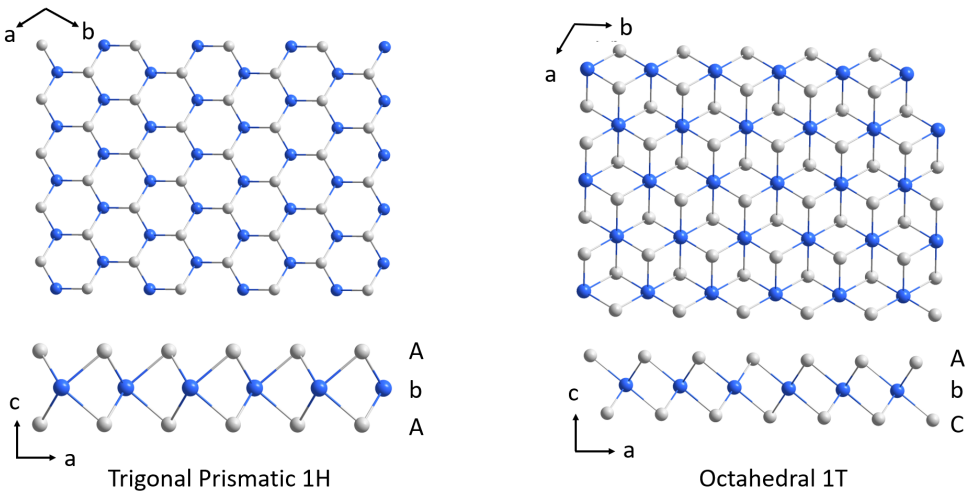

Figure 3.7: TX_2 single layer with viewing direction along c (top) and b-axis (bottom) for trigonal prismatic (left) and octahedral coordination (right).

coordination and the corresponding layering can be seen in Figure 3.8. The 1T and 2H polytypes can be stacked in various sequences. Eleven different polytypes can be found in TMDs which can be transformed into each other by external parameters.[77]

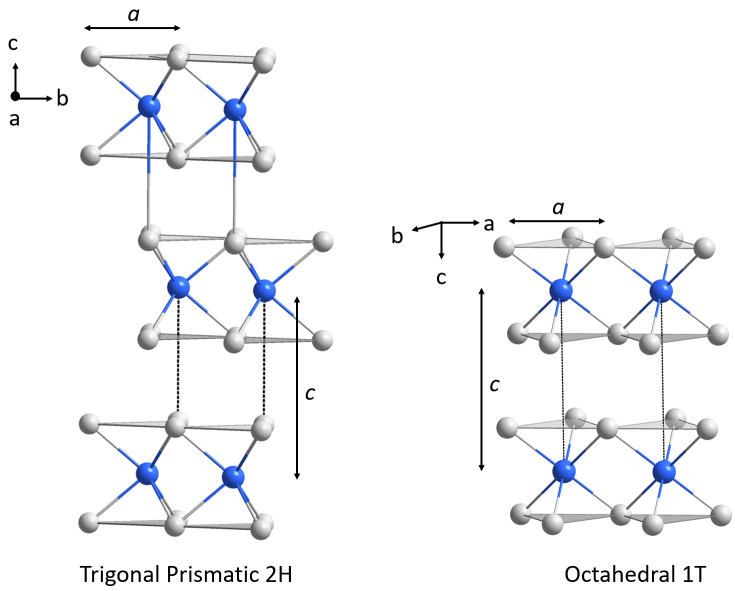

Figure 3.8: Stacking of the individual TMD layers along c-axis for the 2H (left) and 1T polytype (right).

Group IV elements form the 1T polytype and group V elements mostly form the 1T polytype. Group VI elements mostly crystallize in the 2H polytype, and group VII elements form a distorted 1T polytype.[73] The properties and symmetry of the TMDs depend on the filling of the d orbitals.[75] d^0 systems are more stable in octahedral coordination than in trigonal prismatic.[73] Filling the d orbital the trigonal prismatic

is energetically more stable than the octahedral structure, which is again reversed for system with even higher d-electron counts (group VII elements).[73] By intercalation into the van der Waals gap, the filling of the d orbital can be engineered and a transformation of the coordination can be induced.[74]
If the bulk TX_2 forms only one polytype, the corresponding ferecrystalline material will also consist of only this polytype, otherwise the individual TMD layers will be turbostratically disordered.[78] Johnson *et al.* discovered that the dichalcogenides tend to crystallize in ferecrystals in their thermodynamically stable polymorph.[31] By increasing n in $[(MSe)_{1+\delta}]_m(TSe_2)_n$, a huge variation of higher order polytypes is accessible in ferecrystals and even polytypes that have not been reported in the bulk material can be formed.[79]

3.5. X-ray and neutron reflectometry

X-ray reflectometry (XRR) and neutron reflectometry are surface sensitive scattering techniques that can be used to analyze the layer and film thickness, material density, roughness of surface and interface, and determine the layer structure.[80]

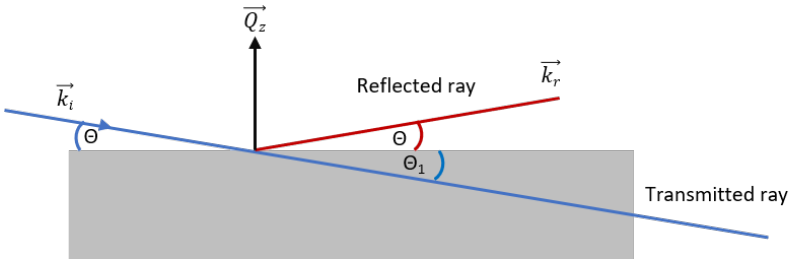

Figure 3.9: Schematic representation of the reflection at an interface showing incident ray $\vec{k_i}$ and reflected ray $\vec{k_r}$ at angle θ and the scattering vector $\vec{Q_z}$.

If the incident angle of an incoming beam is below the critical angle θ_c, total reflection occurs. For incident angles larger than θ_c ($\theta > \theta_c$) a part of the beam penetrates the sample and is transmitted and another part is reflected on the surface (Figure 3.9). The difference between the reflected ray $\vec{k_r}$ and the incident ray $\vec{k_i}$ gives the scattering vector $\vec{Q_z}$ (equation 3.1).[81]

$$\vec{Q_z} = \vec{k_r} - \vec{k_i} \tag{3.1}$$

As the moduli of $\vec{k_r}$ and $\vec{k_i}$ are equal in elastic scattering,

$$\left|\vec{k_r}\right| = \left|\vec{k_i}\right| = k_0 = \frac{2\pi}{\lambda} \tag{3.2}$$

the scattering vector can be written as:

$$Q := |Q_z| = \sqrt{{k_0}^2 + {k_0}^2 - 2k_0 cos(2\theta_i)} = \frac{4\pi sin(\theta_i)}{\lambda} \tag{3.3}$$

X-ray and neutron reflectometry are related to the refractive index n:

$$n = 1 - \delta + i\beta \tag{3.4}$$

Where δ is the anomalous dispersion correction

$$\delta = \frac{r_e \rho_e \lambda^2}{2\pi} \tag{3.5}$$

and β related to the absorption length μ

$$\beta = \frac{\lambda \mu_x}{4\pi} \tag{3.6}$$

r_e is the electron radius ($2.818 \cdot 10^{-15}$ m) and ρ_e is the electron density.[82]
For neutron reflectometry δ and β are generally in the same order of magnitude as for X-rays. As the scattering length b is different for neutrons δ and β for neutron reflectometry are as follows:[81]

$$\delta = \frac{b \rho_n \lambda^2}{2\pi} \tag{3.7}$$

$$\beta = \frac{\lambda \mu_n}{4\pi} \tag{3.8}$$

The scattering length density (SLD) of a material depends on its density, the intrinsic scattering power and has the units Å^{-2}. The intrinsic scattering power depends on the electrons density and nuclear scattering lengths for X-ray and neutron scattering, respectively.[82] The neutron SLD is:

$$\text{SLD} = \frac{\sum_{i=1}^{N} b_i}{V_m} \tag{3.9}$$

Where b_i is the scattering length of the N atoms within the material and V_m is the material volume. The SLD can be calculated for X-rays as:

$$\text{SLD} = r_e N_A \frac{\sum_{i=1}^{N} \rho_m Z_i}{M} \tag{3.10}$$

Here, N_A is the Avogadro constant, and ρ_m is the mass density of the material and M is the molecular weight. Z is the Thomson scattering factor describing the elastic scattering of a wave on z electrons of an isolated atom.
Multiple layers with varying SLDs give a scattering length density profile normal to the interface which determines the reflectivity.

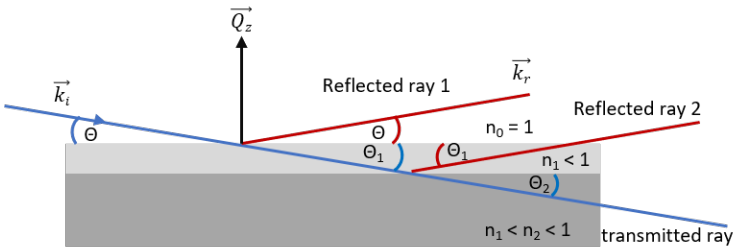

Figure 3.10: Schematic representation of reflection at a layer on a substrate showing incident ray $\vec{k_i}$ and reflected ray $\vec{k_r}$ at angle θ and the scattering vector $\vec{Q_z}$.

In a layered material like in Figure 3.10 the beam can be reflected at the layer/air interface or at the layer/substrate interface and both can interfere. The resulting periodic oscillations are called Kiessig Fringes. The period of the Kiessig Fringes is determined by the film thickness d.[83] From the separation of the Kiessig Fring maxima ΔQ the total film thickness can be calculated as:

$$\Delta Q = \frac{2\pi}{d} \tag{3.11}$$

The total layer thickness in a ferecrystal d was calculated from the Kiessig Fringes in the XRR data.[84] The modified Braggs law (Eq. 3.12) gives the angular position θ_i of the Kiessig Fringes.[85] Where m_i is the diffraction order of the i-th maxima, λ the X-ray wavelength and θ_c angular position of critical angle.

$$m_i\lambda = 2d\sqrt{sin^2\theta_i - sin^2\theta_c} \tag{3.12}$$

Absolute film thickness is determined by rearranging the equation-plotting the square of the sine of the maxima of the oscillations θ_i versus the square of the wavelength over two times the order m_i squared and extracting the thickness d from the slope, as given by the equation below.
The equation was rearranged to equation 3.13 and the $\sin^2\theta_i$ as plotted a function of λ^2 over two times the order m^2. Then the film thickness can be extracted from the slope of the plot.

$$sin^2\theta_i = \left(\frac{\lambda}{2}\right)^2 \frac{m^2}{d^2} + sin^2\theta_c \tag{3.13}$$

The path of the beam in Figure 3.10 can be described by Snell's law (equation 3.14).

$$n_0 sin(\theta) = n_1 sin(\theta_2) \tag{3.14}$$

Air has a refractive index of 1 (n_0) and for the critical angle where $\theta_2 = 0$ (3.13) can be derived as:

$$\theta_c = arccos(n_1) \tag{3.15}$$

In order to model the reflectivity data out of the SLD profile, Paratt's formalism is used in this work. Parrat's formalism (equation 3.16) gives a precise expression for all regions since absorption is considered and no approximations are made.[86] The reflectivity r for N+1 layers is described as:

$$r_{N+1} = \frac{r'_{N,N+1} + r_N e^{id_N k_N}}{1 + r'_{N,N+1} r_N e^{id_N k_N}} \tag{3.16}$$

Here d_N is the material thickness. The Fresnel reflection coefficient[87] between the layers N and *N+1* $\theta > \theta_c$ is:

$$r'_{N,N+1} = \frac{k_{N+1} - k_N}{k_N + k_{N+1}} \tag{3.17}$$

As the layer and surface roughness σ generate a diffuse scattering, Névot and Croce deduced a modified Fresnel coefficient which considers the roughness:[80,88]

$$r'_{N,N+1} = \frac{k_{N+1} - k_N}{k_N + k_{N+1}} e^{-2k_N k_{N+1} \sigma^2_{N,N+1}} \tag{3.18}$$

$$k_N = \sqrt{\omega^2 - 2\delta_N i 2\beta_N} \tag{3.19}$$

Here ω is the diffracted-beam direction with respect to the crystal surface.[89]

The effect of the film thickness, density, roughness on the SLD profile, and the reflectivity curve are represented in Figures 3.11 - 3.13. A multilayer of Mo|Nb|Mo on silicon was simulated. The molybdenum density and thickness thereby were kept constant. By increasing the niobium film thickness, the distance between the Kiessig Fringes is reduced (Figure 3.11). The lower intensity in the SLD profile corresponds to niobium (64.259 Å^{-2}). When the niobium layer thickness is increased the distance between the molybdenum parts in the SLD profile increases as well.
The difference in density of the layers and the substrate affects the amplitude of Kiessig Fringes. A large density difference gives a higher amplitude for the Kiessig

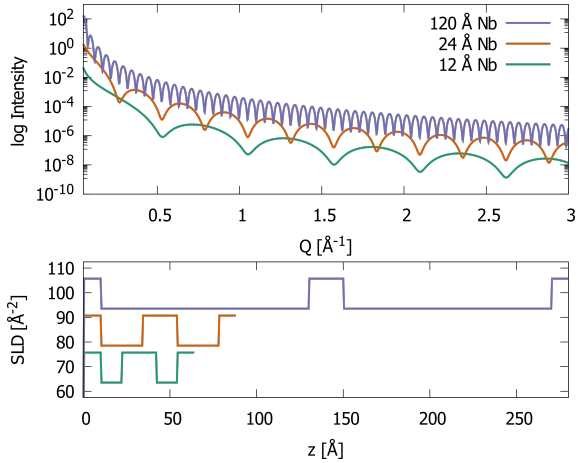

Figure 3.11: Effect of niobium layer thickness in Mo|Nb|Mo films on a silicon substrate on the Kiessig Fringes (top) for visualization is the data plotted with an offset. SLD profiles of the films for visualization are the SLD plotted with an offset (bottom).

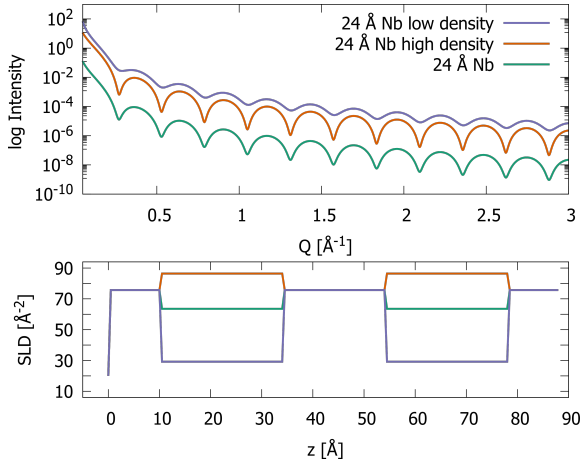

Figure 3.12: Effect of niobium layer density in Mo|Nb|Mo films on a silicon substrate on the Kiessig Fringes (top) and on the SLD profile (bottom).

Fringes. The niobium part in the SLD profile is effected by the change in density (Figure 3.12).

In most cases a surface or interface is not perfectly smooth but shows a certain roughness. The decrease in intensity of the Kiessig Fringes is related to the roughness of the surface and the different interfaces.[87] The roughness was changed for niobium, molybdenum and the substrate by the same degree. Figure 3.13 demonstrates the effect of different surface roughnesses on the reflectivity curve and SLD profile.

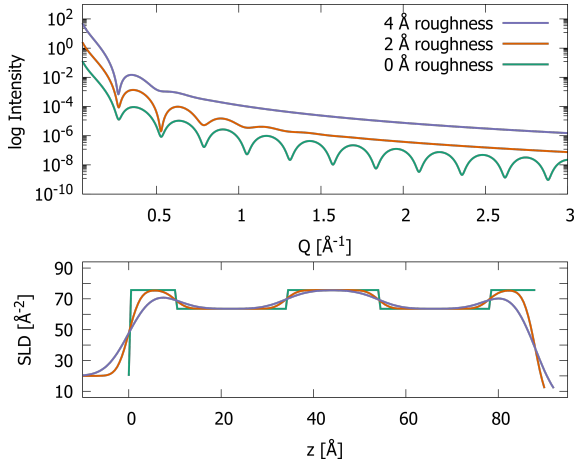

Figure 3.13: Effect of niobium layer roughness in Mo|Nb|Mo films on a silicon substrate on the Kiessig Fringes (top) and on the SLD profile (bottom).

3.5.1. Polarized neutron reflectometry

Polarized neutron reflectometry (PNR) allows the determination of the vector magnetization of the material. The magnetic moment of the neutron can be used to analyze the vector magnetization depth profile normal to the surface.[90,91] Therefore it is possible to analyze strength and range of magnetic interactions in a multilayered material.

The neutrons of the incident beam are conventionally polarized to a fixed direction. The investigated material may then change the polarization of the neutrons.[92] The reflectivity pattern of the material is analyzed according to the sign of the neutron polarization before and after the reflection R^{++}, R^{--}, R^{+-} and R^{-+}.[90]

4. Interlayer correlations in 1:1 ferecrystals

4.1. Introduction and aims

Understanding and controlling nucleation and growth is an important step in improving the crystallinity of thin films and thus crucial for the materials performance.[18,93] Ferecrystals $[(MSe)_{1+\delta}]_m(TSe_2)_n$with $m = n = 1$ (here refereed to as 1:1) are typical parent systems for higher order ferecrystals as they are generally more easily accessed.[94–97] Ferecrystals with $m = n > 1$ become more unstable with increasing m, n and decompose into the 1:1 compound with increasing annealing temperature.[98] Moreover, a comparison with the corresponding misfit material is not possible for the very large range of potential higher order (m, n) ferecrystals[28,99] as most misfit compounds have the composition $[(MSe)_{1+\delta}]_1(TSe_2)_1$.[34,100]
Previous X-ray or electron diffraction experiments on 1:1 samples had a rather low resolution and showed only broad (hkl) reflections.[31,32,94,97]
Recent high resolution studies on $[(SnSe)_{1+\delta}]_1(VSe_2)_1$ ferecrystals indicate directionally dependent interlayer registration, as opposed to the typically observed rotational disorder.[31,101] STEM images of $[(SnSe)_{1+\delta}]_1(TSe_2)_1$ revealed regions with long range order in the stacking direction c.[102] Those results show that at least for some 1:1 ferecrystals ordered domains are present.
A systematic study of such potential interlayer structural correlations in five different 1:1 ferecrystals was carried out and is presented in this chapter.

4.2. Evidence of interlayer correlation

In order to identify interlayer correlations in 1:1 ferecrystals, reciprocal space maps were performed along the l direction (Q_z) of the first in-plane reflections, where the rock salt and dichalcogenide reflections overlap. X-ray diffraction scans in in-plane ($hk0$) and out-of-plane ($00l$) geometry were performed to determine the lattice parameters and exclude a deviation from the usual ferecrystalline structure in these directions.
Figure 4.1 gives the out-of-plane diffraction patterns of the 1:1 materials. The different 1:1 ferecrystals are abbreviated to MT as all investigated ferecrystals are based on selenium and only the M and T metals are varied. For instance $[(SnSe)_{1+\delta}]_1(VSe_2)_1$ is abbreviated to SnV.

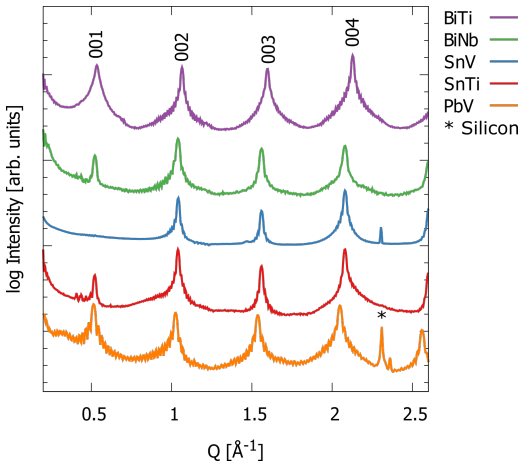

Figure 4.1: X-ray diffraction patterns of selected $m = n = 1$ ferecrystals in out-of-plane $(00l)$ geometry.

All observed reflections in the X-ray diffraction patterns of out-of-plane geometry are indexed according to $(00l)$ reflections of the ferecrystal superstructure, indicating that the individual layers of samples are stacked along the c-axis. The refined c-lattice parameters are given in Table 4.1. c-lattice parameters, determined by a Le Bail fit, and atomic distances, determined by Rietveld refinement, are consistent with previously published data of these materials.[31,43,94,95,102–104] Detailed results of the Le Bail fit and Rietveld refinement can be found in appendix chapter A.1.

Table 4.1: c-lattice parameters obtained from Rietveld refinement of X-ray diffraction patterns in out-of-plane geometry.

	c [Å]
SnTi	12.083(2)
PbV	12.282(6)
BiNb	12.091(3)
SnV	12.070(2)
BiTi	11.818(6)

Figure 4.2 shows X-ray diffraction patterns in in-plane geometry for the five 1:1 ferecrystals. All observed reflections are indexed according to $(hk0)$ reflections of the binary compounds as expected for ferecrystalline materials.[43,99] The in-plane lattice parameters of the binary compounds, obtained by the Le Bail method, are given in Table 4.2. Detailed results of the Le Bail fit are given in the appendix chapter A.1. The obtained lattice parameters are consistent with previously published data of these materials.[31,43,94,95,102–104] Some of the in-plane lattice parameters have a slight variation to the bulk values which is a known phenomenon for ferecrystals.[99]

In the X-ray diffraction patterns in in-plane (Figure 4.2) and out-of-plane (Figure 4.1) geometry all reflections could be indexed as (00l) reflections of the superstructure or (hk0) reflections of the binary compounds. Therefore they give no evidence for a (hkl) superstructure.

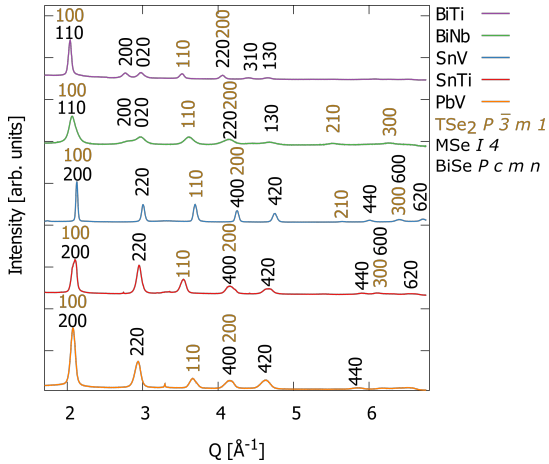

Figure 4.2: X-ray diffraction patterns of selected $m = n = 1$ ferecrystals in in-plane (hk0) geometry.

Table 4.2: Lattice parameters obtained from Le Bail fits of X-ray diffraction patterns in in-plane geometry.

	a MSe [Å]	b MSe [Å]	a TSe_2 [Å]
PbV	6.079(3)	$= a$	3.435(3)
BiNb	4.45(1)	4.25(1)	3.497(6)
SnTi	5.969(6)	6.078(3)	3.555
SnV	5.919(1)	$= a$	3.4025(6)
BiTi	5.565(3)	4.247(3)	3.590(2)

Figure 4.3 shows the reciprocal space maps of the 1:1 ferecrystals. The corresponding in-plane scans are on top of the space maps and the (hk0) reflections are indexed. Along the Q_z direction, unexpected reflections are identified, that are not consistent with the binary compound.

The reciprocal lattice mismatch along Q_z of the $[20l]_{MSe}$ and $[10l]_{TSe_2}$ reflections is given as ΔQ. For those ferecrystals revealing nearly coinciding in-plane reflections (BiTi and SnV) with $\Delta Q \approx 0$, the (hkl) reflections in the reciprocal space maps are very sharp and in line along Q_{par} (Figure 4.3). BiNb, PbV and SnTi have a higher deviation of the in-plane reflection positions and more diffuse and smeared (hkl) reflections with a distinct offset in Q_{par} of the (hkl) reflections.

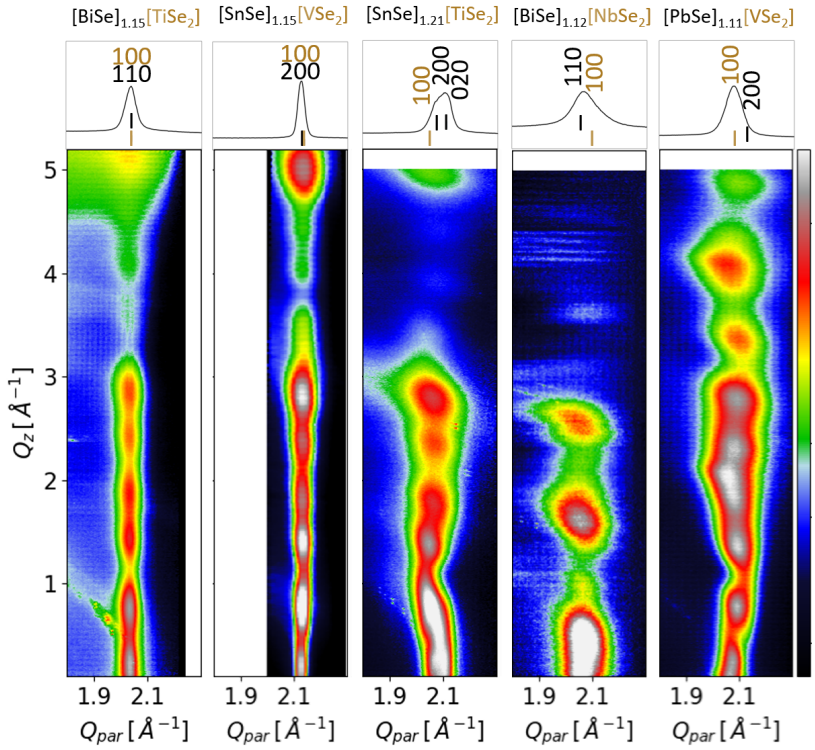

Figure 4.3: Reciprocal space maps of the investigated ferecrystals along with in-plane diffraction intensity (top).

To analyze the $[20l]_{\mathrm{MSe}}$ and $[10l]_{\mathrm{TSe_2}}$ reflections series, intensity profiles along Q_z were integrated. The out-of-plane modulation distance $\Delta\mu$ is the mean distance between two reflection maxima in the intensity profiles along Q_z. $\Delta\mu$ was determined by Gaussian fits of all reflections along the Q_z direction as shown exemplarily for SnV in Figure 4.4 (remaining fits can be found in the appendix chapter A.2). The individual reflections were fitted with individual reflection positions (position of the Gaussian maxima) and intensities. All reflections could be fitted with same width, indicating that the reflections are either generated by the same compound or by compounds with the same correlation length. $\Delta\mu$ relates to the lattice parameter of the compound generating the (hkl) reflections along Q_z (referred to as z-lattice parameter) according to:

$$\frac{2\pi}{\Delta\mu} = z\text{-lattice parameter} \tag{4.1}$$

The z-lattice parameters calculated from the modulation distance and the c-lattice parameter determined from Le Bail fit of the out-of-plane diffraction patterns are plotted in Figure 4.4. For all samples, the z-lattice parameter derived from the modulation distance is in good agreement with the superstructure lattice parameter c determined in the $(00l)$ direction of the ferecrystals, indicating that the repetition

unit is one or a multiple of $[(\mathrm{MSe})_{1+\delta}]_1(\mathrm{TSe}_2)_1$ structural units.

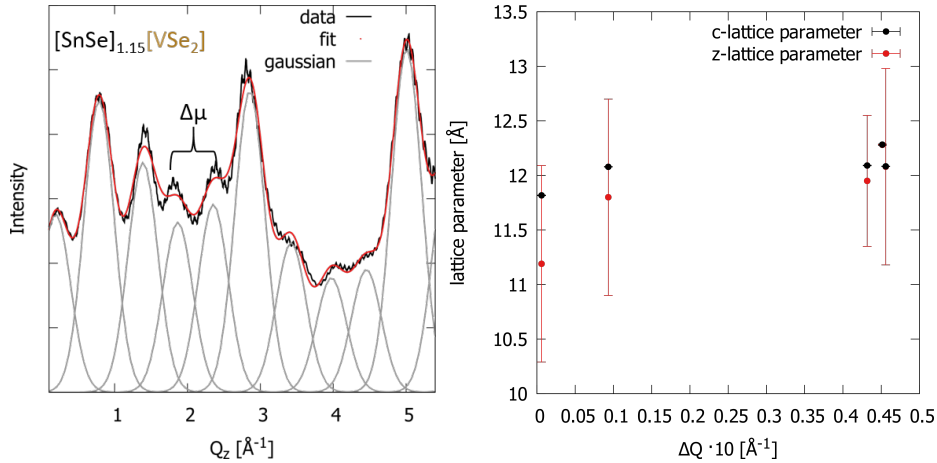

Figure 4.4: Intensity profile along Q_z with Gaussian fits shown exemplary for the SnV ferecrystal (left) and z-lattice parameter compared with the superstructure c-lattice parameter, as a function of ΔQ (right).

As the $(00l)$ reflections of the ferecrystal superstructure are highly diffuse in Q_{par} direction (Figure 4.5 left) the reflections along the $[20l]_{\mathrm{MSe}}$ and $[10l]_{\mathrm{TSe}_2}$ series might arise from an overlap of the binary (hkl) reflections and the $(00l)$ reflections of the superstructure. The intensity profile along Q_z of the 1:1 ferecrystals together with the out-of-plane diffraction pattern of SnV are shown in Figure 4.5 (right). The intensity profiles along Q_z of the 1:1 ferecrystals do not match the reflection position of the out-of-plane diffraction pattern. This provides strong evidence that the unexpected reflections along the $[20l]_{\mathrm{MSe}}$ and $[10l]_{\mathrm{TSe}_2}$ series do not arise from an overlap of $(00l)$ reflections, but indicate an interlayer correlation for 1:1 ferecrystals.

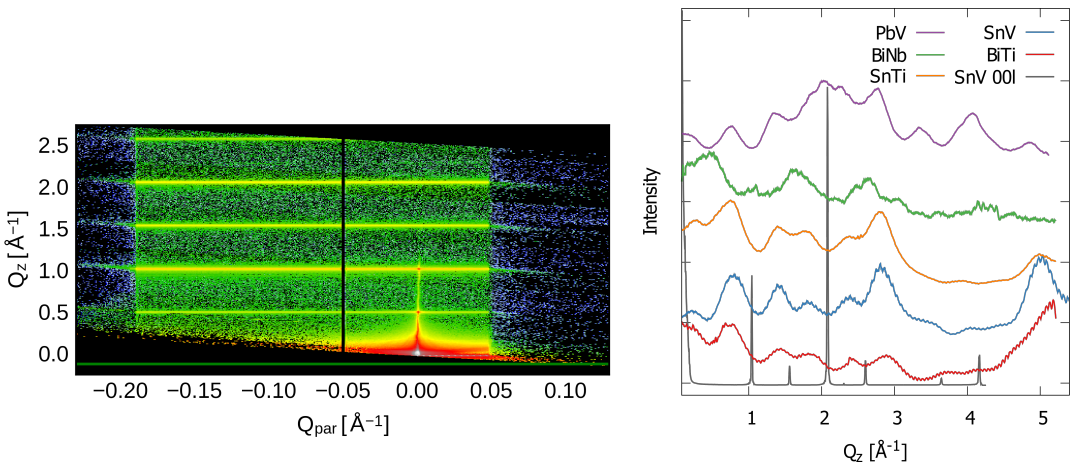

Figure 4.5: Reciprocal space maps along the $(00l)$ reflections (left) and intensity profile along Q_z of selected $m = n = 1$ ferecrystals (right).

The reflection full width at half maximum (FWHM) can be used to calculate the coherence length D in the corresponding direction. By using the FWHM, D can

Table 4.3: Coherence lengths determined for the ferecrystal superstructure (00l) and the interlayer correlation (hkl).

	00l FWHM [Å^{-1}]	00l D [Å]	hkl FWHM [Å^{-1}]	hkl D [Å]
SnTi	0.016	392.70	0.506	12.42
PbV	0.018	349.07	0.426	14.75
BiNb	0.020	314.16	0.586	10.72
SnV	0.015	418.88	0.484	12.98
BiTi	0.020	314.16	0.574	10.95

be approximated by D $\approx \frac{2\pi}{FWHM}$. In ferecrystals, the structural coherence length of the (00l) reflections is in most cases near the total sample thickness. The (hk0) reflections give the average grain size in-plane, which is usually in the range of 0.9 - 12 nm.[105,106] For individual (hkl) reflections, the width along Q_z should correspond to the individual layer thickness of the binary compounds.
The coherence length D approximated by D $\approx \frac{2\pi}{FWHM}$ for the (00l) superstructure is in the order of magnitude of the total sample thickness of 25 - 35 [MSe][TSe_2] double layers (Table 4.3). In contrast, the coherence length D obtained for the (hkl) superstructure is much smaller, underlining that the (hkl) reflections along the $[20l]_{MSe}$ and $[10l]_{TSe_2}$ are independent from the (00l) reflections. This supports that there is an interlayer correlation between the binary compounds in 1:1 ferecrystals.

4.3. Higher order reflections

For the 1:1 SnV ferecrystal, higher order reflection series of $[20l]_{VSe_2}$ $[40l]_{SnSe}$ and $[30l]_{VSe_2}$ $[60l]_{SnSe}$ were also investigated to determine if the correlation is limited to the first overlapping reflections. Reciprocal space maps and intensity profiles are presented in Figure 4.6. For these reflection series, no superstructure reflections were observed. Instead, the out-of-plane lattice parameter in the range of $c = 6(1)$ Å corresponds well with the c-lattice parameters of the binary compounds, and all observed reflections can be indexed according to the binary crystal structure.
This indicates that the interlayer correlation between the binary compounds effects only the $[20l]_{MSe}$ and $[10l]_{VSe_2}$ direction and not the higher order reflections. It is also possible that the intensity of the correlation reflections is weaker at higher Q than the intensity of $[20l]_{VSe_2}$ $[40l]_{SnSe}$. $[30l]_{VSe_2}$ $[60l]_{SnSe}$ in in-plane direction (Figure 4.2) is much weaker than the $[20l]_{SnSe}$ and $[10l]_{VSe_2}$ reflections indicating that the reflections of the correlation might have an intensity too low for detection.

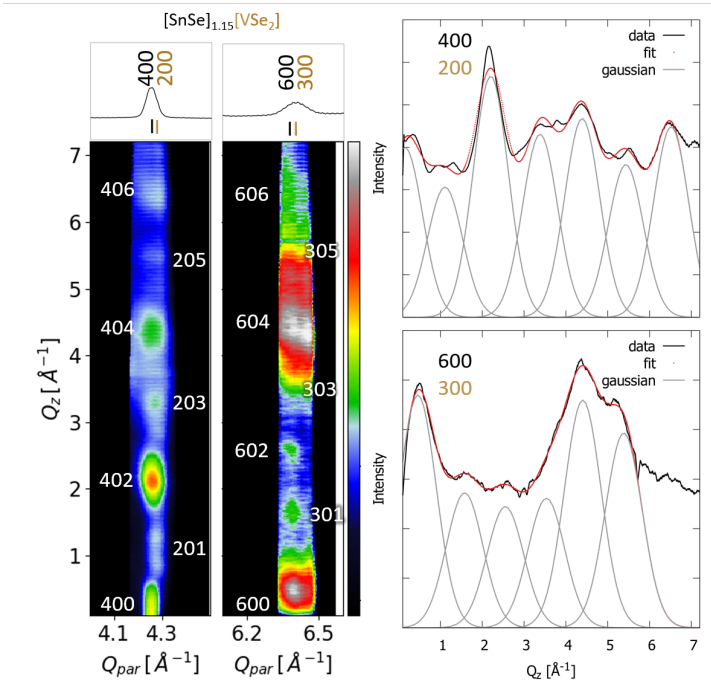

Figure 4.6: Reciprocal space maps in l direction for the higher order reflection series in the SnV ferecrystal (left) and corresponding intensity profiles with Gaussian fits (right).

4.4. Reciprocal space maps along MSe and TSe_2 reflection series

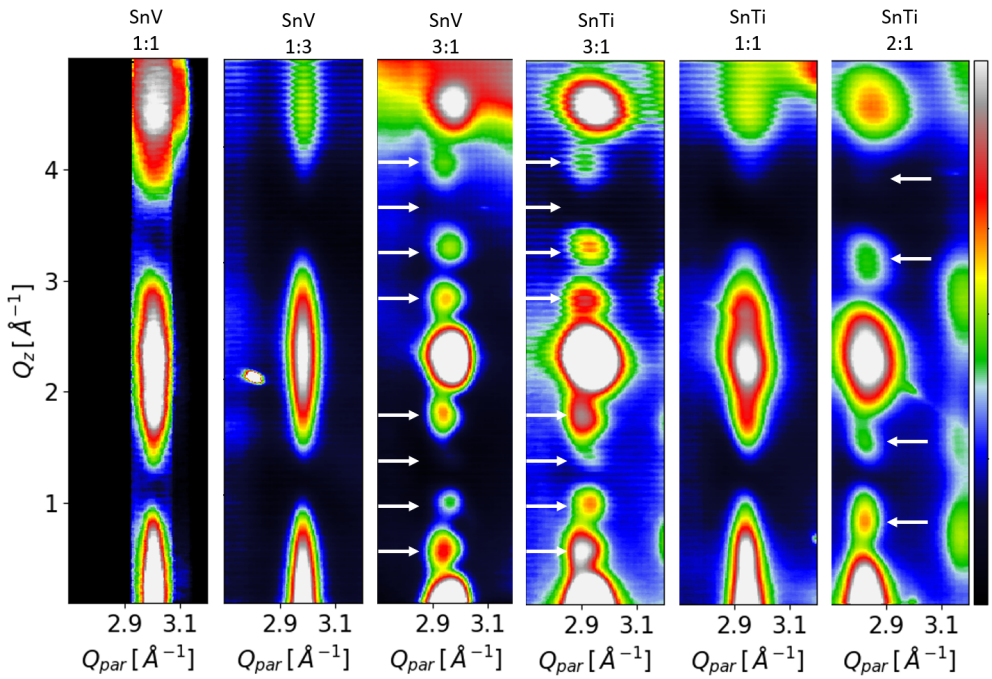

Figure 4.7: Reciprocal space maps for SnV and SnTi ferecrystals with mixed m,n, along $[22l]_{\mathrm{SnSe}}$.

For the SnV and SnTi series with m, $n \neq 1$ and $m = n = 1$, reciprocal space maps along the $[22l]_{\mathrm{SnSe}}$, $[31l]_{\mathrm{SnSe}}$ and $[11l]_{\mathrm{TSe_2}}$ were measured (Figure 4.7 - 4.10). The intensity profiles of SnV and SnTi are given in Figure 4.8. ($2m$-1) Laue oscillations in between Bragg reflections are observed, as expected for the samples with $m \neq 1$ (indicated by white arrows in Figure 4.7).[106,107] The in-plane and out-of-plane diffraction patterns for the ferecrystals with higher m, n order give no evidence for an (hkl) superstructure and are in agreement with previously published data (appendix chapter A.3).[103,108,109]

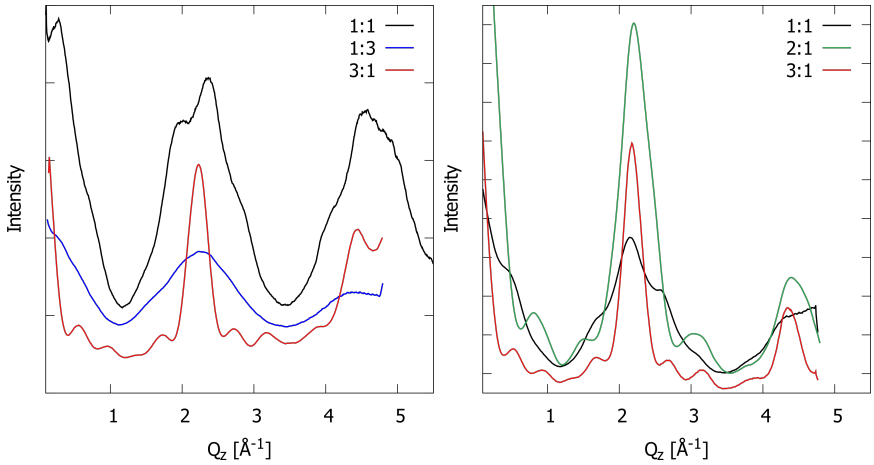

Figure 4.8: Intensity profiles of SnV (left) and SnTi (right) ferecrystals with mixed m,n, along $[22l]_{\mathrm{SnSe}}$.

Along $[22l]_{\mathrm{SnSe}}$, additional reflections are observed for m, $n = 1$ but not for m, $n \neq 1$ (Figure 4.7 and 4.8). This shows that the correlation is not limited to the $[20l]_{\mathrm{MSe}}$ $[10l]_{\mathrm{TSe_2}}$ series but is not present in higher order ferecrystals with m, $n \neq 1$. The additional reflections due to the correlation along $[22l]_{\mathrm{SnSe}}$ are not strong enough to overlap the (hkl) reflections as they have a higher intensity and the reflections of the correlation appear as shoulders of the (hkl) reflections. This indicates that the correlation effect is weaker with increased Q.

Interlayer correlations are not observed for the $[31l]_{\mathrm{SnSe}}$ (Figure 4.9). This might be due to the lower reflection intensity of the $[31l]_{\mathrm{SnSe}}$. The reflection of the correlation might be present as weak shoulders under the more intense (hkl) reflections.

In addition to reciprocal space maps along the rock salt reflections, scans along the $[11l]_{\mathrm{VSe_2}}$ also were performed (Figure 4.10). As for the scans along the rock salt reflections, no correlation reflections can be observed for the ferecrystals with m, $n \neq 1$. For the 1:1 samples, also only (hkl) reflections are present.

Additional reflections of the correlation can only be seen along $[22l]_{\mathrm{SnSe}}$ this indicates that the correlation mostly affects the rock salt layer.

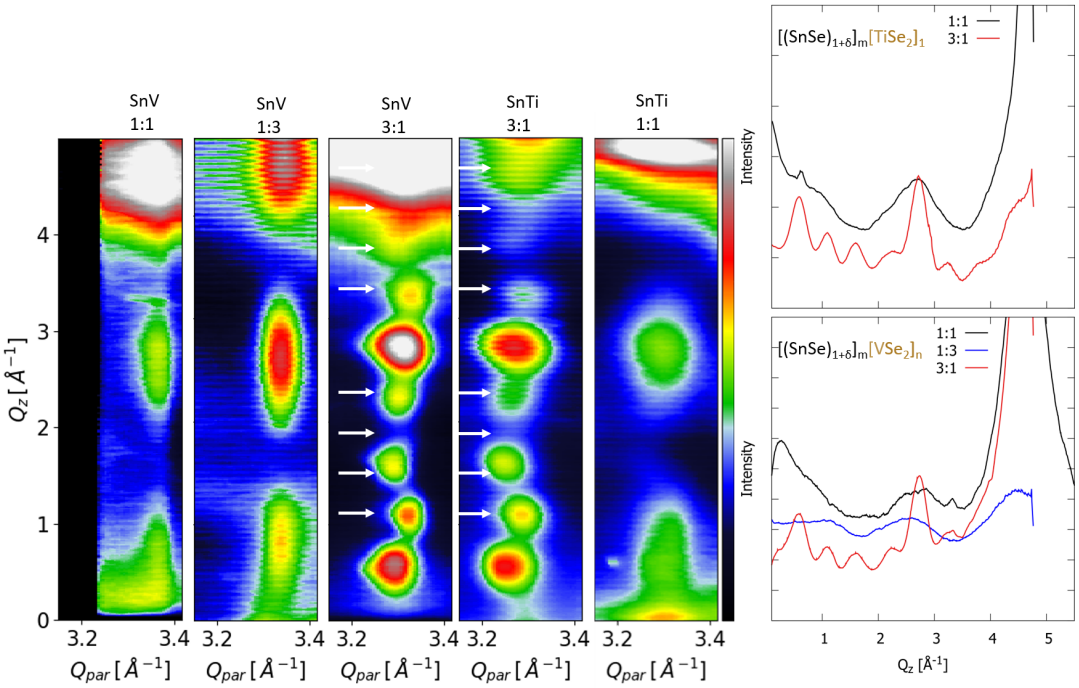

Figure 4.9: Reciprocal space maps for SnV and SnTi ferecrystals with mixed m,n, along $[31l]_{\mathrm{SnSe}}$ (left) and corresponding intensity profiles (right).

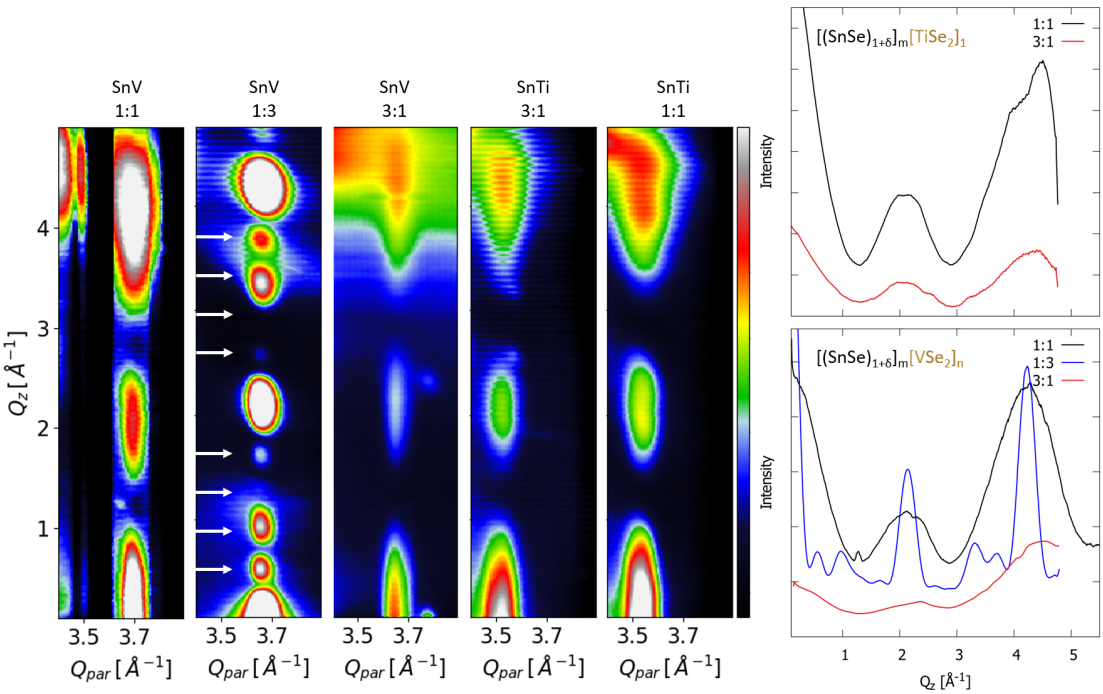

Figure 4.10: Reciprocal space maps for SnV and SnTi ferecrystals with mixed m,n, along $[11l]_{\mathrm{VSe_2}}$ (left) and corresponding intensity profiles (right).

4.5. Potential candidates for interlayer correlations

The previous chapters showed evidence for an interlayer correlation in 1:1 ferecrystals. A detailed discussion of previous work and a connection to the presented results will be given in this chapter.

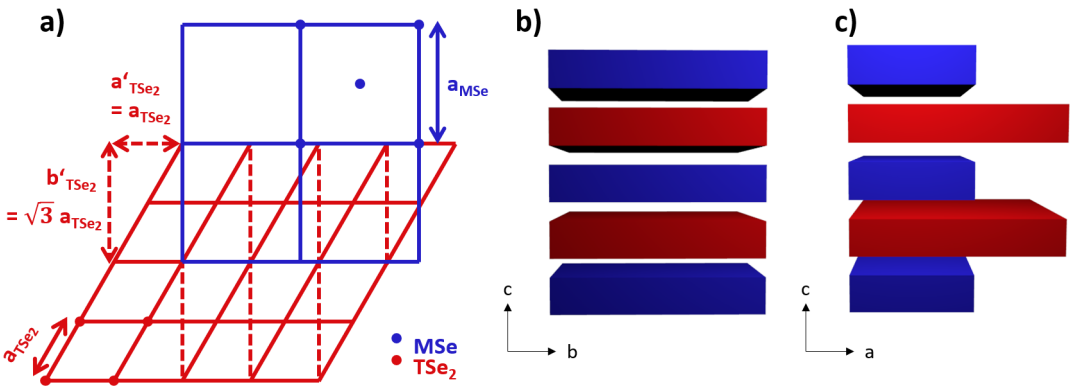

Figure 4.11: a) Relative in-plane orientation for an in-plane lattice of the binary compounds MSe (blue) and TSe_2 (red). Schematic view along b) a- and c) b-axis TSe_2 is represented in the orthorhombic analogue.

Figure 4.11 shows the geometry of the 2D lattices of the binary compounds MSe (blue) and TSe_2 (red). The hexagonal dichalcogenide lattice can be presented in its orthorhombic analogue where $b'_{\mathrm{TSe_2}} = \sqrt{3}a_{\mathrm{TSe_2}}$. Therefore, a commensurate superstructure in $[10l]_{\mathrm{TSe_2}}$ $[20l]_{\mathrm{MSe}}$ direction is only possible if the a_{MSe} and $b'_{\mathrm{TSe_2}}$ lattice parameters coincide. The difference a_{MSe} - $b'_{\mathrm{TSe_2}}$ is the lattice mismatch $\Delta b'$. The unidirectional lattice mismatch of $[10l]_{\mathrm{TSe_2}}$ and $[20l]_{\mathrm{MSe}}$ (ΔQ) decreases with decreasing $\Delta b'$. Figure 4.12 shows ΔQ and Δb' as a function of the misfit parameter δ. The misfit parameter is determined from the relative area of the binary compounds ($\mathrm{MSe_{area}}$ and $\mathrm{TSe_{2area}}$) per formula unit in the binary compounds ($\mathrm{MSe_{unit}}$ and $\mathrm{TSe_{2unit}}$):

$$\frac{\text{MSe unit/MSe area}}{\text{TSe}_2\text{ unit/TSe}_2\text{ area}} = 1 + \delta \tag{4.2}$$

A perfect match of the b_{MSe} and $b'_{\mathrm{TSe_2}}$ lattice parameters would result in a misfit parameter δ of 0.155:

$$b_{\mathrm{MSe}} = b'_{\mathrm{TSe_2}} \tag{4.3}$$

$$\Delta b' = b_{\mathrm{MSe}} - \sqrt{3}a_{\mathrm{TSe_2}} \tag{4.4}$$

$$1 + \delta = \frac{2(b_{\mathrm{MSe}} - \Delta b')}{\sqrt{3}b^2_{\mathrm{MSe}}} \tag{4.5}$$

Therefore, samples with a small lattice mismatch $\Delta b'$ have a misfit parameter δ close to 0.155 (BiTi, SnV). Figure 4.12 gives $\Delta b'$ as function of δ (blue line). The b_{MSe} was set to 6.01 Å which is the in-plane lattice parameter of PbSe in PbV. The in-plane lattice parameters of the rock salt in SnV (5.92 Å) and BiTi (6.23 Å) are also close to 6.01 Å, and therefore these values of $\Delta b'$ (black dots) match to the calculated values (blue line). BiNb and and SnTi have in-plane lattice parameters with $a \neq b$. Therefore can two different values for $\Delta b'$ be calculated and $\Delta b'$ as a function of δ is unable to describe the BiNb and SnV.

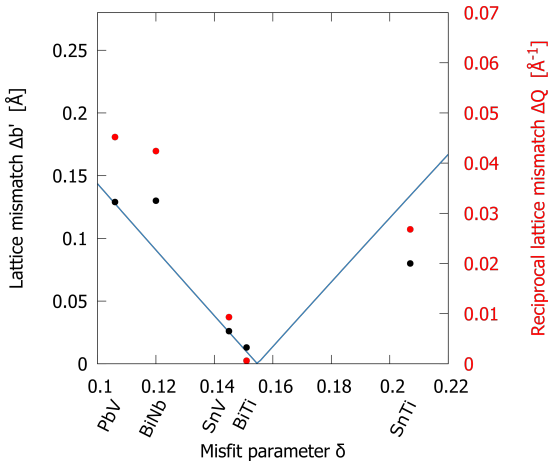

Figure 4.12: Lattice mismatch $\Delta b'$ (left y-axis) and reciprocal lattice mismatch ΔQ and (right y-axis) as a function of the misfit parameter δ. For a clearer visualisation, the absolute value of $\Delta b'$ is given. The equation 4.5 with $b_{\mathrm{MSe}} = 6.01$ Å is plotted in blue.

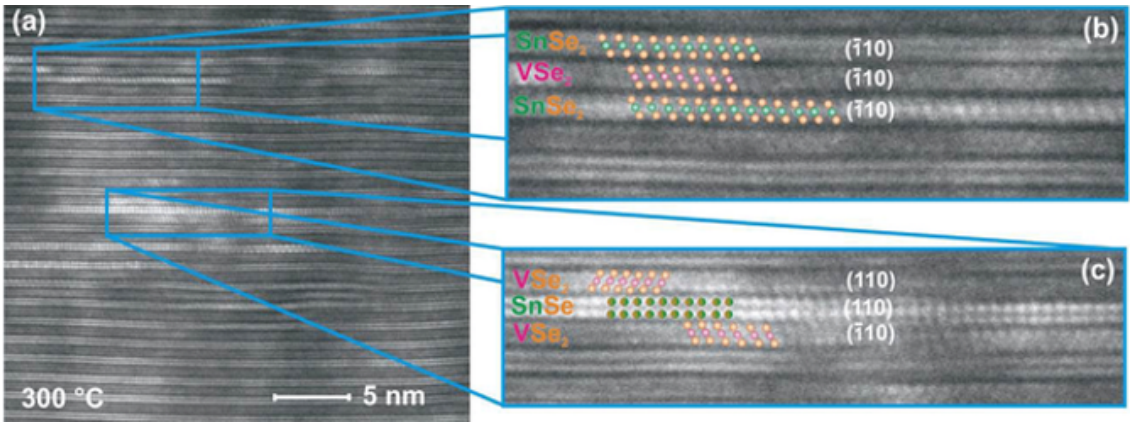

Figure 4.13: (a)HAADF-STEM image of the $(SnSe)_{1.15}VSe_2$ film annealed at 300 °C. The magnified areas clearly reveal the presence of different stacking sequences, (b) $SnSe_2$-VSe_2-$SnSe_2$,and (c)VSe_2-SnSe-VSe_2. (Reprinted figure with permission from M.Falmbigl, M. Esters, D. C. Johnson, *Cryst. Res. Technol. 52*, **2017**.)[47] DOI: 10.1002/crat.201700067 Copyright (2017) by John Wiley and Sons.

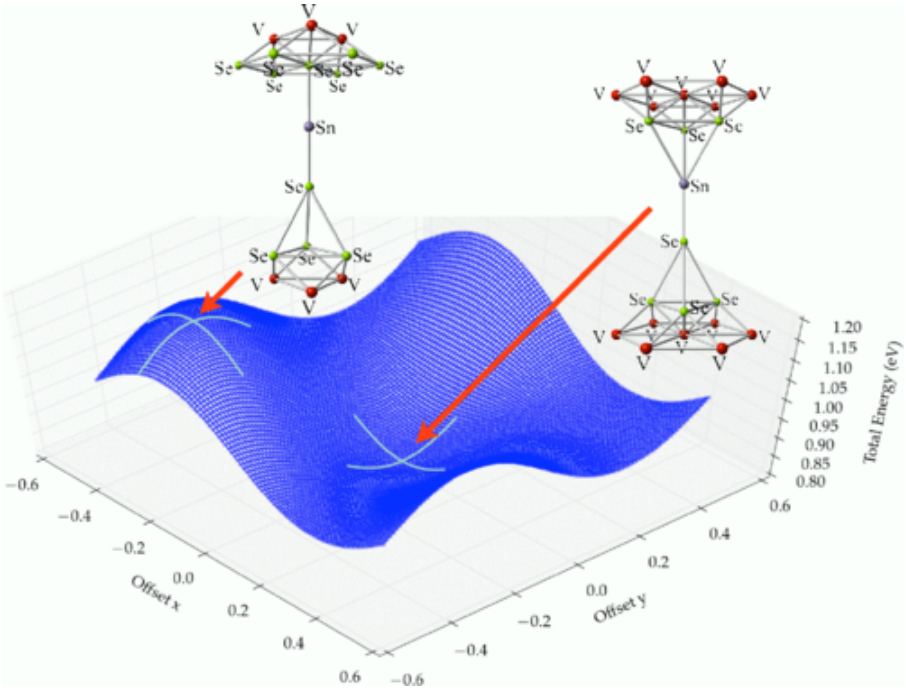

Figure 4.14: Calculated energies for a SnSe "dimer" (islandwith zero radius) sandwiched between 4x4 VSe_2 layers with offsets scanned across a VSe_2 unit cell. Structures are not relaxed. The minimum occurs at d = (0,0), where the dimer sits centered over a Se triangle and in line with a V ion (inset); the maximum is at d = (-1/3,-1/3), where the dimer sits centered in a V triangle with the Sn ion adjacent to a Se ion (inset). The latter geometry but with the dimer's Se ion adjacent to a Se ion (not shown) occurs at d = (+1/3,+1/3), where the energy surface exhibits a third point with zero slope. (Reprinted figure with permission from S. P.Rudind, D. C. Johnson, *Phys. Rev. B 91*, **2015**.)[110] DOI: 10.1103/PhysRevB.91.144203 Copyright (2015) by the American Physical Society.

Johnson *et al.* showed for $(SnSe)_{1.15}VSe_2$ that by annealing the sample, besides VSe_2 and SnSe, $SnSe_2$ is formed.[47] The $SnSe_2$ forms with VSe_2 correlated areas in the 1T polytype (Figure 4.13). By annealing to higher temperatures the $SnSe_2$ transforms into SnSe. Pure transition metal dichalcogenides (TMDs) prepared by the modulated elemental reactants (MER) method show a high disorder if they are able to form not only the 1T polytype but also the 2H or 3R.[31] Johnson *et al.* proposed that the disorder in the ferecrystals is controlled by a template growth.[31] An overview on the possible polytypes in TMDs is given in chapter 3.4.

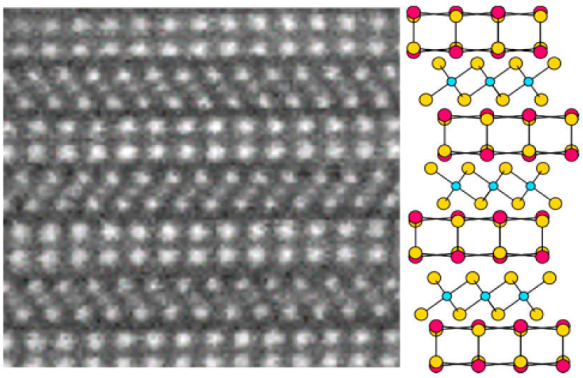

Figure 4.15: Representative HAADF-STEM image of a $(SnSe)_{1.2}TiSe_2$ heterostructure. (Reprinted figure with permission from D. Hamann, D. Merril, S. Bauers, G. Mitchson, J. Ditto, S. P. Rudin, D. C. Johnson, *Inorg. Chem. 56*, **2017**.)[102] DOI: 10.1021/acs.inorgchem.6b03063 Copyright (2017) by the American Chemical Society.

DFT studies on SnV showed that the SnSe energetically favours the to be in line with the vanadium of the VSe_2 layer (Figure 4.14).[110] The resulting 12 fold symmetry has been confirmed by nano-beam electron diffraction (NBED).[101] The preferred orientation can also be seen in high-angle annular dark-field imaging (HAADF)-STEM images of $(SnSe)_{1.15}VSe_2$[101] and $(SnSe)_{1.20}TiSe_2$ (Figure 4.15).[102]
The correlation during the annealing might act as a template for the 12-fold symmetry in 1:1 ferecrystals which correspond to the superstructure c-lattice parameter. The 12 fold symmetry also allows a correlation only for the rock salt layer as the individual TMDs would be distorted to each other. This explains why no correlation reflections could be seen in the reciprocal space map along the $[11l]_{TSe_2}$.
This indicates that the best correlating sample can be prepared with a TMD that only crystallizes in 1T and a rock salt that forms a 2D layered dichalcogenide. The transformation from precursor to the TMD template with mixture of TSe_2-MSe_2-TSe_2 in the 1T polytype and TSe_2-MSe-TSe_2 into TSe_2-MSe-TSe_2 is shown in a schematic free energy landscape as a function of annealing temperature in Figure 4.16.
The TMDs of vanadium[111] and titanium[112] have only been reported in the 1T polytype. $NbSe_2$ can form multiple polytypes in bulk[113] and ferecrystalline materials.[79] As $NbSe_2$ can crystallize in 1T or 2H polytype, the $NbSe_2$ layer has a higher distortion which is reducing its ability to build the template 1T $NbSe_2$-$BiSe_2$-$NbSe_2$ structure. In consequence, the BiNb has less coinciding in-plane lattice parameters.
The TMD of lead and selenium can only be synthesized in a high pressure synthesis (4.5 GPa) at 650 °C, and therefore, there is probably no intermediate in the annealing process.[114] Even if $PbSe_2$ would be formed during the annealing process, it would

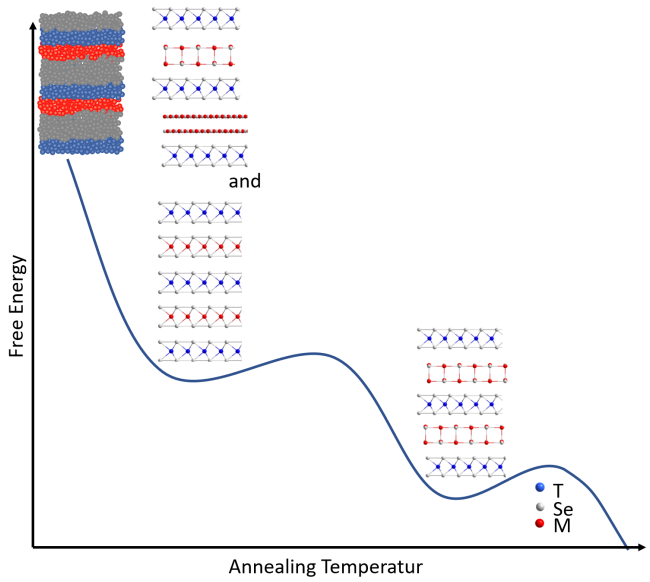

Figure 4.16: Free energy landscape for the transformation of the as deposited precursor into the mixture of TSe_2-MSe_2-TSe_2 and TSe_2-MSe-TSe_2 to the lower energy state with only TSe_2-MSe-TSe_2.

not promote a template crystallization as $PbSe_2$ does not crystallize in a 2D-layered structure.[114]

In line with these preconditions, largest ΔQ (0.0452 Å) is observed for PbV, even though VSe_2 crystallizes only in 1T, and the second smallest ΔQ (0.0093 Å) of the investigated ferecrystals is observed for SnV.

SnTi has a much larger ΔQ (0.0268 Å) than BiTi (0.0006 Å) and SnV (0.0093 Å) which is surprising as the SnSe is able to form a TMD and $TiSe_2$ crystallizes, like VSe_2, only in 1T. In comparison to SnV, the SnSe in SnTi exhibits a peak splitting and therefore a higher offset in ΔQ, as the a and b-lattice parameter deviate below and above b'. Johnson *et al.* showed a transformation from α- to β-SnSe with increasing rock salt layer thickness m.[45,109] Due to a higher Sn content in SnV exhibits SnSe a peak splitting with high Sn/V ratios (1.37).[115] Therefore, might the peak splitting in SnTi be due to a higher Sn content. The different SnSe symmetry in SnTi and SnV might also result from different annealing temperatures. α-SnSe has a temperature dependent change in the ratio of a/b lattice parameters and, above 880 K, a phase transition to β-SnSe.[116]

In consequence, the correlation in 1:1 ferecrystals depends on the ability of the TMD to crystallize in 1T or multiple polytypes and if the rock salt forms a 2D layered dichalcogenide. This templating might then influence the in-plane lattice parameter. It is also possible that the coinciding lattice parameters allow a better formation of a template crystallization of the TMD and the dichalcogenide of the rock salt. There-

fore, a small Δb' seems to be essential for interlayer correlations but not necessarily all 1:1 ferecrystals with $\Delta b' \approx 0$ show interlayer correlations. The ability of the in-plane lattice parameter to be distorted to reduce Δb' might also be important. For example a $(PbSe)_{1+\delta}NbSe_2$ should have a higher ΔQ than $(PbSe)_{1+\delta}VSe_2$ as $NbSe_2$ crystallizes contrary to VSe_2 not only in 1T.
Applying this model on other 1:1 ferecrystals, a high deviation from the ideal value of the misfit parameter (0.155) is expected for ferecrystals with TMDs that form multiple polytypes. This can be seen for $MoSe_2$ (0.03)[97] and WSe_2 (-0.01)[97] compounds but not for all $NbSe_2$ (SnNb 0.136)[117] ferecrystals. Also, PbTi has a misfit parameter of 0.160,[118] even though PbSe is unable to form a 2D layer dichalcogenide. If the proposed model is correct have those ferecrystals with a δ of 0.155 not necessarily a high correlation and therefore should in reciprocal space maps of PbTi reflections of the binary compounds along $[20l]_{PbSe}$ and $[10l]_{TiSe_2}$ be visible.

4.6. Summary

A systematic study of structural interlayer correlations was performed for five different 1:1 ferecrystals by reciprocal space mapping. Additional correlation reflections in these 1:1 ferecrystals were observed, in particular in $[10l]_{TSe_2}$ $[20l]_{MSe}$ and along $[22l]_{MSe}$ reflection series. These additional reflections are associated with interlayer correlations in these particular directions. For samples with a small lattice mismatch in-plane, the $[10l]_{TSe_2}$ $[20l]_{MSe}$ reflections are better aligned in the lateral direction. This indicates that the degree of correlations depends on the lattice mismatch. A correlation with the lateral Q position, *i.e.*, a lateral smearing of the very strong $(00l)$ reflections, could be ruled out as the correlation length in l direction is much different and the Q_z position of the additional reflections does not match the Q_z position of the $(00l)$ superlattice reflections.
For higher order reflections, correlation can only be seen in the rock salt layer indicating that TSe_2 does not nucleate randomly but crystallizes and acts as a template for following layers as proposed by Johnson *et al.*.[31] It is essential for a high degree of correlation that the TMD crystallizes only in the 1T polytype and that the rock salt is able to form a 2D layered TMD as intermediate. The misfit parameters of previously published 1:1 ferecrystals that do not obey this rule but have a low Δb' indicates that a low Δb' does not necessarily mean that a high degree of correlation is present in these samples. Further reciprocal space maps on 1:1 ferecrystals with a low Δb' but a rock salt that is unable to form a 2D TMD like PbV could confirm

that a low Δb' does not necessarily give samples with interlayer correlations.
The results show that correlation of 1:1 ferecrystals is found in all five investigated 1:1 ferecrystals and probably also can be found in other 1:1 ferecrystals with appropriate TMD and rock salt. This is according to the previous work on correlations in 1:1 ferecrystals[31,101,102] and is an important step in understanding the 3D structure and nucleation of multilayered materials containing TMDs, especially ferecrystals.

5. $[(Cu_xCr_ySe_z)_{1+\delta}]_1(NbSe_2)_3$ ferecrystals

5.1. Introduction and aims

In nanolayer synthesis the challenge is the synthesis of materials with a small size distribution and precise control of the structure. Via modulated elemental reactant (MER) method materials with finely, (sub-Å) tunable, monodisperse layer thickness are accessible.[22,119] The MER method allows preparation of nanolaminates with systematically designed compositions.[118] The individual components (typically chalcogenide materials) of these ferecrystals are precisely oriented in the stacking direction (c-axis) but rotationally disordered in plane.
Therefore magnetic ferecrystals are ideal for the investigation of surface and finite size induced structural effects. The typical rock salt in $[(MSe)_{1+\delta}]_m(TSe_2)_n$ (M = Pb, Sn, Bi, or rare earth metal; Te; T = transition metal) was exchanged with the cubic spinel $CuCr_2Se_4$. $CuCr_2Se_4$ thin films have first been prepared by Bettinger *et al.* by pulsed laser deposition (PLD).[57] The X-ray diffraction patterns of the films revealed impurities of $CuCrSe_2$ and $Cr_{2.8}Se_4$. For the preparation of $CuCr_2Se_4$ via the MER method a Se|Cr|Cu|Cr|Se layering scheme is essential to prevent the formation of Cu-Se compounds as reaction intermediates.[46,59] Previous work on $CuCr_2Se_4$ showed that it is possible to prepare phase pure $CuCr_2Se_4$ layers via the MER method.[58,120] These $CuCr_2Se_4$ films were crystallographically aligned with [111] perpendicular to the substrate and had a Curie temperature of 406 K.[58] First experiments indicated that an alternative layering with $NbSe_2$ is possible.[46]
We explored the synthesis of heterostructures within the Cr-Cu-Se-Nb system, focusing on the Se rich phases using modulated elemental reactants in an attempt to control the structure of the products formed.

5.2. Sample calibration and preparation

The $[(Cu_xCr_ySe_z)_{1+\delta}](NbSe_2)_n$ ferecrystals were prepared using a previously reported layering scheme for preparing $CuCr_2Se_4$ with the MER method (Figure 5.1).[46,59] As it is not necessarily that $CuCr_2Se_4$ forms in ferecrystalline materials this layer will be referred to as $Cu_xCr_ySe_z$ in the following.
The deposition parameters for the Nb-Se layers were based on parameters successfully used in prior studies on $[(MX)_m]_{1+\delta}(NbSe_2)_n$. A number of precursors were prepared during the course of this investigation by depositing elemental layers in designed

sequences to probe the potential formation of heterostructures containing alternating layers of $Cu_xCr_ySe_z$ and $NbSe_2$.

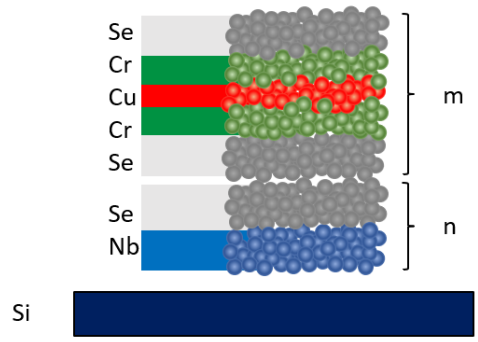

Figure 5.1: Layering scheme for the preparation of $(Cu_xCr_ySe_z)(NbSe_2)_n$.

As explained in chapter 3.3 $CuCr_2Se_4$ has a preferential formation along [111] with a double layered structure if a c-lattice parameter of 12 Å is considered. To determine the constituent c-lattice parameters samples with 1, 3 and 5 $NbSe_2$ layers were prepared. The Nb|Se deposition parameters were used as previously calibrated by the Johnson group. Tooling factors and deposition rates were inherited from previous calibrations performed in the Johnson group. For Cu|Se|Cr arbitrary starting values were tested. By plotting the change in c-lattice parameter vs. the number of $NbSe_2$ layer (Figure 5.2) the individual constituent c-lattice parameters can be calculated from the linear trend given that the choosen parameters are roughly in the range. The slope of the trend line is 6.31 Å and corresponds to the c-lattice parameter of $NbSe_2$ and is close to the bulk value of 6.29 Å. The y-axis intercept corresponds to the $Cu_xCr_ySe_z$ c-lattice parameter and is with 12.31 Å slightly larger than what would be expected from the bulk material. Even though the constituent lattice parameters are close to the desired values, a lot of $(00l)$ reflections in the samples are not visible indicating a poor crystallinity and that further optimization of the deposition parameters is necessary.

Therefore the amount of niobium and selenium deposited in Få was kept constant and the Cu/Cr ratio deposited was systematically varied to obtain highly crystalline samples. Preliminary experiments revealed that samples with a m:n ratio 1:3 are the best choice to prepare a crystalline sample. Therefore the 1:3 sample was used to calibrate the Cu/Cr ratio.

To optimize the Cr deposition parameters samples with copper thickness of 2.1 and 2.9 Få and varying chromium thickness were prepared (Figure 5.3). The goal were samples with the best crystallinity *i.e.* samples with most $(00l)$ reflections that have a high intensity and are sharp. For the samples with a copper layer thickness of

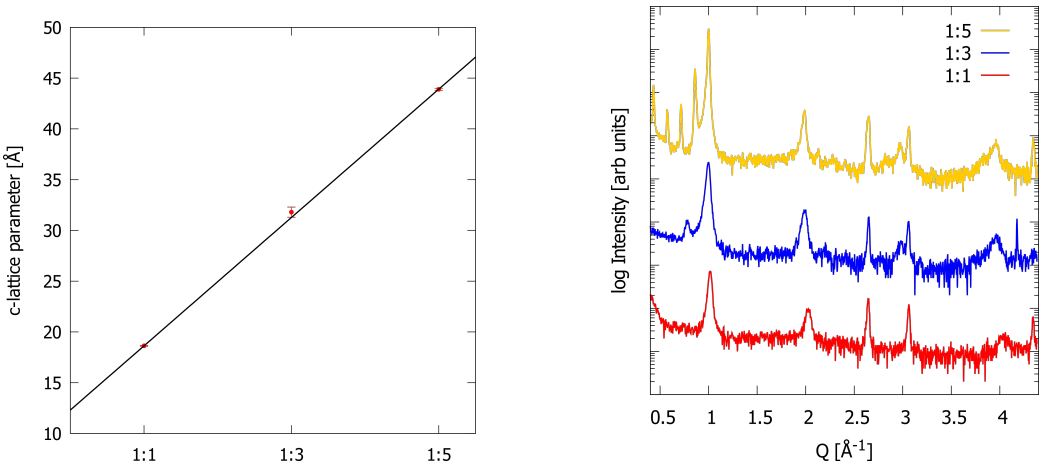

Figure 5.2: Change in c-lattice parameter vs. the number of $NbSe_2$ layers (left). Specular diffraction pattern (right).

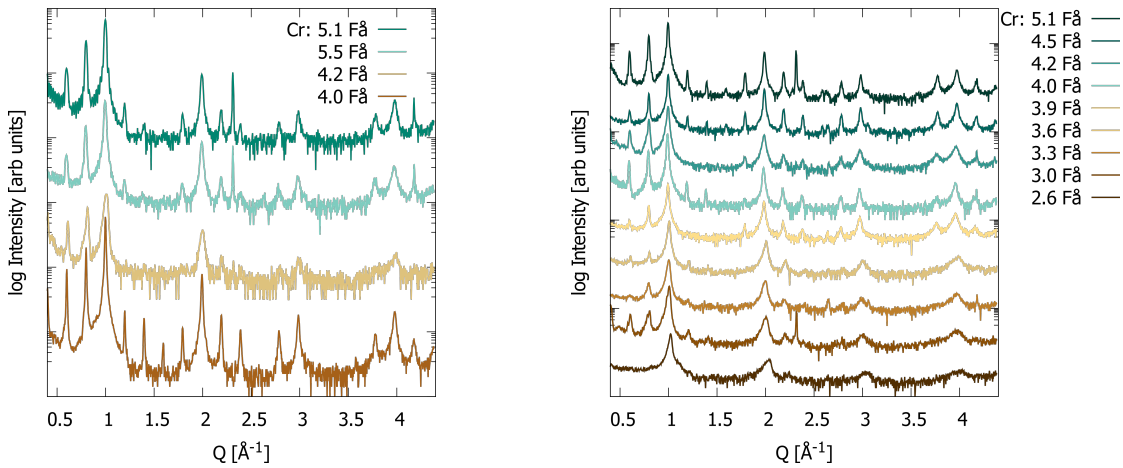

Figure 5.3: Specular diffraction patterns of samples with varying chromium layer thickness in Få and constant copper layer thickness. 2.1 Få of copper (left) and 2.5 Få of copper (right).

2.1 Få a chromium layer of 4.0 Få gave the best result, for a copper layer thickness of 2.9 Få 5.1 Få of chromium gave the best sample. The formation of secondary phases would be expected for samples with thicker copper layers than 2.5 Få (pure copper or $CuSe_2$) and for samples with a copper layer thinner than 2.1 ($CrSe_2$).

Comparing those two samples directly (Figure 5.4) it can be seen that samples with 2.1 Cu Få and 4.0 Cr Få give the best crystallinity. The used parameters for sample preparation are given in Table 5.1.

Additional samples with slightly different deposition parameters were prepared as the screening for optimal deposition parameters showed that variation in a huge range of deposition parameters gave crystalline materials. The used parameters and the corresponding samples are given in table 5.1.

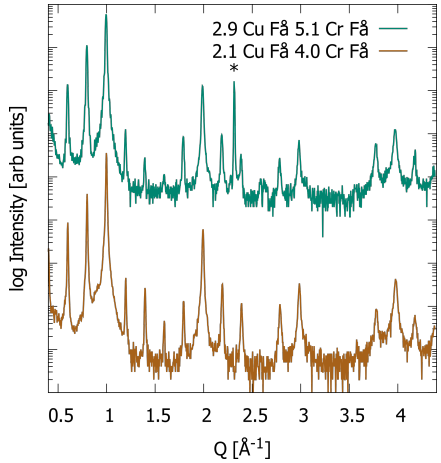

Figure 5.4: Specular diffraction patterns of the samples with 2.9 Cu Få, 5.1 Cr Få (left) and 2.1 Cu Få, 4.0 Cr Få (right). * = silicon

Table 5.1: Parameters for preparation of $[(Cu_xCr_ySe_z)_{1+\delta}]_1(NbSe_2)_n$ samples

	sample 1 and 4			sample 2 and 3			sample 5		
	Få	Rate	Tooling Factor	Få	Rate	Tooling Factor	Få	Rate	Tooling Factor
Nb	7.7	0.2	64	7.8	0.2	64	7.8	0.2	64
Se	8.3	0.5	65	8.3	0.5	68	8.3	0.5	68
Se	7.4	0.5	65	7.4	0.5	68	7.4	0.5	68
Cr	5.1	0.2	64	3.3	4.0	0.2	64	0.2	64
Cu	4.1	0.2	64	4.5	2.1	0.2	64	0.2	64
Cr	5.1	0.2	64	3.3	4.0	0.2	64	0.2	64
Se	7.4	0.5	65	7.4	7.4	0.5	68	0.5	68

5.3. Annealing study

An annealing study was performed to determine the changes in structure as a function of temperature and time. The annealing time and temperature as well as the coherence of the obtained heterostructure were optimized. The annealing studies were performed with $[Se|Cr|Cu|Cr|Se]_1[Nb|Se]_3$ precursors in a glove box with nitrogen atmosphere with O_2 and H_2 concentration below 0.5 ppm. For annealing the samples were heated heated on a costume made hot plate to temperatures between 100 and 600 °C. During the annealing the sample was covered with a clean silicon-wafer to reduce the selenium loss. After each annealing step X-ray reflectivity and X-ray diffraction patterns were taken, and the total thickness and c-lattice parameter are determined.

Figure 5.5 shows the time dependent X-ray reflectometry and diffraction patterns with

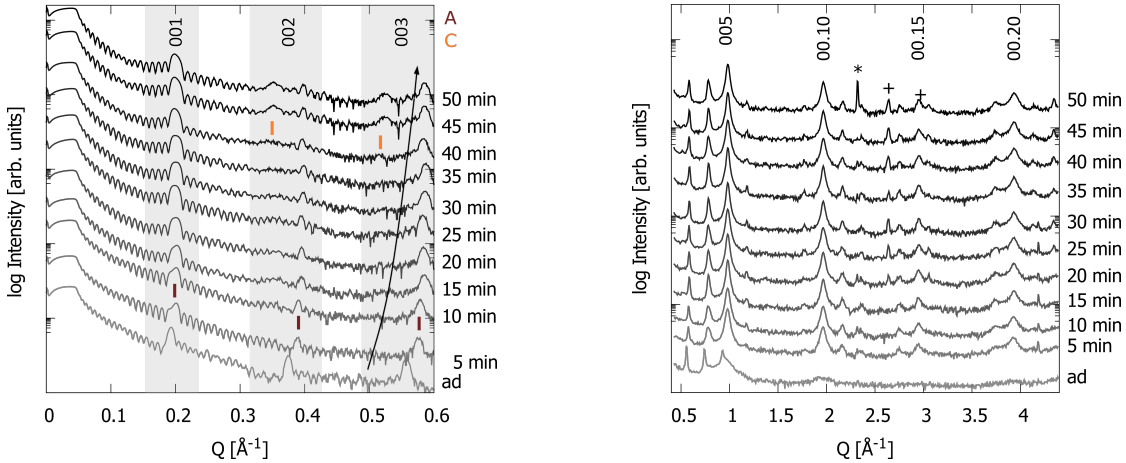

Figure 5.5: X-ray reflectometry (left) and diffraction patterns (right) obtained after different annealing times of sample 1 $[(CuCr_xSe_y)_{1+\sigma}]_1[NbSe_2]_3$ at 400 °C reflections of secondary phase are indexed in italic. Heterostructures A and C are indexed as brown and orange lines, respectively. * = silicon, + = stage

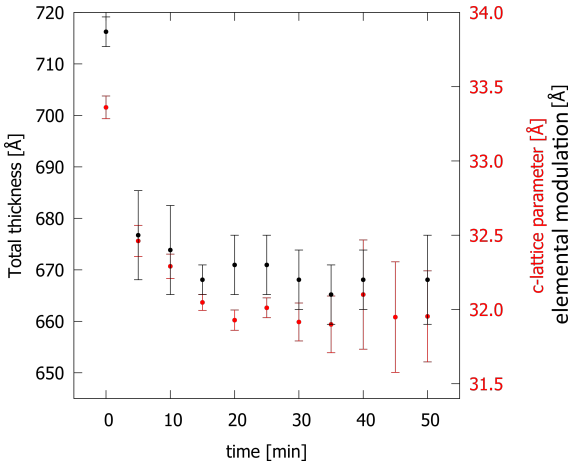

Figure 5.6: Total thickness and elemental modulation / c-lattice parameter as a function of time.

indexed $(00l)$ reflections. One piece of sample 1 was annealed at 400 °C in 5 min steps. Uniform Kiessig fringes and the first five Bragg reflections in the as-deposited material indicate that the precursor already is nicely layered with a repeating thickness of 33.9(1) Å and contains significant order. With increasing annealing time additional reflections appear, reflections sharpen, and the intensity of the $(00l)$ reflections increases indicating optimization of crystallographic alignment of the film along the modulation axis. The c-lattice parameter as well as the total thickness (Figure 5.6) reduce with increasing temperature due to loss of excess selenium and increasing crystallinity, *i.e.* a more efficient packing of the atoms in the structure. After annealing for 5 min already additional reflections appear and the c-lattice parameter decreases. After 30 min all reflections can be indexed as $(00l)$ reflections of a common superlat-

tice, indicating that this is the optimum annealing time for 400 °C. The heterostructure A formed after 30 min of annealing and has a c-lattice parameter of 32.2(2) Å. After 35 min two new reflections appear in the XRR scan, indicating the formation of heterostructure C with a larger c-axis lattice parameter of 36.13(6) Å based on indexing them as the 2nd and 3rd order reflections.

By varying the annealing time the system evolves into two heterostructure. The calculated total thickness obtained from the Kiessig fringes and the thickness of the elemental modulation determined from the sharp reflections present at low Q in the as deposited sample and after short annealing times, and the c-axis lattice parameter from the crystalline heterostructures that form during the annealing over time are given in Figure 5.6.

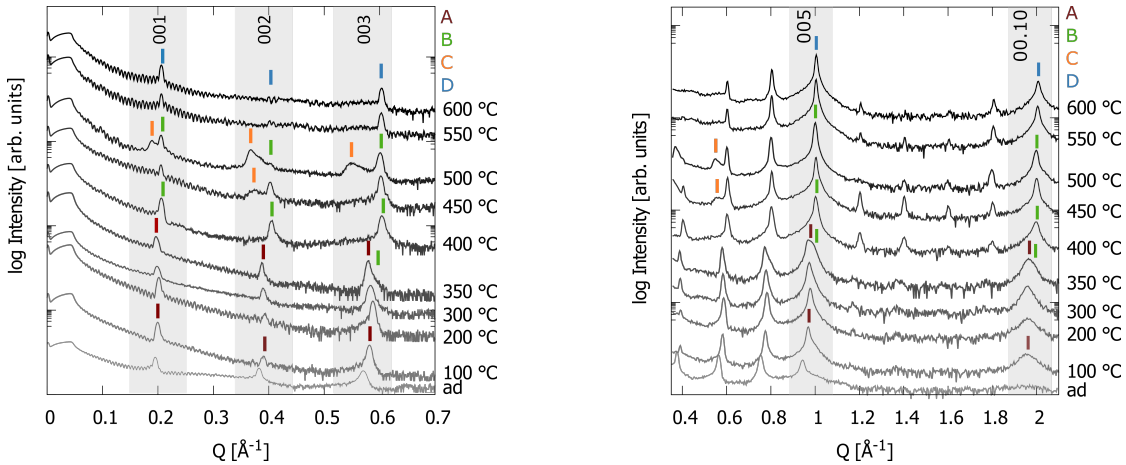

Figure 5.7: X-ray reflectometry (left) and diffraction patterns (right) obtained after different annealing temperatures of sample 2 $[(CuCr_xSe_y)_{1+\sigma}]_1(NbSe_2)_3$.

Considering the complexity of the evolution of the precursor as a function of time, an annealing study was performed on sample 2 to determine the impact of annealing temperature on structures that are formed. Nine individual samples were heated on a hot plate to different temperatures for 30 min (Figure 5.7). In the temperature range of 100 to 600 °C four distinct structural transitions are observed in the XRR and XRD (Figure 5.7) and the derived total thickness and c-lattice parameter (Figure 5.8 right).

Low temperature annealing at 100 and 200 °C transforms the as deposited material into heterostructure A with a smaller c-lattice parameter. Heterostructure A has the highest amount of reflections and the highest intensity by annealing at 300 °C. The c-lattice parameter of the material decreases about 1 Å from 33.20(4) Å in the precursor to 31.95(3) Å in heterostructure A. Increasing the annealing temperature to

300 - 400 °C further the c-lattice parameter decreases and heterostructure A (indexed in brown in Figure 5.7 left) transforms to heterostructure B (indexed in green in Figure 5.7 left). The c-lattice parameter of heterostructure B (31.50(7) Å) is about 0.5 Å smaller than heterostructure A. The reflections of heterostructure B sharpen by annealing at 450 °C. A third heterostructure C forms between 400 and 500 °C with a larger c-lattice parameter (indexed in orange in Figure 5.7 left). The XRR at 500 °C has less uniform Kiessig fringes at low Q due to an increased surface roughness because heterostructure B and C coexist. By annealing to 600 °C heterostructure C is eliminated and a heterostructure D (indexed in blue in Figure 5.7 left) with a c-lattice parameter similar to heterostructure B forms. The formation of the different heterostructures is visualized by colour blocks in Figure 5.8.

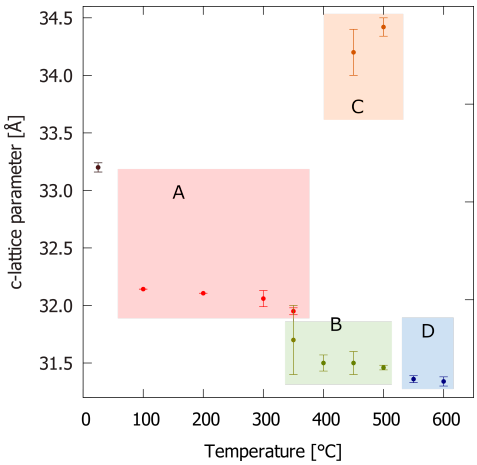

Figure 5.8: Total thickness (gray) and c-lattice parameter as function of annealing temperature. The c-lattice parameters are plotted in the colour of the corresponding heterostructures A red, B green, C orange, and D blue.

5.4. Heterostructure formation in a broader set of samples

A third sample (3) was prepared with the same parameters as sample 2 to determine the reproducibility of the sample preparation and heterostructure formation in a broader set of samples. Sample 3 was divided into three pieces, one annealed at 350 °C to form heterostructure A, one annealed at 400 °C to form heterostructure B and one annealed to 600 °C to form heterostructure D. The influence of different Cu/Cr ratios on the heterostructures were investigated. Therefore samples with three different Cu/Cr (0.96, 1.19, 1.8) ratios were prepared.

The diffraction patterns of the three heterostructures A, B and D of sample 3 are given in Figure 5.9. The different annealing conditions clearly produce samples with

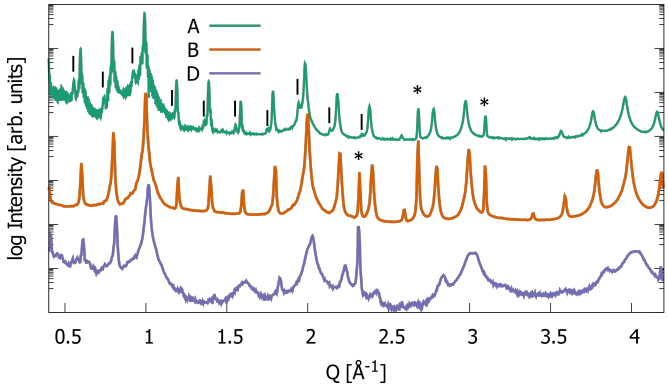

Figure 5.9: Specular diffraction pattern in the range of 0.4 - 4.5 $Å^{-1}$ for the $[(CuCr_xSe_y)_{1+\sigma}]_1[NbSe_2]_3$ compound of sample 3 with heterostructure A, B, and D. Heterostructure C is indicated by vertical lines. * = sample holder

different c-lattice parameters. This can be seen in the offset to higher Q for heterostructure A relative to that for heterostructure B. For heterostructure A of sample 3, reflections of heterostructure C can be seen, which has a significantly higher intensity than observed in the sample prepared from precursor 2 (5.10 right). The reflections of heterostructure C might not be visible due to the lower resolution of the XRD data of sample 2 A. Sample 2 was measured on an in house diffractometer and sample 3 at the ID03 instrument at the ESRF. Comparing the c-lattice parameters of the samples prepared from precursor 2 and 3, we find that the as deposited material has a slightly smaller c-lattice parameter for sample 3 and the c-lattice parameters of all heterostructures are slightly smaller (Table 5.2).

Table 5.2: c-lattice parameters of samples 2 and 3 and their corresponding heterostructures.

	c-lattice parameter [Å]			
	A	B	C	D [Å]
Sample 2	33.20(4)	31.50(7)	34.34(8)	31.34(4)
Sample 3	31.77(2)	31.48(1)		31.1(1)

Figure 5.10 compares the samples 2 and 3 annealed at 350 °C with heterostructure A and the samples 2 and 3 annealed at 400 °C with heterostructure B. The higher background for sample 2 A and 2 B is due to the lower resolution of the measurement. Both samples 3 A and B have a different intensity profile in comparison to their corresponding sample 2. This reflects the potentially different composition and thickness of the precursor and our limits on reproducing the deposition process.
Likewise a sample was prepared with the same parameters as sample 1. This sample 4 differs from sample 3 in the amount of copper and chromium that was deposited.

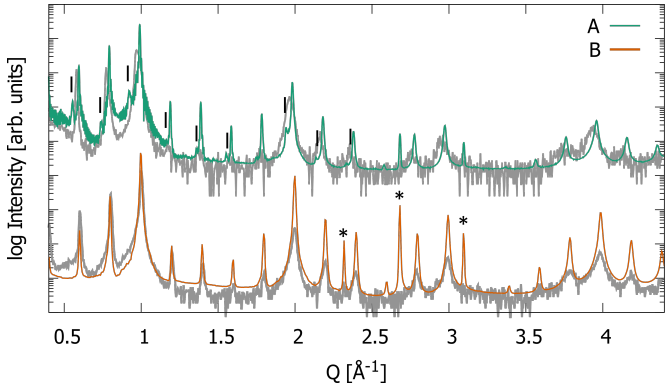

Figure 5.10: Specular diffraction pattern in the range of 0.4 - 4.5 $Å^{-1}$ for the $[(CuCr_xSe_y)_{1+\sigma}]_1[NbSe_2]_3$ compound of sample 2 (grey) and 3 (colour) with heterostructure A and B. Heterostructure C is indicated by vertical lines. * = sample holder

Additionally a fifth sample (sample 5) was prepared with a third variation in copper and chromium deposition parameters than sample 3 and 4 aiming for higher Cu/Cr ratio. To determine the Cu/Cr ratio XRF measurements of sample 3, 4 and 5 were performed. The results of the XRF measurements are summarized in table 5.3. The three different samples have similar Se/Nb ratios as their deposition parameters where not varied. The Cu/Cr ratio of the sample increases from sample 3 to 5.

Table 5.3: Cu/Cr and Se/Nb atomic ratios determined by XRF.

	sample 3 A	sample 4 B	sample 5 B
Cu/Cr	0.96	1.19	1.85
Cu/Nb	0.03	0.05	0.04
Cr/Nb	0.03	0.04	0.02
Se/Nb	2.60	2.69	2.50

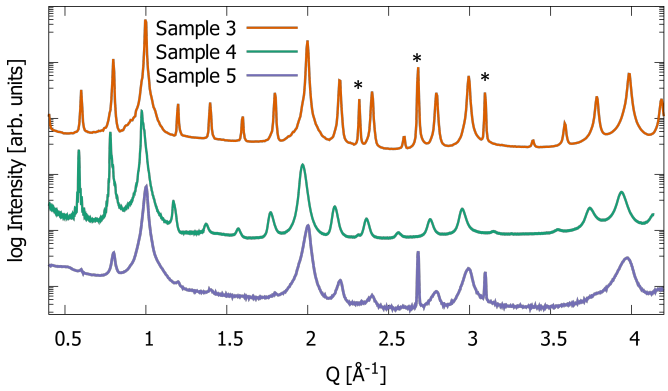

Figure 5.11: Specular diffraction pattern in the range of 0.4 - 4.5 $Å^{-1}$ for the $[(CuCr_xSe_y)_{1+\sigma}]_1[NbSe_2]_3$ compounds 3, 4 and 5 annealed at 400 °C. * = sample holder

The intensity profiles of sample 3, 4, and 5 differ due to the variation in Cu/Cr ratio (Figure 5.11). The Cr/Nb and Cu/Nb ratios have been increased from sample 3 to sample 4. Sample 5 has completely different Cu/Cr ratio and a lower Cr/Nb ratio than sample 3 and 4 but only a slight offset in the reflection position. Sample 3, 4, and 5 have visible $(00l)$ reflections to wide Q range, this shows that over a wider range of copper and chromium ratios a crystalline material could be obtained. For sample 4 are a lot of $(00l)$ reflections are not visible indicating a poorer crystallinity than in sample 3 and 4.

Figure 5.12 gives the evolution of the c-lattice parameter with temperature of the samples 3, 4, and 5. All three samples show a temperature dependent change in c-lattice parameter similar to sample 2. This indicates that in the prepared range of Cu/Cr ratio it is possible to form the different heterostructures A to D by varying the annealing temperature. A table with the c-lattice parameters of the samples 3, 4, and 5 at varying annealing temperatures can be found in the appendix chapter B.1.

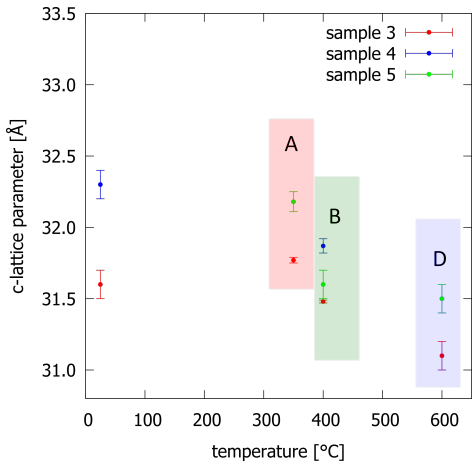

Figure 5.12: c-lattice parameter as a function of temperature for sample 3, 4, and 5. The corresponding heterostructures are marked by coloured boxes.

For sample 5 a lot of $(00l)$ reflections are not visible indicating a poorer crystallinity (Figure 5.13). The sample annealed at 600 °C has more visible reflections than the sample 2 A and B. Due to the higher Cu/Cr ratio more energy might be needed to form material with a good crystallinity. Johnson *et al.* showed for SnSe that excess material migrates out of the sample to the surface.[109] This might be the case for sample 5 D indicating that the Cu/Cr ratio of sample 5 is the upper limitation for the production of a crystalline sample under the applied conditions. It also possible that for the Cu/Cr ratio in sample 5 the selenium content in the $Cr_xCu_ySe_z$ layer is too high and a higher annealing temperature than 400 °C or a longer time is needed to evaporate the excess selenium. The Cr/Nb ratio of 0.2 might too low to form a smooth

homogeneous $Cu_xCr_ySe_z$ layer in every unit cell, this explains the low crystallinity in the sample.

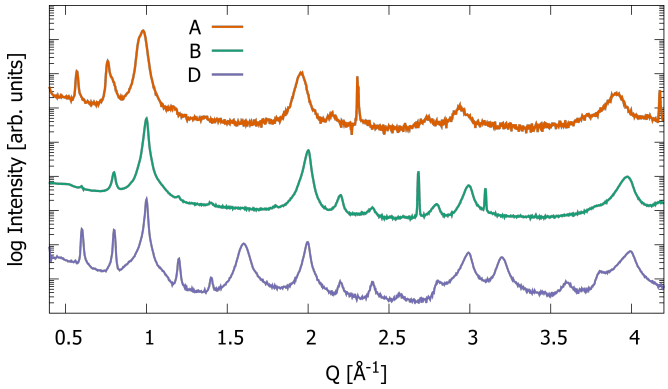

Figure 5.13: Specular diffraction pattern in the range of 0.4 - 4.5 $Å^{-1}$ for the $[(CuCr_xSe_y)_{1+\sigma}]_1[NbSe_2]_3$ compound of sample 5 with heterostructure A, B, and D. * = sample holder

5.5. Structural investigation of the in-plane structure

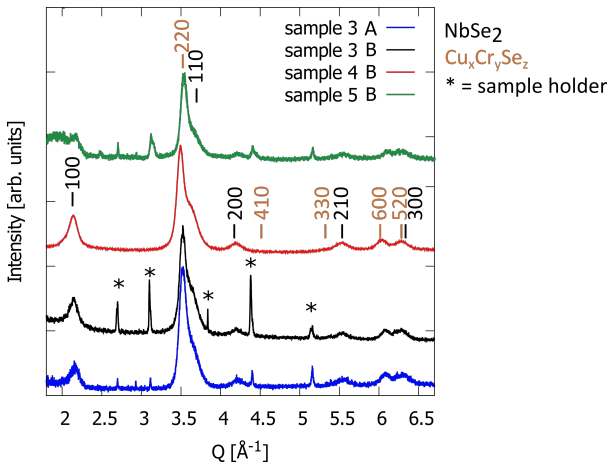

Figure 5.14: In-plane diffraction patterns of sample 3, 4, and 5 with heterostructure B and sample 3 with heterostructure A .

Further structural information of the samples 3, 4, and 5 was obtained from in-plane diffraction patterns. Due to the formation of heterostructure A and B, it was investigated, if the change in superstructure c-lattice parameter, due to the formation of heterostructure A and B, also has an effects on the a-lattice parameter. Further, the effect of the Cu/Cr ratio on the in-plane lattice parameters was investigated.

Sample 3 A (annealed at 350 °C) and 3 B (annealed at 400 °C) and sample 4 B and 5 B (annealed at 400 °C) where probed with in-plane X-ray diffraction (Figure 5.14). The lattice parameters were obtained by the Le Bail method.[121] The detailed results

of the Le Bail fitting are presented in appendix chapter D.2. The two constituents can be indexed independently which is characteristic for ferecrystalline materials.[108] All reflections can be indexed as ($hk0$) reflections of a hexagonal plane for either $Cu_xCr_ySe_z$ or $NbSe_2$.
For indexing the cubic spinel $Fd\bar{3}m$ was transformed along [111] direction into a hexagonal subgroup $R\bar{3}m$.
The a-lattice parameters for the $Cu_xCr_ySe_z$ (given in Table 5.4) are slightly smaller than for the hexagonal transformation of the bulk $CuCr_2Se_4$ material (7.31 Å).[56] All a-lattice parameters for $Cu_xCr_ySe_z$ are larger than the reported bulk value for $CrSe_2$ (3.399 Å).[122] An additional candidate for the $Cu_xCr_ySe_z$ compound is $CuCrSe_2$, with an a-lattice parameter nearly 1/2 of the obtained lattice parameter (3.679 Å),[123] (compare table 5.4). The obtained in-plane lattice parameters indicate that the compound is not $CrSe_2$, but might be either a $Cu_{0.5}CrSe_2$ or a $CuCr_2Se_4$ analogue with varying Cu/Cr content.
$NbSe_2$ is indexed with the hexagonal space group $P\bar{3}m1$. Ferecrystals give in in-plane geometry only ($hk0$) reflections and therefore there is no information for the packing symmetry of $NbSe_2$ along the c-axis accessible with in-plane diffraction. Because of that the use of the higher symmetry space group $P6_3/mmc$ of $NbSe_2$ is not reasonable and usually all dichalcogenides in ferecrystals are indexed with $P\bar{3}m1$. All a-lattice parameters for the $NbSe_2$ compound (given in Table 5.4) are larger than the reported bulk value (3.4461 Å)[124] or the copper intercalation product $Cu_{0.667}NbSe_2$ (3.487 Å),[125] indicating a rather high degree of copper intercalation into the $NbSe_2$ layer.
The annealing temperature for sample 3 has no effect on the $NbSe_2$ a-lattice parameter and only affects the second decimal place of the $Cu_xCr_ySe_z$ a-lattice parameter (Table 5.4). The different samples with heterostructure B show that the $NbSe_2$ a-lattice parameter is not linked to the Cu/Cr ratio in the sample. $Cu_xCr_ySe_z$ a-lattice parameter shows some slight variation with changing Cu/Cr ratio but the ratio of $Cu_xCr_ySe_z$ a-lattice parameter and c-lattice parameter of the superstructure are almost the same for the three different samples (Table 5.5). This shows that the total volume of the $Cu_xCr_ySe_z$ layer is not effected by the Cu/Cr ratio but the varied occupation with copper and chromium effects the a- and c-lattice parameter differently.

Table 5.4: Calculated a-lattice parameters and misfit parameter of the 1:3 samples 2 and 3 and their corresponding heterostructures along with literature values for bulk materials.

	space group	$Cu_xCr_ySe_z$ a [Å]	$NbSe_2$ a [Å]	misfit δ
Sample 3 A		7.293(3) 3.646	3.508(6)	0.463
Sample 3 B		7.258(9) 3.629	3.504(6)	0.466
Sample 4 B		7.30(1) 3.65	3.501(9)	0.460
Sample 5 B		7.228(9) 3.614	3.526(6)	0.476
$CuCr_2Se_4$[56]	$Fd\bar{3}m$	10.337		
$CuCr_2Se_4$	$R\bar{3}m$	7.31		
$CrSe_2$[122]	$P\bar{3}m1$	3.399		
$CuCrSe_2$[123]	$R3m$	3.679		
$NbSe_2$[124]	$P6_3/mmc$		3.4461	
$Cu_{0.667}NbSe_2$[125]	$P6_3/mmc$		3.487	

Table 5.5: Ratio of $Cu_xCr_ySe_z$ a-lattice parameters and superstructure c-lattice parameter for samples 3 A, 3 B, 4 B and 5 B.

	a / c
Sample 3 A	0.230
Sample 3 B	0.231
Sample 4 B	0.229
Sample 5 B	0.229

5.6. Scanning transmission electron microscopy

To get a better insight into the layering and lattice parameters of the films High-angle annular dark-field - scanning transmission electron microscope (HAADF-STEM) images of sample 3 and 4 with heterostructure B were collected. The local composition of the films was investigated by EDX-line scans.

HAADF-STEM images were collected from sample 3 which was expected to form heterostructure B, a representative image is shown in Figure 5.15 (left). The STEM images reveal distinct and regularly ordered layers along the c-axis with a double layer structure with four selenium layers. The distinct layering can clearly be seen in the plot of the gray value in the STEM as function of distance (Figure 5.15, right). Since $CuCr_2Se_4$ forms with its [111] plane parallel to the surface, the number of potential ways to slice the cubic structure into layers is limited. Previous reports on V_3Se_4 showed that the structures terminated on its Se plane.[126] Therefore the bulk

$CuCr_2Se_4$ structure has two possible atomic arrangements along the 111 axis, with four selenium layers, a chromium- or a copper-deficient structure, $Cu_1Cr_{1.25}Se_4$ and $Cu_{0.5}Cr_{1.75}Se_4$, respectively (Figure 5.16). The two parts of the bulk structure differ in the occupation and atomic positions. Both structural models would result in a double layer structure.

The distinct layering can also be seen in the gray value plot (Figure 5.15 right). Due to the atomic number contrast,[127] the $NbSe_2$-layers appear much brighter than the $Cu_xCr_ySe_z$-layers ($Z_{Cu} = 29$, $Z_{Cr} = 24$, $Z_{Nb} = 41$). Due to the turbostratic disorder of the nanolaminate material, the in-plane orientation of the layers parallel to the beam may vary, resulting in varying brightness of the layers.

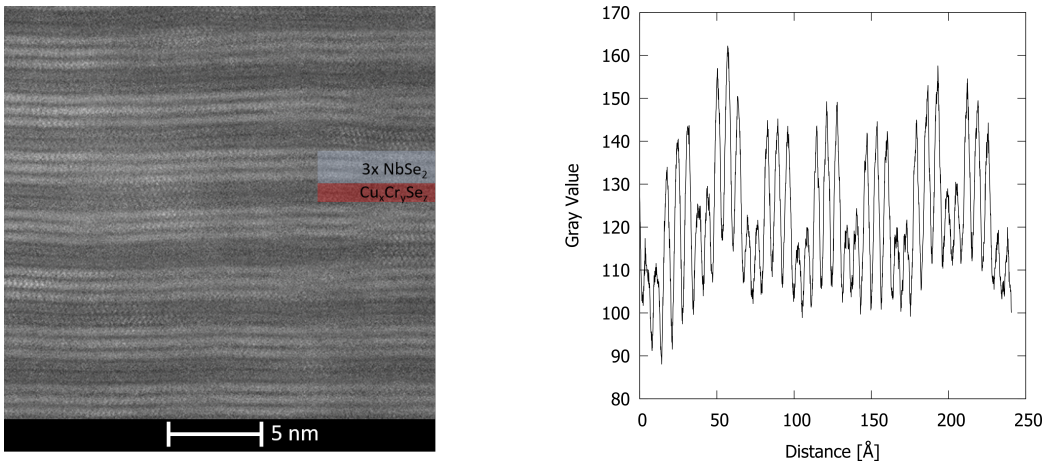

Figure 5.15: Representative STEM image of sample 3 (left). Plot of the Gray value in the STEM image vs. the distance in Å (right).

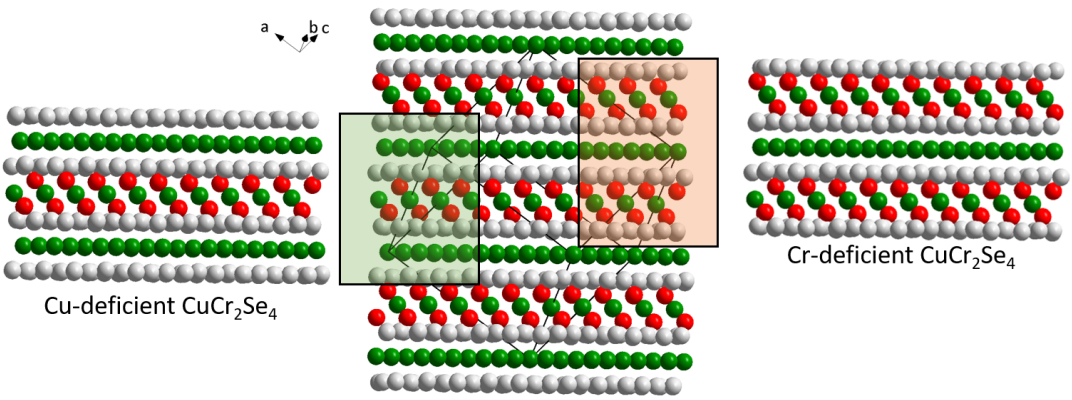

Figure 5.16: Structural models of the Cu deficient $CuCr_2Se_4$ and Cr deficient $CuCr_2Se_4$.

EDX line scans (Figure 5.17 right) suggest as expected a structure of a double layer of chromium in the $Cu_xCr_ySe_z$ phase, whereas a less occupied chromium layer in-between cannot be excluded. As expected, three niobium positions are observed in

the $NbSe_2$ phase, with potentially a small amount of niobium in the chromium layer. The EDX line scans also reveal that copper has likely diffused over the whole material. Whereas copper diffusion is a known issue[66] especially in thin films,[67,68] the amount of copper detected here might have been affected by the Cu TEM grid used, despite careful background correction.

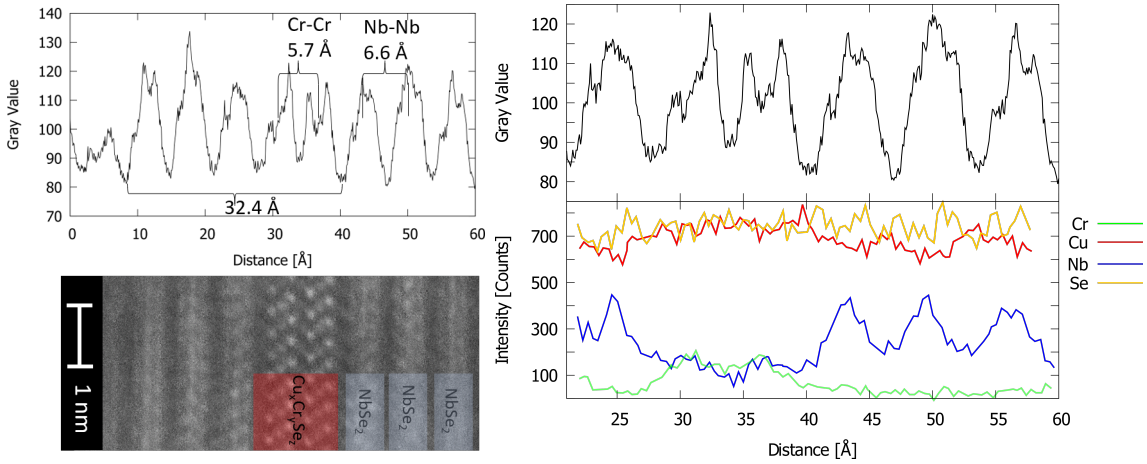

Figure 5.17: Representative STEM image of sample 3 together with plot of the Gray value in the STEM image vs. the distance in Å (left). EDX maps and corresponding Gray value vs. the distance in Å (right).

Atomic distances along the c-axis were measured from the gray value profile (Figure 5.17 left) to compare with the diffraction data. The chromium in the $Cu_xCr_ySe_z$ layer has to be in the centre of one $Cu_xCr_ySe_z$ regardless of the structure is copper deficient $CuCr_2Se_4$, chromium deficient $CuCr_2Se_4$, $CuCrSe_2$ or $CrSe_2$. Therefore, the plots of the gray values in the STEM can be used to determine the Cr-Cr distance. The measured atomic distances and bulk values for comparison are given in table 5.6. The measured Cr-Cr distance is 5.8(3) Å which is in the range of $CrSe_2$.[122] The Cr-Cr distance also matches to $CuCr_2Se_4$ assuming a third chromium layer in-between the two chromium layers. The Nb-Nb distance is 6.7(3) Å and larger than the Nb-Nb distance in the bulk material[124] and previously published $[(MSe)_1]_{1+\delta}(NbSe_2)_3$[32,55,128] ferecrystals. The larger Nb-Nb distance might be due to copper intercalation into $NbSe_2$ as EDX data indicate a copper diffusion into the $NbSe_2$ layers. $Cu_{0.667}NbSe_2$ has a Nb-Nb distance of 6.82 Å which is in the range of the measured Nb-Nb distance. This confirms that the $NbSe_2$ layers have an enlarged unit cell due to copper intercalation.

$Cu_xCr_ySe_z$ layer has a double layer structure with four selenium layers. The Cr-Cr atomic distance of 5.7 Å is in the range of $CrSe_2$. The Cr-Cr distance also matches $CuCr_2Cr_4$ assuming a third chromium with a lower occupation in-between the two

chromium layers. This indicates that the $Cu_xCr_ySe_z$ layer is a Cu_xCrSe_2 double layer or $CuCr_2Cr_4$.

Table 5.6: Cr-Cr and Nb-Nb distances in Å along the c-axis for different bulk and thin film materials.

	Cr-Cr distance [Å]		Nb-Nb distance [Å]
$CuCr_2Se_4$[56]	2x = 5.95	$NbSe_2$[124]	6.29
$CuCrSe_2$[123]	6.46	$Cu_{0.667}NbSe_2$[125]	6.82
$CrSe_2$[122]	5.92		
$CuCr_2Se_4$[58]	2.98	$n = 3$ $NbSe_2$[128]	6.28
thin film	2x = 5.97	ferecrystals	

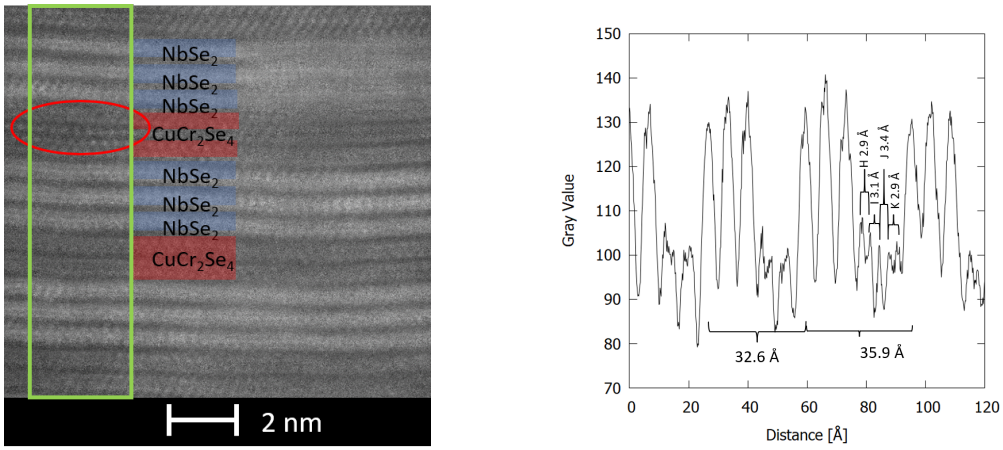

Figure 5.18: Representative STEM image of sample 3 (left). An additional layer is marked by a red ellipsoid. Area in green box was used for plot of the Gray value in the STEM image vs. the distance in Å (right).

In a small part of the sample an additional layer in the $Cu_xCr_ySe_z$ phase was observed (red mark in Figure 5.18), which can be either a stacking fault or a secondary phase in the material. The interplanar distances H and K in the thicker $Cu_xCr_ySe_z$ layer are in range of 2.9 - 3.1 Å and very similar (H, I and K in Figure 5.18) to the Se-Se distances in $CuCrSe_2$. Se-Se distances in $CuCr_2Se_4$ and $CrSe_2$ are between 2.9 and 3.0 Å indicating that the secondary phase might consist of an additional selenium layer. This secondary phase might be heterostructure C as this heterostructure has a slightly larger c-lattice parameter than heterostructure B. The X-ray diffraction patterns give no evidence that heterostructure C is present next to heterostructure B in sample 3 annealed at 400 °C. This could be due to low concentration of heterostructure C.
Figure 5.19 (left) shows the STEM (ER-C) image of sample 4 annealed at 400 °C.

Same as sample 3 sample 4 shows distinct layers with a double layered structure for the $Cu_xCr_ySe_z$ layer similar to sample 3. The gray value profile gives a larger c-lattice parameter for the superstructure which is according to the $(00l)$ data of sample 4. The Cr-Cr distance is with 6.1 Å slightly larger than the Cr-Cr distance in sample 3 (5.7 Å). As the Cr-Cr distances in $CuCrSe_2$, $CrSe_2$, and $CuCr_2Se_4$ are rather similar an assignment of the structures based on the Cr-Cr distance is not possible. The Se-Se distance in a $Cu_xCr_ySe_z$ single layer Figure 5.19 (right) corresponds to the Se-Se distance in $CuCrSe_2$, $CuCr_2Se_4$ and $CrSe_2$. The Nb-Nb distance in sample 4, as shown for sample 3, is larger than the bulk value. The larger Nb-Nb distance indicates that the copper intercalation into the $NbSe_2$ layer also occurs in sample 4.
Sample 3 and 4 have the same stacking along the c-axis and the individual layers have similar distances although their c-lattice parameters are slightly different and they were prepared with different deposition parameters. This shows that slight variations in the atomic composition of the precursor do not change the layering in the sample and only have a small effect on the atomic distances. Similarly, Johnson *et al.* revealed that SnV ferecrystals exhibit a change in atomic distances if the Sn/V ratio is varied but keep the atomic layering scheme.[115] This suggests that the heterostructure B can be prepared in a wide range of Cu/Cr ratios. Which is surprising as only small variations in the annealing temperature are needed to transform the heterostructure B into heterostructure C and D.

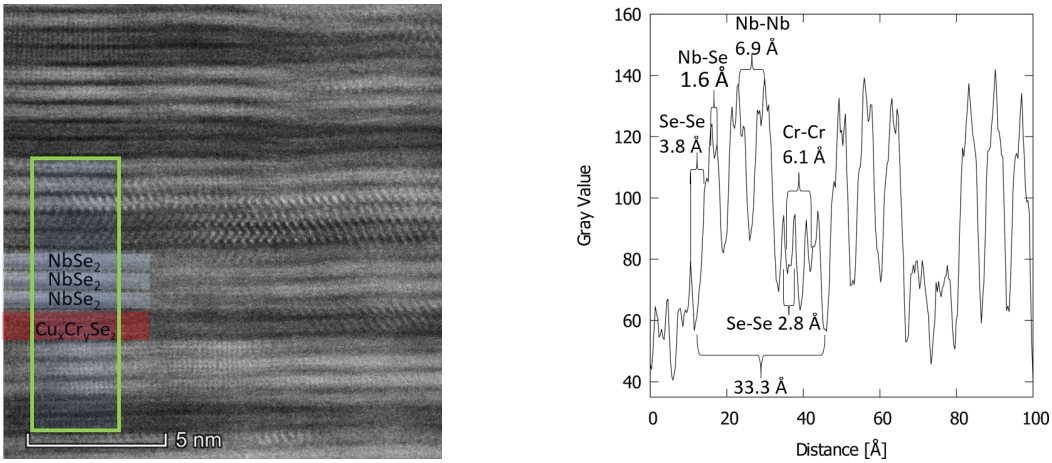

Figure 5.19: Representative STEM images of sample 4 annealed at 400 °C (left). Area in green box was used for plot of the gray value in the STEM image vs. the distance in Å (right).

5.7. Summary

A new set of ferecrystals has been successfully prepared, were the usual rock salt phase was exchanged by a $Cu_xCr_ySe_z$ layer. These new ferecrystals allow the preparation of four structurally different heterostructures by varying the annealing temperature. This is the first ferecrystalline material which gives access to multiple heterostructures depending on the used annealing temperature. The precise transition temperatures of the heterostructures and if two heterostructures are present at the same annealing temperature could be revealed by further, high resolution, temperature dependent X-ray diffraction studies.

X-ray diffraction patterns revealed that the reproducibility of the samples is not perfect due to limitations of the used deposition system. Samples with three different Cu/Cr ratios were prepared with distinct variations in the c-lattice due to the variation of the Cu/Cr ratio. Heterostructures A, B, and D could be prepared in all investigated samples regardless of the Cu/Cr ratio.

In contrast to the superstructure c-lattice parameter, the in-plane lattice parameters are not affected by the transformation into the different heterostructures or the Cu/Cr ratio. The a-lattice parameters of $NbSe_2$ indicate a copper intercalation into the $NbSe_2$ layers as the a-lattice parameter is in comparison to the bulk values considerably enlarged. Copper intercalation into TMDs especially $NbSe_2$ is a known phenomenon[65,66] as copper has a high tendency to diffuse through nanolayers[67–69] and even bulk materials.[65] The in-plane lattice parameters of the $Cu_xCr_ySe_z$ double layer do not allow an unambiguous assignment of the crystal structure to one of the possible structures. The atomic distances and lattice parameters of Cu_xCrSe_2 and the copper deficient part of $CuCr_2Se_4$ are too similar for a clear distinction.

STEM images reveal a double layered structure for $Cu_xCr_ySe_z$, supporting the assumption that the $Cu_xCr_ySe_z$ layer consists of either Cu_xCrSe_2 or copper deficient part of $CuCr_2Se_4$. EDX line scans and STEM gray values indicate that the $Cu_xCr_ySe_z$ layer consists of two Cr layers indicating the Cu_xCrSe_2. A less occupied chromium position in between the two chromium layers, which would correspond to the copper deficient part of $CuCr_2Se_4$, could not be ruled out. In some parts of the samples a secondary phase is observed. This might be another heterostructure or heterostructure C indicating that with the transformation into the different heterostructures a change in the layering along the c-axis occurs.

In future work EDX line scans with higher resolution will be performed in order to get a better understanding how the different heterostructures are formed and how

they transform into each other. Another objective of this EDX study will be the investigation of the secondary phase found in sample 3 and whether the secondary phase corresponds to one of the observed heterostructures or if it is a new, fifth heterostructure.

6. Structural investigation of the $Cu_xCr_ySe_z$ constituent

6.1. Introduction and aim

Transformation of crystal symmetry in bulk as well as in nanomaterials[129,130] has a major impact on the materials properties. Even subtle modifications of the structure such as strain,[131–134] change in site occupency[135–137] or lattice distortions[138–140] may have a major impact on electrical, catalytic, and magnetic properties. Therefore, a detailed analysis of the crystal structure of a material is essential for an explanation of its properties.

Slight variations in the site occupancies in SnV ferecrystals have a strong effect on the lattice parameters, the electric resistivity, and the Hall coefficient.[115] Similarly, the structure transformation from α to β-SnSe heavily affects the electric properties in associated ferecrystals.[109]

In the previous chapter, the formation of various heterostructures with varying annealing temperatures was presented. In the present chapter, different model layering schemes for the $Cu_xCr_ySe_z$ part of the structure are discussed and applied as starting models for Rietveld refinement.

6.2. Comparison of different models for the $Cu_xCr_ySe_z$ layer

The bulk $CuCr_2Se_4$ structure has two possible atomic arrangements along the [111] axis, that contain four selenium layers, a Cu deficient and a Cr deficient structure. It is also possible that the $Cu_xCr_ySe_z$ layer is made of $CuCrSe_2$. $CuCrSe_2$ has a layered structure of CdI_2-type $CrSe_2{}^{2-}$ layers that are stacked along the c-axis (Figure 6.1, left). Copper is tetrahedrally coordinated by Se^{2-} and fills 1/2 of the tetrahedra. The selenium forms a distorted octahedral coordination sphere around the Cr^{3+}.[123,141] It crystallizes in the trigonal space group *R3m* with an *a*-lattice parameter of 3.679(1) Å and a *c*-lattice parameter of 19.385(5) Å.[123]

For the model of $CuCrSe_2$ layers in the ferecrystals, a model where copper is in a symmetrically position between the $CrSe_2{}^{2-}$ layers has been used (Figure 6.1, right). The double layer structure has the composition $Cu_{0.5}CrSe_2$, *i.e.*, $CuCr_2Se_4$, but differs in its layering scheme from the $CuCr_2Se_4$ spinel. As the copper distances between the different $CrSe_2{}^{2-}$ layers are not equal in the bulk structure,[123] an asymmetrical

model was also considered.

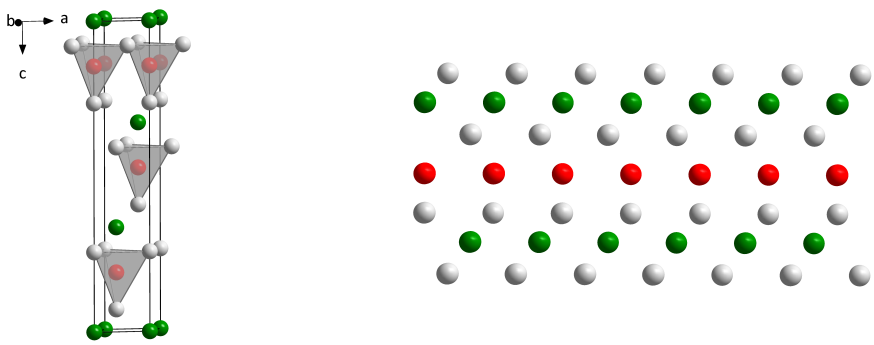

Figure 6.1: Crystal structure of $CuCrSe_2$[123] and assumed layering scheme for the ferecrystal with Cu in symmetrical position between the $CrSe_2{}^{2-}$ layers (Cu occupation might be lower).

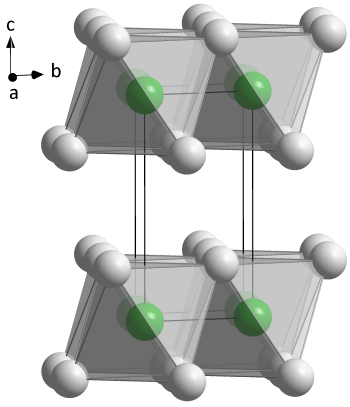

Figure 6.2: Crystal structure of $CrSe_2$.[142]

As we assume that copper might diffuse through the system, it is also possible that the $Cu_xCr_ySe_z$ layer is made of a $CrSe_2$ double layer with intercalated copper, *i.e.*, Cu_xCrSe_2. $CrSe_2$ crystallizes in the $Cd(OH)_2$ structure type with the space group $P\bar{3}m1$.[142,143] Chromium is octahedrally coordinated by selenium and forms $CrSe_2$ layers that are stacked along the c-axis.

All three structural models would result in a double layer structure as seen in the STEM image for set 3 (chapter 5, Figure 5.17). EDX line scan indicated that the $Cu_xCr_ySe_z$ layer consists of a Cu_xCrSe_2 double layer.

As EDX line scans revealed that copper diffused over the whole system and chromium is hard to refine next to copper in a Rietveld refinement based on X-ray data, it is challenging to make an unambiguous assignment of the atomic positions in $Cu_xCr_ySe_z$. Therefore, individual refinements according to the proposed structure models are carried out and discussed in comparison in the following.

Ferecrystalline materials usually exhibit Kiessig fringes due to interferences at the film/substrate and air/film interfaces along the $(00l)$ direction. These Kiessig fringes overlap with Bragg reflections and can not be modelled in a Rietveld refinement. Prior to the Rietveld refinement Le Bail fits were therefore performed to reduce the error and stabilize the refinement of reflection profiles. During the Le Bail fit, c-lattice parameter, zero shift, background and profile parameters are refined. These parameter are fixed in the Rietveld refinement, leaving only atomic site parameters to be refined. The Le Bail fit represents the best possible fit for the data and was compared to the Rietveld refinement results. X-ray diffraction in out-of-plane geometry gives for ferecrystals only information on the projection of the crystal structure along c, due to the orientation of the layers along the c-axis. This preferred orientation is simulated by setting the a and b-lattice parameters to very small values (0.5 Å) which shifts the h and k reflections to Q ranges larger than the simulated range. The in-plane diffraction patterns were handled similarly by setting the c-lattice parameter to 0.5 Å. During the Rietveld refinement the z coordinate, occupation, and isotropic vibrational parameter are refined. The vibrational parameter is kept equal for all atoms. The space group $P\bar{3}m1$ was used for the refinement. $P\bar{3}m1$ imposes a mirror plane in the center of the unit cell, which limits the number of atomic planes required to model the data.
The sample with two $NbSe_2$ layers prepared with the parameters of sample 3 annealed at 350 °C was taken to test the Rietveld refinement. This sample was easily fitted by a Le Bail fit and is therefore an ideal candidate to test different models. For all refinements, the same profile parameters, c-lattice parameters, background, and zero shift derived from the same Le Bail fit are used. The sample was modeled as a stack of two $NbSe_2$ layers and two $Cu_xCr_ySe_z$ layers. The layering in the $Cu_xCr_ySe_z$ layer was changed according to the Cu-deficient $CuCr_2Se_4$, Cr-deficient $CuCr_2Se_4$ and $CuCrSe_2$ structure. These three different types of layering were used as starting models for the Rietveld refinement. A propagation of copper over the whole unit cell was not considered in the models.

The Cu-deficient $CuCr_2Se_4$ model was used to refine the out-of-plane data. Figure 6.3 shows the measured and simulated patterns. For visualization of the low intensity reflections, the data is also plotted in log scale. The obtained occupation and atomic plane distances are illustrated in Figure 6.4. For the Cu-deficient $CuCr_2Se_4$ model, the (0.0.14) reflection appears to be extinct, whereas the reflection is clearly visible in the experimental data. Besides that the calculated pattern from the Rietveld refinement still gives a good simulation of the reflection intensities. Calculated occupations

for the Cr1 strongly deviate from those expected for Cu-deficient $CuCr_2Se_4$ (Figure 6.4 left). Moreover, the atomic distances in the $CuCr_2Se_4$ layer determined from the Rietveld refinement are completely different from the bulk material (Figure 6.4). This indicates that the Cu-deficient model is not appropriate to describe the data.

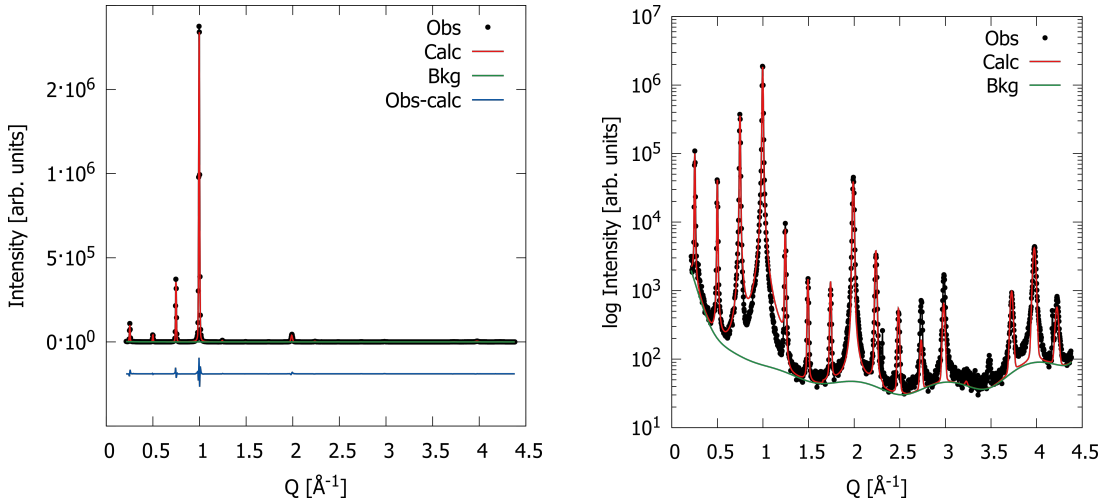

Figure 6.3: X-ray diffraction patterns of the 1:2 sample with the calculated background and difference between experimental and simulated pattern using the Cu-deficient model in linear (left) and log scale (right).

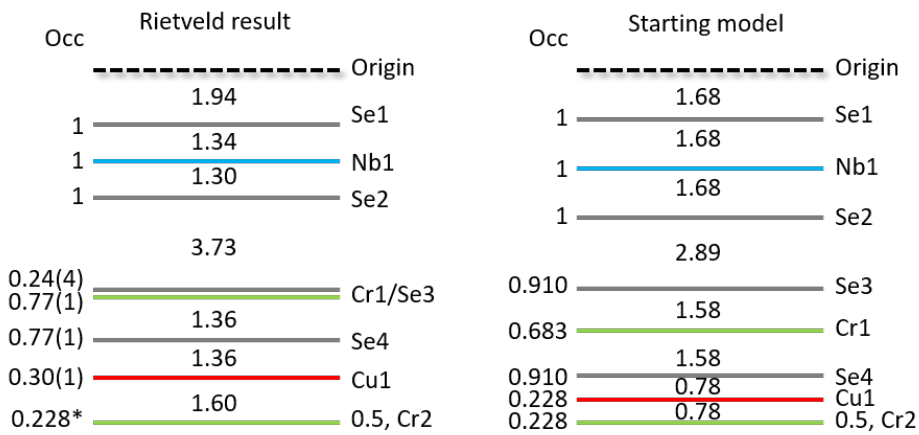

Figure 6.4: Comparison of atomic plane distances in Å along c-axis and site occupancies from the Rietveld refinement (left) and from the starting model derived from the bulk values for the Cu-deficient model (right).

Refinement results of the Cr-deficient model were used to refine the $(00l)$ data. The results of the Rietveld refinement are shown in Figure 6.5. Calculated atomic distances and site occupanies for the bulk model as well as the refined values are given in Figure 6.6. Rietveld refinement does not simulate the (0.0.11) reflection besides that the calculated pattern from the Rietveld refinement still gives a good simulation of the peak intensities. The copper and chromium occupations are double of the

expected values. The atomic distances for Cu1-Cr1 in the $Cu_xCr_ySe_z$ layer are much smaller than in the bulk material. The z-coordinates and site occupancies appeared to be heavily correlated indicated by unstable fits. Therefore, these parameters were excluded from the last step of the refinement. This underlines that the Cr-deficient $CuCr_2Se_4$ is not an appropriate model to describe the sample.

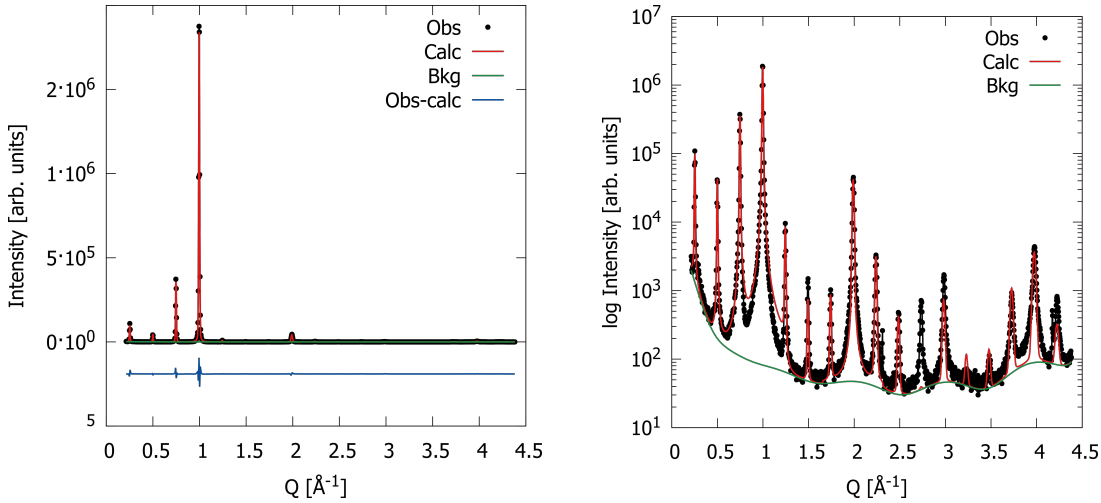

Figure 6.5: X-ray diffraction patterns of the 1:2 sample with the calculated background and difference between experimental and simulated pattern using the Cr-deficient model in linear (left) and log scale (right).

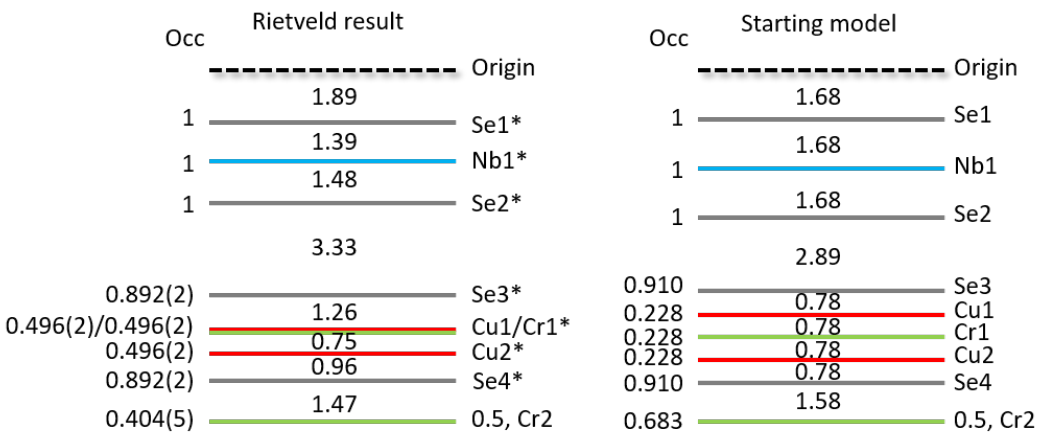

Figure 6.6: Comparison of atomic plane distances in Å along c-axis and site occupancies from the Rietveld refinement (left) and from the starting model derived from the bulk values for the Cr-deficient model (right). * not refined in last refinement step.

The Rietveld refinement using the $CuCrSe_2$ model gives a match of the simulated and observed reflections as shown in Figure 6.7. Moreover, atomic distances along the c-axis obtained from the Rietveld refinement are in good agreement with the model (Figure 6.8). For example the Se1-Cu1 distance is close to the bulk distances

1.67 and 1.74 Å calculated and bulk values, respectively. The copper occupation is lower than the expected value for $CuCrSe_2$. The atomic distances derived from the Rietveld refinement are according to the atomic distances determined from the gray value plot of the STEM image (5.19).
Besides the copper occupation all the other parameters are in agreement with the bulk material. The fit profile matches the intensity profile of the data, which indicates that $CuCrSe_2$ is the best model to describe the data.

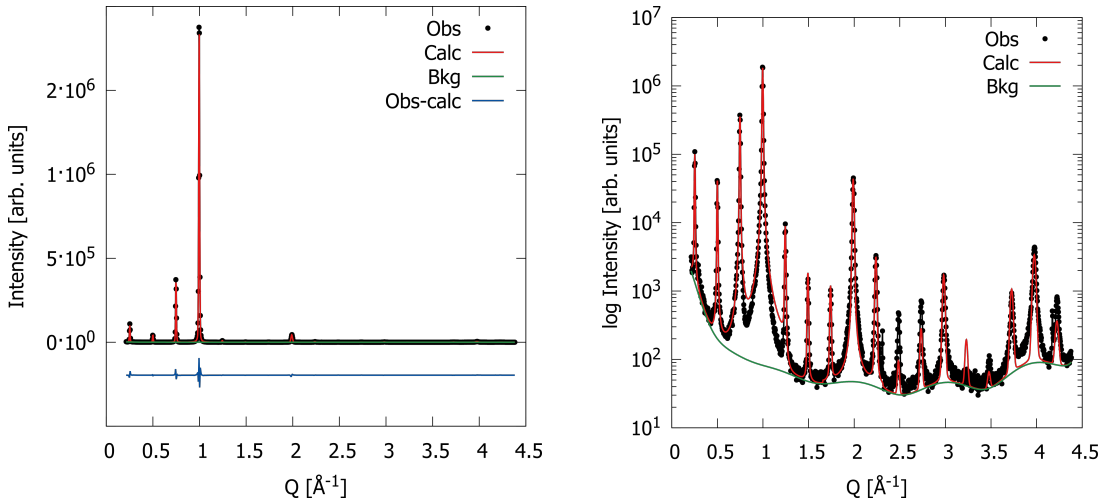

Figure 6.7: X-ray diffraction patterns of the 1:2 sample with the calculated background and difference between experimental and simulated pattern using the $CuCrSe_2$ model in linear (left) and log scale (right).

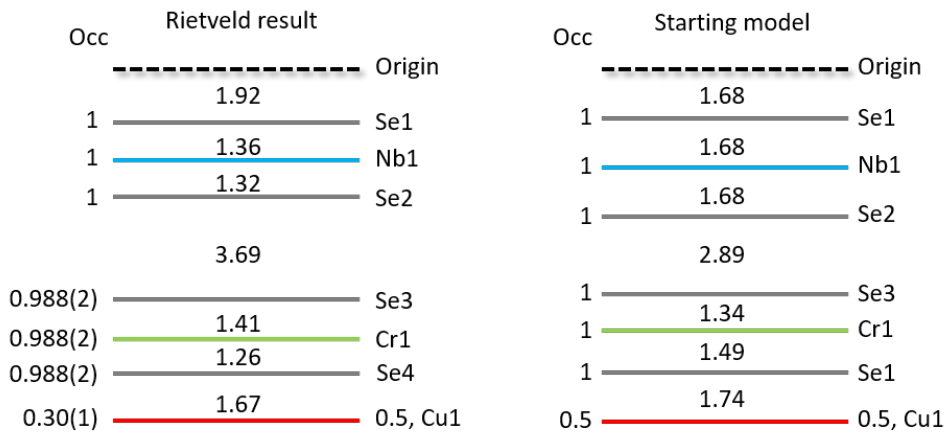

Figure 6.8: Comparison of atomic plane distances in Å along c-axis and site occupancies from the Rietveld refinement (left) and from the starting model derived from the bulk values for the $CuCrSe_2$ model (right).

The bulk structure of $CuCrSe_2$ has a layered structure of $CrSe_2^{2-}$ layers with copper (Cu1) filling tetrahedral sites. For the previous refinement, a model where copper is in symmetrically located between the $CrSe_2$ layers has been used. As in the bulk

structure copper is not in a symmetrical position between the $CrSe_2$ layers, an asymmetrical model has to be considered.

The results of the symmetrical $CuCrSe_2$ have been used as starting parameters and the Cu z-coordinate starting value was set to 0.45. A refinement of all z-coordinates simultaneously was not possible as the fit diverges. Apparently, the site occupancies and remaining z-coordinates are not significantly affected by the change in copper position. As the variation of the copper position has no major effect on the refined parameters, the symmetric $CuCrSe_2$ seems to be an appropriate model to describe the $(Cu_xCr_ySe_z)_{1+\delta}(NbSe_2)_2$ sample annealed at 350 °C.

The R-values of the four different refinements in Table 6.1 are for all models in the same range for all models and do not allow to differentiate a better fit.

Table 6.1: R-values of the Rietveld refinements.

	wRp	Rp
Cu-deficient	0.1451	0.0814
Cr-deficient	0.1461	0.0816
$CuCrSe_2$ sym	0.1453	0.0822
$CuCrSe_2$ asym	0.1457	0.0822

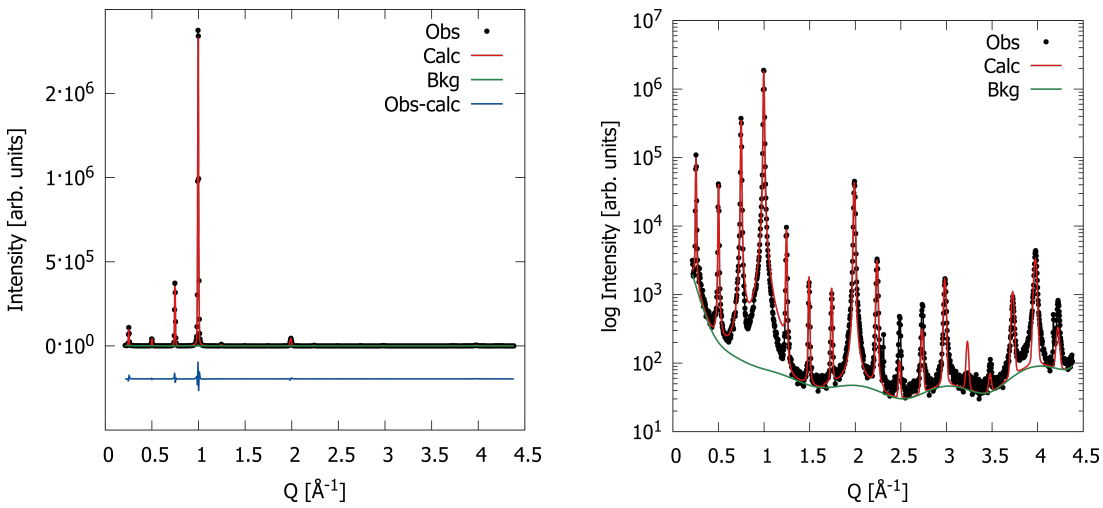

Figure 6.9: X-ray diffraction patterns of the 1:2 sample with the calculated background and difference between experimental and simulated pattern using the asymmetric $CuCrSe_2$ model in linear (left) and log scale (right).

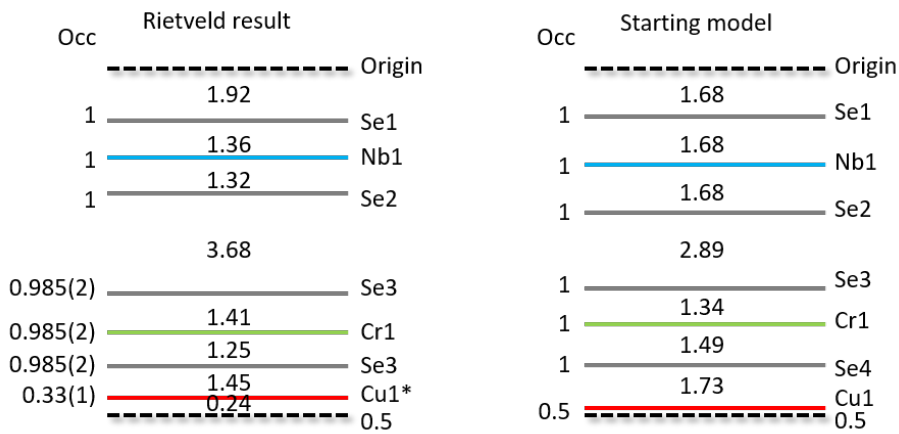

Figure 6.10: Comparison of atomic plane distances in Å along c-axis and site occupancies from the Rietveld refinement (left) and from the starting model derived from the bulk values for the asymmetric $CuCrSe_2$ model (right). * not refined in last refinement step.

6.3. Structural differences in heterostructure A and B

The Rietveld refinement of the 1:2 sample annealed at 350 °C indicated that Cu_xCrSe_2 is the best starting model of the tested models to refine the out-of-plane data. Therefore this model was used to refine the out-of-plane data of the 1:3 sample of set 3 annealed at 350 °C (sample 3 A) and 400 °C (sample 3 B).

Figure 6.11 gives the Rietveld refinement of sample 3 annealed at 350 °C. All reflections besides the (0.0.22) are simulated by the Rietveld refinement, indicating that the $CuCrSe_2$ model is a suitable model to describe heterostructure A of sample 3. During the Rietveld refinement it was not possible to refine the copper occupation. As the 1:3 sample contains an additional $NbSe_2$ layer, the model became more complex and therefore less stable than the refinement of the 1:2 sample. Sample 3 is also very smooth and has Kiessig Fringes to high Q which increases the background. Sample 3 A contains reflections of heterostructure A and C, which makes the simulation of the peak profile more challenging.

The Rietveld refinement of sample 3 B is given in Figure 6.12, showing that besides the (0.0.12) and (0.0.22) all reflections are simulated. Same as for sample 3 A it was not possible to refine the copper occupation. The refined atomic distances for the $CuCrSe_4$ layer agree well with the atomic distances from the $CuCrSe_2$ model indicating that the model is suitable to describe the heterostructures A and B of sample 3. The atomic Se1-Se2 distance in $NbSe_2$ depicted in Figure 6.13 (left) is larger than in bulk $NbSe_2$ (6.13 right), indicating an intercalation of copper between the layers. The Se1-Se2 distance decreases from sample 3 A (6.13 middle) to sample 3 B, indicating that

the amount of intercalated copper is reduced. Sample 3 B was annealed to a higher temperature and therefore contains less selenium. A more uniform propagation of copper is also possible.

This indicates that in heterostructures A and B, the $Cu_xCr_ySe_z$ layer is a Cu_xCrSe_2 with a lower copper occupation than in the bulk compound. The different heterostructures might vary in their copper intercalation in the van der Waals gaps and consequential in their atomic distances.

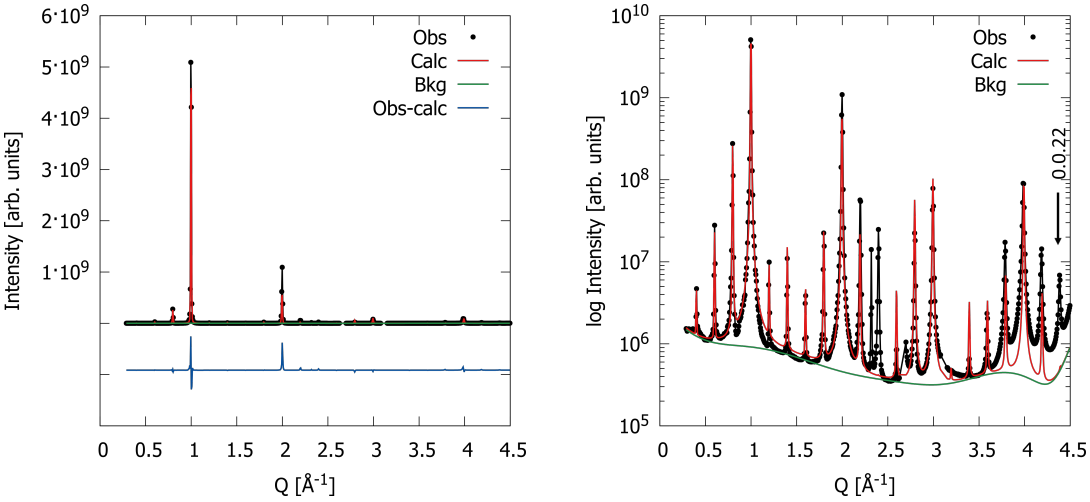

Figure 6.11: X-ray diffraction patterns of sample 3 A with the calculated background and difference between experimental and simulated pattern using the $CuCrSe_2$ model in linear (left) and log scale (right).

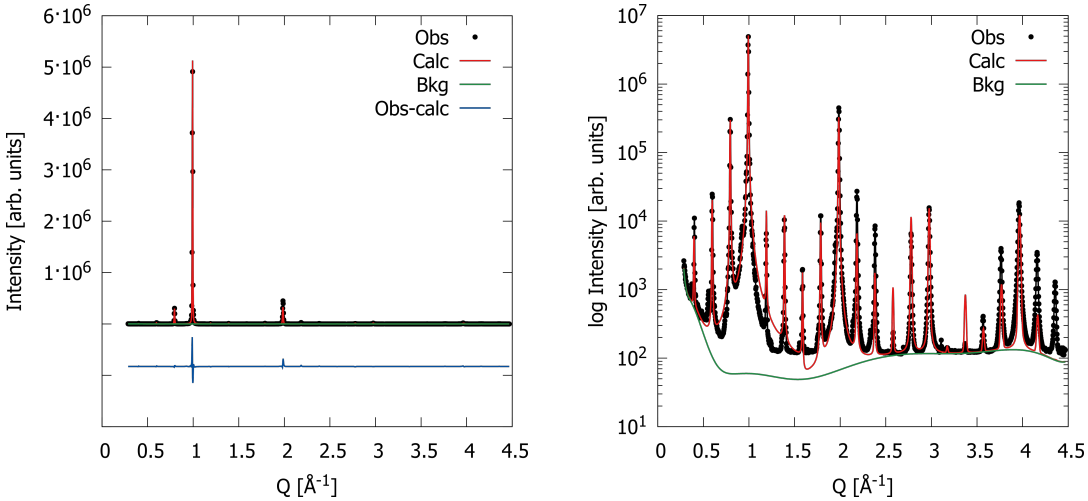

Figure 6.12: X-ray diffraction patterns of sample 3 B with the calculated background and difference between experimental and simulated pattern using the $CuCrSe_2$ model in linear (left) and log scale (right).

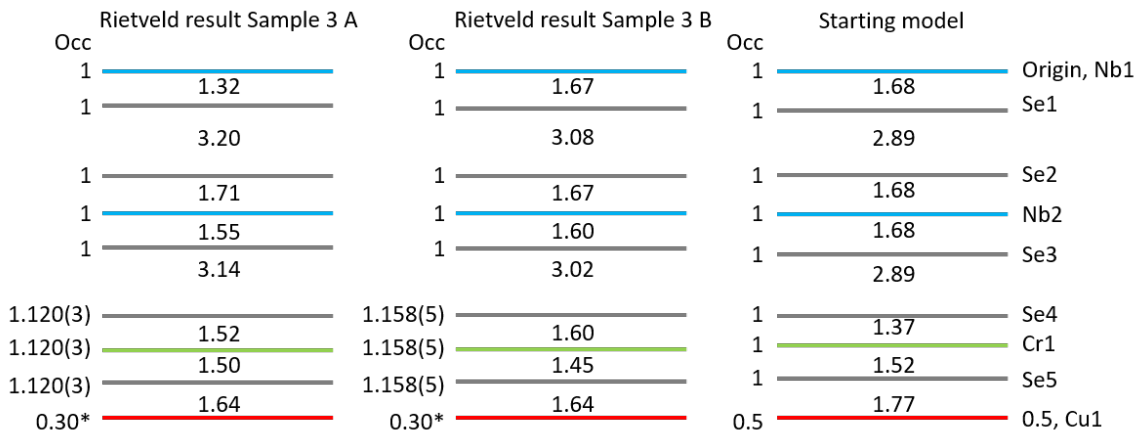

Figure 6.13: Atomic plane distances in Å along c-axis and occupation from the Rietveld refinement using the symmetric $CuCrSe_2$ model for sample 3 A (left), sample 3 B (middle), and the bulk values for symmetric $CuCrSe_2$ model (right). * not refined in last refinement step.

6.4. Preparation of $[(Cu_xCr_ySe_z)_{0.5}]_{1+\delta}(NbSe_2)_3$

The atomic distances derived from STEM gray values, EDX line scan and Rietveld refinement of the 1:2 and 1:3 sample, indicate that the $Cu_xCr_ySe_z$ double layer has four selenium layers.

A sample with only one copper layer would reduce the amount of parameters to be refined. Therefore, it was tried to prepare a sample with only one $Cu_xCr_ySe_z$ layer. It was aimed for a $[(Cu_xCr_ySe_z)_{0.5}]_{1+\delta}(NbSe_2)_3$ sample (sample 6) as samples with three $NbSe_2$ were easier prepared with a suitable crystallinity in previous experiments.

For the sample preparation, the same layering scheme as for the 1:3 samples has been used to prevent the formation of $CuSe_2$. The deposition parameters for the $Cu_xCr_ySe_z$ layer were reduced by 1/2 resulting in the deposition parameters in Table 6.2. The deposition parameters are based on the parameters of sample 4.

Table 6.2: Parameters for preparation of the $[(Cu_xCr_ySe_z)_{0.5}]_{1+\delta}(NbSe_2)_3$ sample 6

	sample 6		
	Få	Rate	Tooling Factor
Nb	7.7	0.2	64
Se	8.3	0.5	65
Se	3.7	0.5	65
Cr	2.6	0.2	64
Cu	2.1	0.2	64
Cr	2.6	0.2	64
Se	3.7	0.5	65

6.5. Structure of $[(Cu_xCr_ySe_z)_{0.5}]_{1+\delta}(NbSe_2)_3$

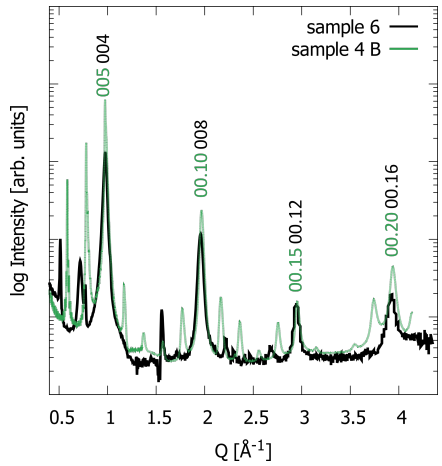

Figure 6.14: X-ray diffraction patterns of sample 6 (black line) and sample 4 (green line) annealed at 400 °C in the range of 0.4 - 4.5 Å.

In comparison to sample 4, sample 6 has a lower crystallinity as reflections for example the reflections (005) - (007), are extinct. All reflections can be indexed as $(00l)$ reflections indicating that even though the sample has a poor crystallinity, it is aligned along the c-axis. This indicates that a double layer structure of Cu_xCrSe_2 is essential for a good crystallinity of the $[(Cu_xCrSe_2)_{1+\delta}]_1(NbSe_2)_n$ ferecrystals.
For the Rietveld refinement of sample 6, a variation of the $CuCrSe_2$ model with Cr in the 0.5 position was used (Figure 6.15, right). The atomic distances derived from the Rietveld refinement in the $NbSe_2$ layers and the Cu_xCrSe_2 are much lower than the expected bulk values (Figure 6.15, left). This indicates that the Cu_xCrSe_2 model is not appropriate to describe the single $Cu_xCr_ySe_z$ layer.
The c-lattice parameter of sample 6 is 25.48(3) Å which corresponds to the c-lattice parameter of sample 4 reduced by 1/2 of the $Cu_xCr_ySe_z$ double layer thickness. This

indicates that even though the structure of sample 6 seems to be different, the total thickness of the $Cu_xCr_ySe_z$ single layer is similar to the $Cu_xCr_ySe_z$ layer in sample 4. This is not surprising since all discussed compounds for the $Cu_xCr_ySe_z$ double layer have similar c-lattice parameters.

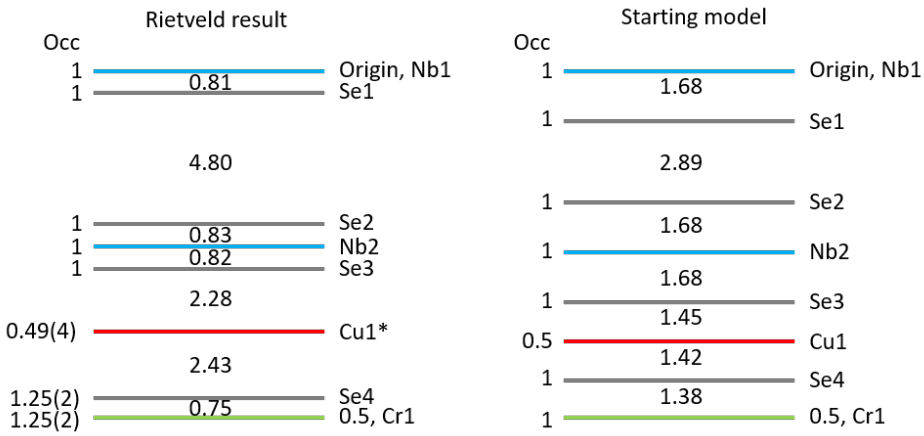

Figure 6.15: Comparison of atomic plane distances in Å along c-axis and site occupancies from the Rietveld refinement for sample 6 (left) and from the starting model derived from the bulk values for the $CuCrSe_2$ model (right).

Figure 6.16 gives the in-plane diffraction patterns of sample 4 and 6. Due to the lower content of $Cu_xCr_ySe_z$, the reflections of $NbSe_2$ have a higher intensity in sample 6. As a result, the $(220)_{Cu_xCr_ySe_z}$ and $(520)_{Cu_xCr_ySe_z}$ reflections appear in sample 6 only as shoulder of the $NbSe_2$ reflections. Therefore, the determination of the a-lattice parameter is more challenging and the a-lattice parameters of $Cu_xCr_ySe_z$ in sample 6 might be underestimated. No reflections of a secondary phase can be seen in sample 6.

By reducing the $Cu_xCr_ySe_z$ party to a single layer, the a-lattice parameter of $NbSe_2$ was not affected (Table 6.3). The a-lattice parameters of the $Cu_xCr_ySe_z$ layer in sample 6 (7.21(1) Å) is reduced by 0.1 Å in comparison to sample 4 (7.30(1) Å), which might be due to a change in structure.

Table 6.3: Calculated a-lattice parameters and misfit parameter of the samples 4 B and 6 and their corresponding heterostructures.

	$Cu_xCr_ySe_z$ a [Å]	$NbSe_2$ a [Å]	misfit δ
Sample 4 B	7.30(1)	3.501(9)	0.460
Sample 6	7.21(1)	3.515(3)	0.475

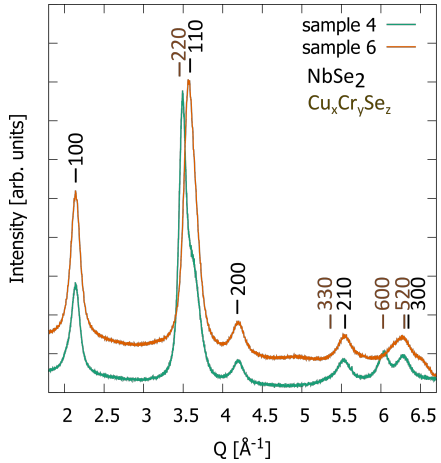

Figure 6.16: In-plane diffraction patterns of sample 4 and 6.

6.6. Summary

Diffraction and electron microscopy data discussed in the previous chapter 5 indicated a Cu_xCrSe_2 structure. A variation of the $CuCr_2Se_4$ structure could not be excluded. A $(Cu_xCr_ySe_z)_{1+\delta}(NbSe_2)_n$ compound with $n = 2$ was prepared and Rietveld refinement of the out-of plane diffraction pattern was performed to determine the structure of the $Cu_xCr_ySe_z$ layer. Four structure models for the $Cu_xCr_ySe_z$ layer were tested. A symmetric variation of the $CuCrSe_2$ structure gave the best fit for the data of the 1:2 data set.

In order to gain more detailed information on the different heterostructures in the 1:3 samples, the Cu_xCrSe_2 model was used to refine samples with three $NbSe_2$ layers annealed to 350 and 400 °C. A refinement with all parameters was not possible but an adequate description of the atomic distances was achieved. The refined Se-Se distances in the $NbSe_2$ and between $NbSe_2$ and Cu_xCrSe_2 are considerably larger in the sample annealed to 350 °C (heterostructure A) than in the sample annealed to 400 °C (heterostructure B). This indicates that the structural difference in the heterostructures is based on the copper intercalation in the van der Waals gaps.

Rietveld refinement on samples with only one $Cu_xCr_ySe_z$ layer did not give a sufficient fit indicating that the Cu_xCrSe_2 model is not appropriate to describe the data. The sample with a $Cu_xCr_ySe_z$ single layer had a poorer crystalinity underlining that the $Cu_xCr_ySe_z$ double layer is essential for a decent crystallinity.

The Rietveld refinement data indicates that the $Cu_xCr_ySe_z$ double layer in $(Cu_xCr_ySe_z)_{1+\delta}(NbSe_2)_n$ has the structure of Cu_xCrSe_2. For further investigation, EDX line scans focusing on the copper intercalation would allow an assignment of copper occupations and verify if the structural changes in the heterostructures are based on the copper intercalation in the van der Waals gaps.

7. $[(Cu_xCr_ySe_z)_{1+\delta}]_1[NbSe_2]_n$ ferecrystals

7.1. Introduction and aims

In the previous chapter 5, the influence of the annealing condition and the copper chromium ratio on the formation of different heterostructures in $[(Cu_xCr_ySe_z)_{1+\delta}]_1(NbSe_2)_3$ ferecrystals was discussed. Previous work showed that increasing the amount of TSe_2 dimensionality n systemically changes structure,[79] resistivity,[104,128,144] charge density wave transition temperature,[104] transport properties,[145] and superconducting transition temperature.[128] The amount of $NbSe_2$ reception units per superstructure n might therefore affect the heterostructure formation.
The magnetic properties such as interlayer coupling of multilayered materials can be modified by systematic variation of the non magnetic spacer thickness.[146] Clake and Freedman[147] showed that the interlayer (ferromagnetic) and intralayer (antiferromagnetic) coupling for $(BiSe)_{1.23}(CrS_2)_n$ misfit materials can be altered by introducing a BiSe spacer.
Changing the separation layer thickness n in range of n = 1 - 5 may alter the phase composition in case of significant copper diffusion as well as the structure and magnetic properties. To investigate the correlation of structural and magnetic interface effects in magnetic ferecrystals with n series, $[(Cu_xCr_ySe_z)_{1+\delta}]_1(NbSe_2)_n$ ferecrystals were prepared.

7.2. Sample preparation

The deposition parameters, which were obtained through the calibration process described in chapter 5.2, enabled the preparation of smooth samples with a high crystallinity. The deposition parameters of sample 3 (Table 5.1) were used to obtain a set of samples with n = 1 - 5 layers, referred to as set 3 in the following discussion. The amount of Nb|Se repetitions deposited in between the Se|Cr|Cu|Cr|Se is equal to n. The samples of set 3 were annealed to 350 °C and 400 °C aiming for heterostructure A and B.

7.3. Structural investigation of set 3 with n = 1 - 5

Reflectivity scans of set 3 annealed at 400 °C show uniform Kiessig fringes up to high Q (Figure 7.1 left) which indicates that the material is a smooth multilayered ma-

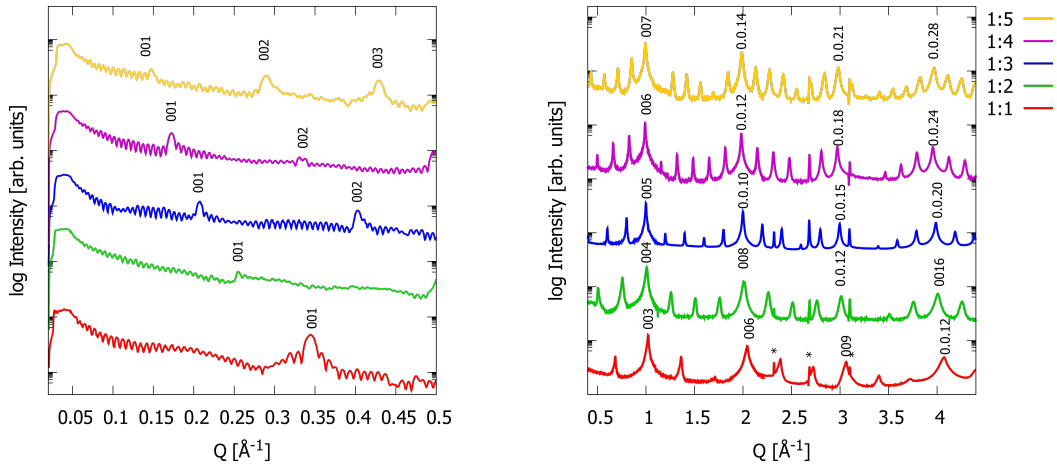

Figure 7.1: Specular diffraction patterns of set 3 annealed at 400 °C in the range of 0 - 0.5 Å^{-1} and 0.4 - 4.5 Å^{-1}. * = sample holder

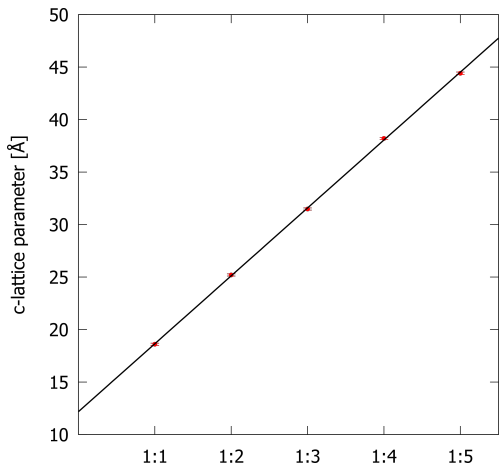

Figure 7.2: Representation of the change in c-lattice parameter as a function of the number of $NbSe_2$ layers n.

terial. The superstructure is crystalline along the staking direction, and all Bragg reflections can be indexed as $(00l)$ of the superlattice (Figure 7.1 right). The linear trend in the function of c-lattice parameter and amount of $NbSe_2$ layers, n, (Figure 7.2) enables to calculate the single layer thickness of the $NbSe_2$ and $Cu_xCr_ySe_z$ layer, respectively. The slope of the measured multilayer thickness corresponds to the single layer thickness of the $NbSe_2$ along c and has a dimension of 6.47(4) Å, which is larger than found in bulk material (6.291 Å).[124] The increased thickness might result from the copper intercalation in the $NbSe_2$ layer. The EDX data of $[(Cu_xCr_ySe_z)_{1+\delta}]_1[NbSe_2]_3$ annealed at 400 °C also indicates a copper intercalation into the $NbSe_2$ layer (chapter 5.6). In $Cu_{0.06}NbSe_2$ the c-lattice parameter is not affected by the copper intercalation.[148] The change in c-lattice in the $NbSe_2$ might hence result from a larger amount of copper intercalation.

The y-axis intercept (Figure 7.2) corresponds to the $Cu_xCr_ySe_z$ layer thickness along

c and has a value of 12.2(1) Å, which is slightly smaller than found in bulk $CuCr_2Se_4$ (12.66 Å)[56] or $CuCrSe_2$ (12.93 Å).[149] This might be due to a loss of copper into the $NbSe_2$ layer. Scince the c-lattice parameter as a function of n has linear trend, the copper intercalation has to be systematically with n. A table with the c-lattice parameters of set 3 can be found in the appendix D.1.

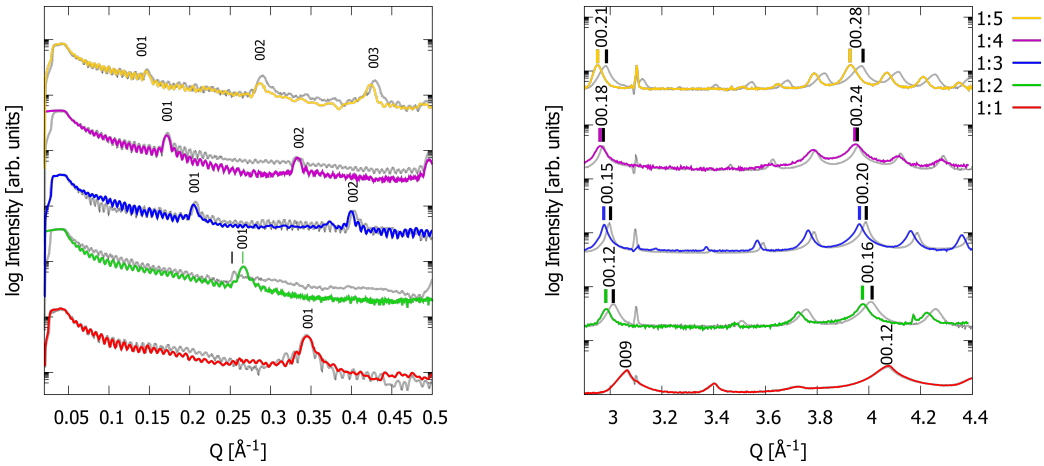

Figure 7.3: Specular diffraction patterns of set 3 annealed at 350 °C in the range of 0 - 0.5 Å^{-1} and 2.9 - 4.5 Å^{-1}. The sample annealed at 400 ° is pictured below in black. * = sample holder

Figure 7.3 gives the specular diffraction patterns of set 3 annealed at 350 °C (colour) and 400 °C (gray). The samples of set 3 annealed at 400 °C have a slight shift of the reflection position to higher Q. This effect is observed at low Q ranges (Figure 7.3 left) and more distinct in high Q ranges (Figure 7.3 right). Surprisingly, the shift to higher Q values in the 1:4 sample is much smaller than for the other samples and the c-lattice parameter of the 1:1 samples is the same after annealing at 350 and 400 °C. Possibly the transition temperature from heterostructure A to B is not the same for all samples of set 3. It is also possible that the different heterostructures can not be formed in all samples of set 3. Another explanation would be that the heterostructures A and B have only a small shift or no shift in the c-lattice parameter for the $n = 1, 4$. Moreover, it is not clear which part of the layer is responsible for the heterostructure transformation. An effect of the $NbSe_2$ layer thickness n on the transformation can not be excluded.

Besides the different c-lattice parameters, the samples annealed at different temperatures have a slightly different intensity profile. This change in the intensity profile can be observed in the XRD pattern of the 1:4 sample (Figure 7.4 (left)). The different intensity profiles could be explained by a transition from heterostructure A to B even though the shift in c-lattice parameter is rather low.

Distinct reflections of a heterostructure B can only appear for sample 1:3 (Figure 7.4). A detailed discussion on the different heterostructures in the 1:3 samples can be found in chapter 5.4. The separate diffraction pattern of the 1:1 sample has unsymmetrical Bragg reflections indicating the overlap with a second phase.[150] The limitations of reproducibility in the sample series might be the reason that the other compounds in series 3 have no distinct reflections of heterostructure B. Another reason might be that the structure of the 1:3 sample in series 3 facilitates the formation of heterostructure B at lower temperatures.

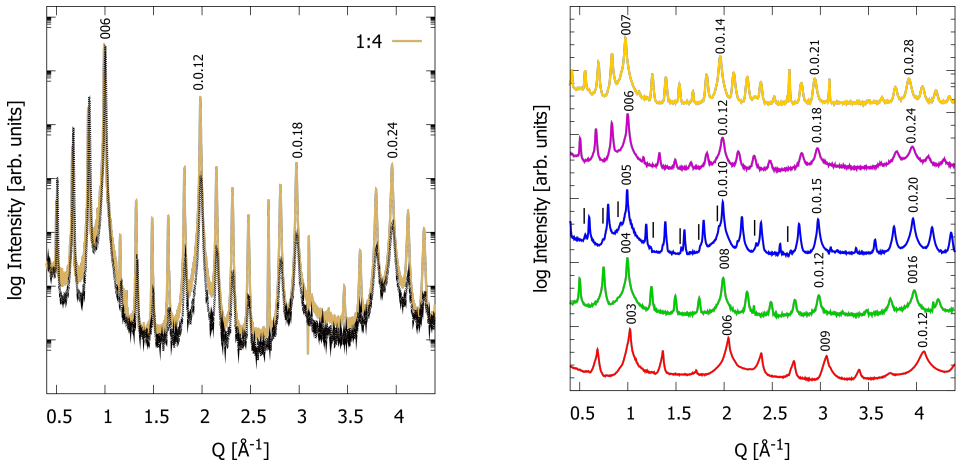

Figure 7.4: Specular diffraction patterns of the 1:4 sample of set 3 annealed at 350 °C in the range of 0.4 - 4.5 Å^{-1} (right). The 1:4 sample of set 3 annealed at 400 °C is pictured below in black. Specular diffraction patterns of the $[(Cu_xCr_ySe_z)_{1+\delta}]_1(NbSe_2)_4$ sample annealed at 350 °C in the range of 0.4 - 4.5 Å^{-1} (left).

7.4. Magnetic Properties of $CuCr_2Se_4$, $CuCrSe_2$, and $CrSe_2$

Bulk $CuCr_2Se_4$ is metallic conducting and has a Curie temperature T_C above room temperature. T_C is affected by impurities[151–153] and deviations from the perfect spinel composition.[154] Therefore, a rather broad range of Curie temperatures of 415 - 460 K[155–158] has been stated. Zhang *et al.* investigated the T_C by various techniques and obtained a T_C value of 430 K.[159] The magnetic easy axis in $CuCr_2Se_4$ is along [111].[156] This affects the in-plane and out-of-plane field dependent magnetization in crystallographically aligned films.[58] Besides structural and compositional variations, the T_C is also affected by the crystallite size.[160] Wang *et al.* investigated that a decreasing particle size decreases the saturation magnetisation, the Curie constant, T_C, and the effective magnetic moment per Cr (values for the bulk material are given in Table 7.1).[160,161] Nanocrystalline $CuCr_2Se_4$ is only ferromagnetic below

its blocking temperature, which is also size dependent.[159,161,162] Two contradicting models for the electronic and magnetic states in $CuCr_2Se_4$ have been discussed in literature and will be summarized in the following.

Lotgering and van Stapele proposed the electronic configuration $Cu^+(Cr^{3+}Cr^{4+})Se_4^{2-}$.[155] Indirect coupling of the Cr^{3+} and Cr^{4+} ion spins via holes in the valence band explains the ferromagnetism. They propose that $CuCr_2Se_4$ conducts due to hole conduction, while e^- are transferred from Se_4^{2-} p-states to Cr^{4+} d-states.

Goodenough proposed a contradicting model with the suggested electronic configuration $Cu^{2+}(Cr^{3+})_2Se_4^{2-}$.[163] The overall ferrimagnetism is caused by nearest neighbour superexchange interactions, a ferromagnetic 90 ° cation-anion-cation interaction, and an antiferromagnetic cation-cation interaction (direct exchange and superexchange are shown in Figure 7.5). Neutron diffraction[157,164] and nuclear magnetic resonance (NMR)[165] experiments indicate a Cr^{3+} valence state.

Kimura *et al.*[166] performed soft X-ray magnetic circular dichroism spectroscopy (XMCD) to characterize the electronic and magnetic states and showed that the valence state of Cr is 3^+. They proposed a modified version of Goodenoughs model. The electronic structure is $Cu^+(Cr^{3+})_2\square^{+1}Se_4^{2-}$. The holes induced into the Se 4p-states are necessary for the charge balance. Various band structure calculations[57,167] and XMCD measurements[168] support Kimuras model.

Saha-Dasgupta *et al.* performed multiple density of states (DOS) calculations revealing that the ferrimagnetism in $CuCr_2Se_4$ is stabilized if the angle Cr-Se-Cr gets close to 90 ° (in $CuCr_2Se_4$ the angle Cr-Se-Cr is 93.48 °).[169] They propose a kinetic energy driven mechanism. The Cr ions and the delocalized Se 4p band hybridization lead to a hole-mediated exchange. Their proposed electronic structure is $Cu^+Cr^{3+}_{\uparrow}Se^-_{\downarrow}Cr^{3+}_{\uparrow}Se_3^{2-}$. The metallicity is explained by the charge of the hole. This results are supported by modified Arrott plot, Kouvel–Fisher method,[159] and band structure calculations.[170]

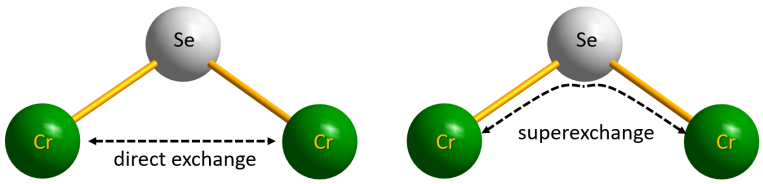

Figure 7.5: Schematic illustration of direct exchange and superexchange.

In contrast to $CuCr_2Se_4$, $CuCrSe_2$ is an antiferromagnetic compound and a p-type

Table 7.1: Bulk values for the Curie constant C, effective magnetic μ_{eff} moment per Cr, Curie-Weiss Temperature Θ_W, Curie Temperature T_C, Néel temperature T_N, and second Néel temperature T_{N2} for $CuCr_2Se_4$, $CuCrSe_2$, and $CrSe_2$.

	$CuCr_2Se_4$	$CuCrSe_2$ ordered	$CuCrSe_2$ disordered	$CrSe_2$
C [K]	2.55[156]	2.37[171]	1.64[172]	
μ_{eff} Cr [μ_B]	5.0[156,166]	2.9[173]	3.62[172]	2.44[174]
Θ_W [K]		5[173]	31.82[172]	
T_C [K]	430[159]			
T_N [K]		55[173]	55[172]	157[175]
T_{N2} [K]				20[175]

conductor with a metal-like conductivity.[176] The electronic configuration is $Cu^+Cr^{3+}Se^{2-}$.[177] The indirect 90° Cr-Se-Se exchange is similar to $CuCr_2Se_4$ and ferromagnetic. The direct exchange between Cr-Cr is antiferromagnetic and depends on the Cr-Cr distance,[149,171] while the magnetic easy axis is perpendicular to the c-axis as the direct exchange in $CuCrSe_2$ is stronger then the indirect interaction.[178]

$CrSe_2$ has a short Cr-Cr distance of 3.399 Å[142] and is therefore a strong antiferromagnet. Its magnetic easy axis is perpendicular to the c-axis as the Cr-Cr is shorter along the a- and b-axis. The electronic configuration is $Cr^{4+}Se^{2-}$.[174] $CrSe_2$ monolayers can be switched from antiferromagnetic to ferromagnetic by strain induction.[179]

7.5. Macroscopic magnetization

Temperature dependent zero field (ZFC) and field cooled (FC) susceptibility χ curves have been measured for the 1:1, 1:2, 1:3, and 1:5 sample of set 3. χ was corrected for a diamagnetic contribution χ_D and a linear term χ_T. The linear term was derived phenomenologically and might be related to substrate impurities as the substrates were not necessarily pure silicon.
The corrected susceptibility χ_{corr} was calculated with a modified Curie-Weiss-law:

$$\chi_{\text{exp}} = \frac{C}{T-\theta} + \chi_T T + \chi_D \tag{7.1}$$

$$\chi_{\text{corr}} = \chi_{\text{exp}} - \chi_T - \chi_D \tag{7.2}$$

Here M is the volume magnetization, H the applied magnetic field, T the temperature, C the Curie constant, and θ the Curie-Weiss temperature.

Figure 7.6 (left) shows χ before the correction with χ_D and χ_T. The modified Curie-Weiss-law has been fitted to χ (black line). Figure 7.6 (right) shows the corrected χ_{corr} as a function of temperature.

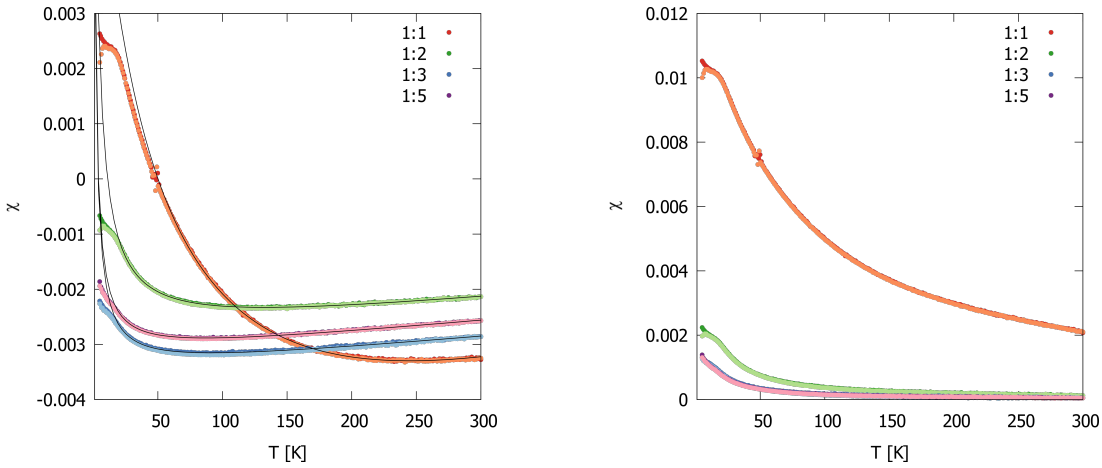

Figure 7.6: Temperature dependent susceptibility curves for the 1:1, 1:2, 1:3, and 1:5 samples of set 3 annealed at 400 °C (left). Corrected susceptibility as a function of the temperature (right). Samples were measured in FC and ZFC (pale colours) at 0.25 T.

The FC curves for the 1:1 sample exhibit a distinct splitting to the ZFC curve (Figure 7.4) giving strong evidence that there is a low temperature cooperative magnetism in this sample. This splitting is also present in the 1:2 sample but less pronounced. In the 1:3 and 1:5 samples, no splitting between the ZFC and FC curve is observed, which indicates that above a separation layer thickness of $n = 2$ no or a non detectable interlayer coupling occurs.

The χ_{corr} has been used to plot the inverse susceptibility χ^{-1}, which is represented in Figure 7.7. χ^{-1} has been used to fit C, and θ. Table 7.2 gives the calculated values for χ_D, χ_T, C, and θ. The corrected values for χ_D and χ_T are similar for the 1:2, 1:3, and 1:5 sample and have a larger deviation for the 1:1 sample. It might be that another type of silicon wafer has been used for the 1:1 sample which would lead to a different background. C increases with decreasing n, underlining the effect of n on the interlayer coupling (Table 7.2). θ is -48 K for the 1:1 sample indicating an antiferromagnetic coupling which would be expected for $CuCrSe_2$. With increasing n increases θ underlining a reduction of the magnetic coupling. All values for C and θ are below the bulk values of $CuCrSe_2$ (Table 7.1).

The effective magnetic moment μ_{eff} per Cr was calculated by a notional lattice with the in-plane lattice parameters of $NbSe_2$ and the c-lattice parameter of the supercell. By knowing that the amount of niobium atoms per supercell is z(Nb) = η, the z(Cr)

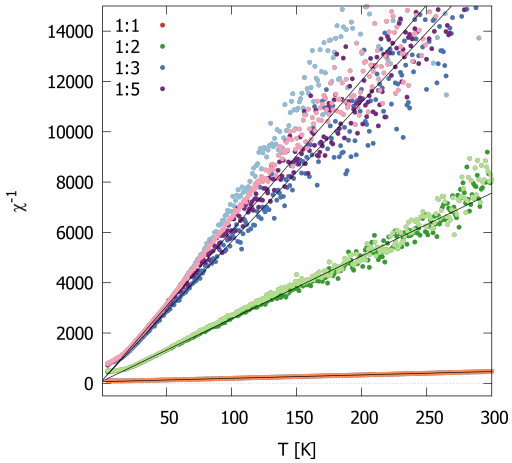

Figure 7.7: Temperature dependent inverse susceptibility curves for the 1:1, 1:2, 1:3, and 1:5 samples of set 3 annealed at 400 °C. Samples were measured in FC and ZFC (paler colours) at 0.25 T.

Table 7.2: Correction parameters for the diamagnetic susceptibility χ_D and linear susceptibility χ_T as well as Curie constant C and Curie-Weiss temperature θ for each sample.

	1:1	1:2	1:3	1:5
χ_T [K^{-1}]	8.6(2)·10^{-6}	2.19(2)·10^{-6}	2.10(2)·10^{-6}	2.15(2)·10^{-6}
χ_D [K^{-1}]	-7.9(1)·10^{-3}	-2.914(7)·10^{-3}	-3.5394(6)·10^{-3}	-3.260(5)·10^{-3}
C [K]	0.74(2)	0.0400(6)	0.0180(5)	0.0167(4)
θ [K]	-48(2)	-2.8(3)	-1.4(5)	1.1(5)

can be calculated from the Cr/Nb ratio derived from XRF. Dividing z(Cr) by the volume of the notional lattice V_η η(Cr) can be derived. μ_{eff} is thus given by:

$$\frac{\mathrm{z(Cr)}}{\mathrm{V}_\eta} = \eta(\mathrm{Cr}) \tag{7.3}$$

$$\mu_{eff}[J/T] = \sqrt{\frac{3 \cdot C \mathrm{k_B}}{\mu_0 \eta(\mathrm{Cr})}} \tag{7.4}$$

$$\mu_{eff}[\mu_\mathrm{B}] = \frac{\mu_{eff}[J/T]}{\mu_\mathrm{B}} \tag{7.5}$$

Here, μ_B is the Bohr magneton ($9.274 \cdot 10^{-24}\,\mathrm{JT}^{-1}$) and $\mathrm{k_B}$ the Boltzmann constant ($1.380 \cdot 10^{-23}\,\mathrm{JK}^{-1}$).

μ_{eff} given in Table 7.3, deviates strongly from the value for Cr^{+3} (3.87 µB) and the μ_{eff} of $CuCrSe_2$ (3.62 - 3.87 µB) (Table 7.1). The μ_{eff} of the 1:1 sample is even higher than the μ_{eff} of $CuCr_2Se_4$ (6.0 µB). Colominas calculated a μ_{eff} of 6 µB if a cation Cu^+ occurs next to Cr^{+3}.[164] Therefore, the Cu_xCrSe_2 layer might contain a significant amount of Cu^+. A change in the Cr-Se-Cr angle also has a major impact

Table 7.3: Effective magnetic moment μ_{eff} per Cr and percentage of chromium assuming that only spin only Cr is present.

	1:1	1:2	1:3	1:5
μ_{eff} [J/T]	$5.5(9)\cdot10^{-23}$	$1.4(2)\cdot10^{-23}$	$1.1(2)\cdot10^{-23}$	$1.2(2)\cdot10^{-23}$
μ_{eff} [μ_B]	6(1)	1.5(2)	1.2(2)	1.3(2)
Cr %	155	38	31	33

on the magnetism in $CuCr_2Se_4$.[169] Distortions in the structure might be the cause of the increased μ_{eff} as well.

In Figure 7.8, temperature dependent plots of χ_{corr} and χ^{-1} are represented for the 1:2 samples annealed at 350 and 400 °C. It can be observed, that the sample annealed to 350 °C has a slightly stronger susceptibility, a slightly larger C, and a smaller θ as the sample annealed to 400 °C. For the calculation of the μ_{eff}, the in-plane lattice parameters were used. As for the 1:2 sample annealed at 350 °C, the X-ray diffraction pattern in in-plane geometry was not measured. Instead the in-plane lattice parameters of the annealed at 400 °C have been used for this sample. The Curie-Weiss temperature is significantly smaller for the 1:2 sample annealed at 350 °C than for the 1:2 sample annealed at 400 °C indicating a stronger antiferromagnetic coupling for the sample annealed at 350 °C. The Curie constant is slightly larger for a lower annealing temperature and the derived μ_{eff} is slightly larger for the sample annealed at 350 °C. The previous chapter showed that the samples annealed at 350 and 400 °C vary in their Se-Se distances which is probably caused by a variation in copper occupation. The sample annealed at 350 °C might therefore contain a higher amount of Cu^+, leading to a higher μ_{eff}. This indicates that the different heterostructures might have varying μ_{eff} depending on the Cu^+ distribution.

Field dependent isothermal magnetization measurements were performed between -2 T and 2 T. In order to determine the diamagnetic content in the field dependent measurements, linear fits between 1.7 and 2 T were performed. The corrected magnetization M was plotted against the applied filed.

The field dependent measurements reveal a significant magnetization despite the small magnetic volume of the samples. According to the temperature dependent χ measurements, the samples exhibit a decreased saturation magnetization (M_S) with increasing n, and the samples with $n = 1$, 2 have a coercivity (Hc) > 0. Multiple temperature dependent magnetization curves were measured (Figure 7.10) to analyze the temperature-dependent change in M_S and Hc. The coercivity (Figure 7.10, right) shows a clear trend towards zero with increasing temperature. This is in line with

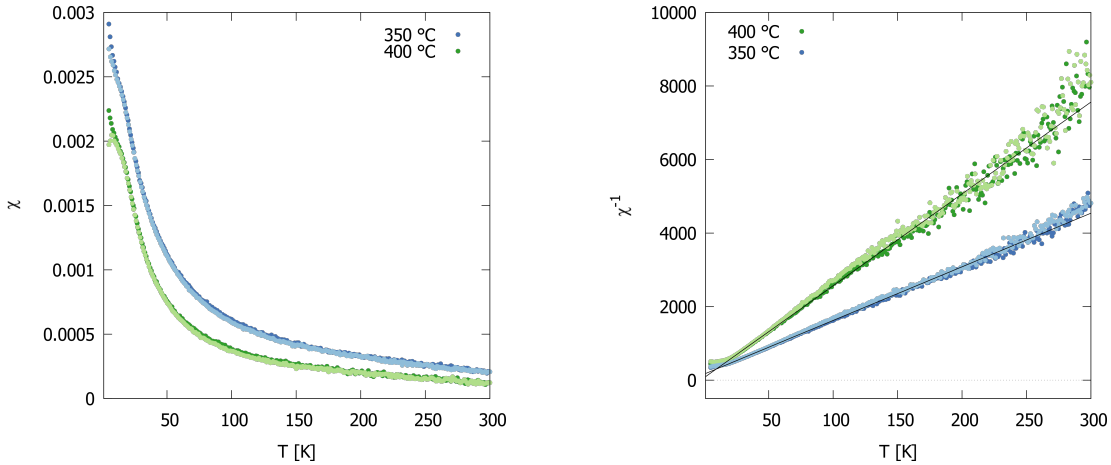

Figure 7.8: Temperature dependent corrected susceptibility and inverse susceptibility curves for the 1:2 samples of set 3 annealed at 350 and 400 °C. Samples were measured in FC and ZFC (pale colours) at 0.25 T.

Table 7.4: Correction parameters for the diamagnetic susceptibility χ_D, linear susceptibility χ_T, Curie constant C, Curie-Weiss temperature θ, effective magnetic μ_{eff} moment per Cr, and percentage of chromium assuming that only spin only Cr is present for 1:2 sample annealed at 350 and 400 °C.

	1:2 350 °C	1:2 400 °C
χ_T [K^{-1}]	$2.76(2)\cdot10^{-6}$	$2.19(2)\cdot10^{-6}$
χ_D [K^{-1}]	$-3.879(8)\cdot10^{-3}$	$-2.914(7)\cdot10^{-3}$
C [K]	0.0686(8)	0.0400(6)
θ [K]	-11.4(3)	-2.8(3)
μ_{eff} [J/T]	$1.8(2)\cdot10^{-23}$	$1.4(2)\cdot10^{-23}$
μ_{eff} [μB]	2.0(2)	1.5(2)
Cr %	51	38

the ZFC/FC measurements as a splitting in those measurements is only observed to ≈ 13 K. M_S as a function of temperature as expected a similar trend as the ZFC measurement (Figure 7.10).

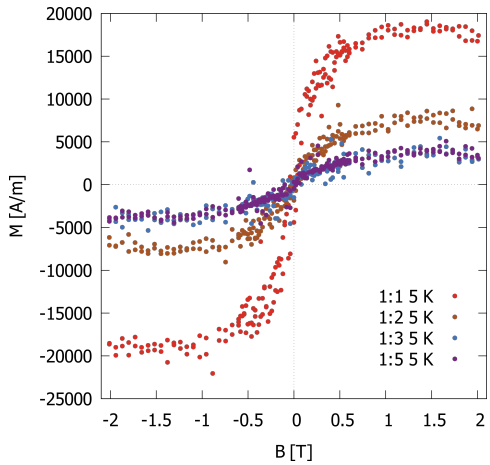

Figure 7.9: Field dependent magnetization curves at 5 K of the 1:1, 1:2, 1:3, and 1:5 sample of set 3 annealed at 400 °C.

Table 7.5: Saturation magnetization M_S and coercivity μ_0Hc derived the field dependent magnetization curves at 5 K.

	1:1	1:2	1:3	1:5
M_S [A/m]	19551(261)	8321(140)	4158(168)	4202(131)
μ_0Hc [T]	-0.04(1)	-0.03(1)	0	0

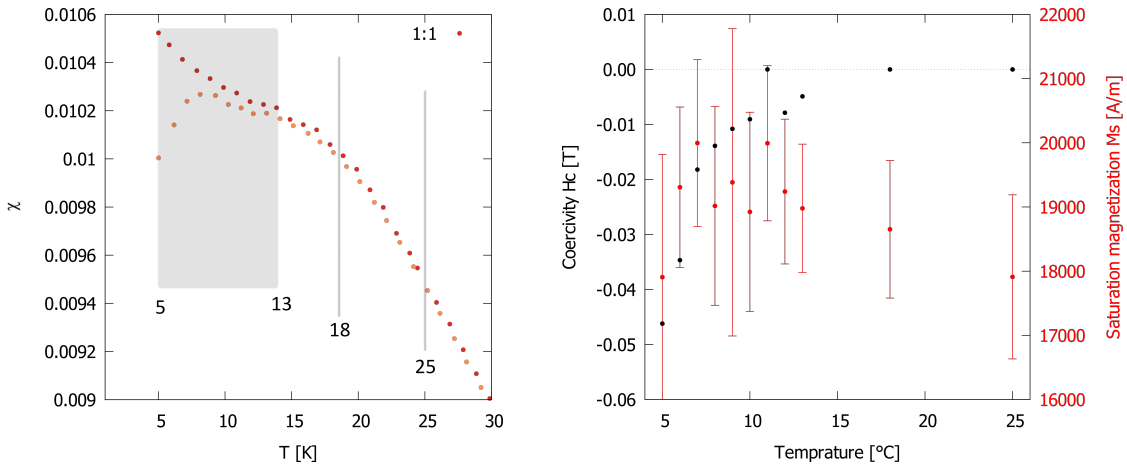

Figure 7.10: Temperature dependent corrected susceptibility for the 1:1 samples of set 3 annealed at 400 °C. The temperatures at which field depended measurements were performed are marked in the curve (left). Coercivity (left y-axis) and saturation magnetization (right y-axis) as a function of temperature (right).

7.6. Polarized neutron reflectometry

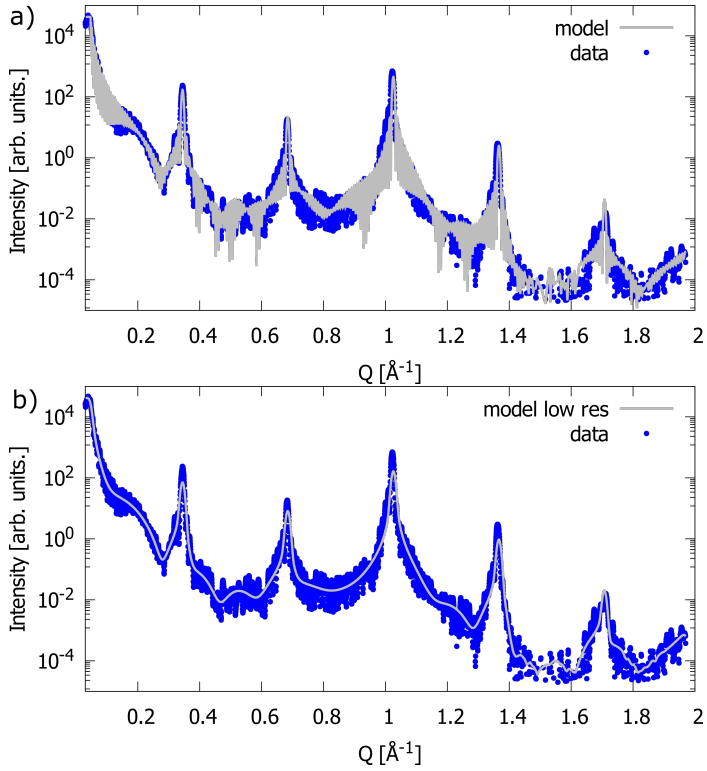

Figure 7.11: a) X-ray reflectometry data (blue) from the 1:1 sample annealed at 400 °C of set 3 and simulated data (continuous gray). b) The same data modelled with a lower resolution.

To obtain information about the depth resolved magnetometry of the modulated layers, polarized neutron reflectometry (PNR) experiments at 5 K were performed. Prior to the PNR measurements X-ray reflectometry (XRR) was performed to determine the nuclear scattering length density (SLD) profile. The *c*-lattice parameter was derived from the out-of plane diffraction patterns and not refined here. The refinement algorithm is based on the work of Bijerka *et al.*,[180] a detailed description can be found in chapter 9.3.5. Ferecrystals usually have a less smooth bottom and top area than the core of the nanolaminate. Thus, a substrate area and an end area are defined were the SLD is allowed to deviate from the periodic area. Figure 7.11 a) shows the measured XRR pattern and the simulated data. A second fit was performed with a lower resolution to suppress the Kiessig Fringes and model only the pattern shape. Both fits are observed to model the XRR pattern. The corresponding SLD profiles are represented in Figure 7.12. Both profiles have a similar modulation underlining the reliability of the profile. The periodic area in the SLD has 39 repetitions and three distinct modulations. The STEM images of 1:3 samples

in chapter 5.6 showed that the Cu_xCrSe_2 layer has a double layer structure. Two layers of the modulation would then correspond to the Cu_xCrSe_2 layer and one to the $NbSe_2$ layer. Two of the modulations have a higher SLD of $\approx 70{\cdot}10^{-6}$ Å^{-2} which is in the range of the bulk SLD of $CuCrSe_2$ (57.57 Å^{-2}) indicating that these correspond to the Cu_xCrSe_2 double layer. The third layer has a SLD slightly above the SLD of $NbSe_2$.

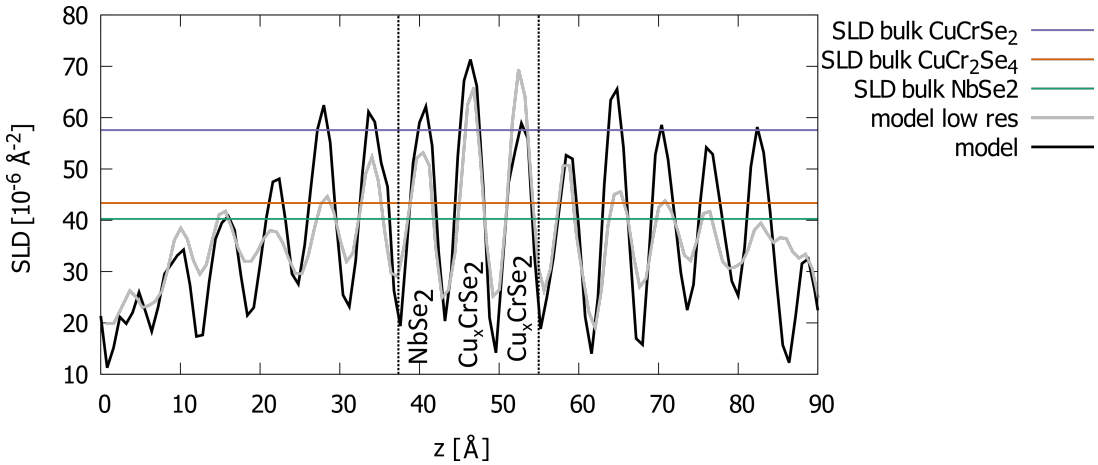

Figure 7.12: Scattering length density profile as a function of the distance z. Bulk SLD values are given in purple, orange, and green for $CuCrSe_2$, $CuCr_2Se_4$, and $NbSe_3$, respectively. The area between the dotted lines corresponds to the unit cell and has 39 repetition units.

For the 1:1 and 1:3 samples, PNR measurements at 5 K under field cooled conditions were conducted at MARIA, MLZ and the results are represented in Figure 7.13. The 1:1 sample exhibits a distinct splitting of R^+ and R^- which is not present in the 1:3 sample. This underlines that above $n = 2$ no measurable magnetic interlayer coupling occurs. The splitting in the higher Q range (0.7 - 0.1 Å^{-1}) is instrument related. Unfortunately, the real space resolution that can be derived from the PNR measurements is too low to distinguish the individual modulations in the SLD as for the XRR data. Therefore it was not possible to resolve the magnetic profile of the 1:1 sample. Further experiments should cover at least the first Bragg reflection (0.4 Å^{-1}) in order to get a reliable resolution of the SLD modulations.

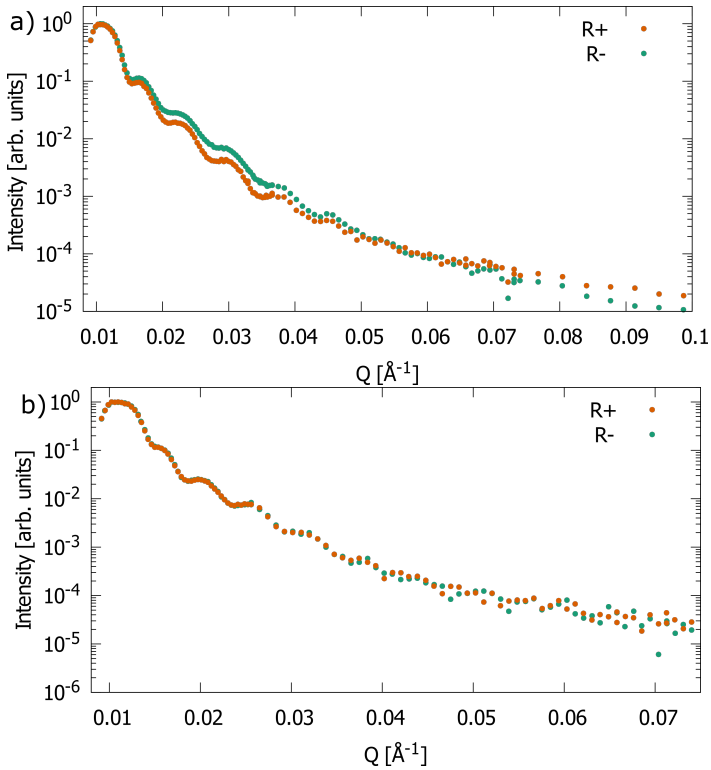

Figure 7.13: a) Polarized neutron reflectometry curve for the 1:1 sample at 5 K under FC conditions with an applied field of 1 T. b) Polarized neutron reflectometry curve for the 1:3 sample at 5 K under FC conditions with an field of 1 T.

7.7. Summary

Diffraction and electron microscopy data as well as Rietveld refinement data discussed in the previous chapters 5 and 6 indicated a Cu_xCrSe_2 structure. Variations in annealing temperature and time showed a significant effect on the structure of the ferecrystals 5. In order to investigate the effect of $NbSe_2$ layers repetitions n on the magnetic properties, samples with $n = 1$ - 5 were prepared (set 3). In-plane and out-of-plane diffraction patterns confirm that samples with a systematic change in n could be prepared. Set 3 could be prepared as heterostructure A and B by changing the annealing temperature from 350 °C to 400 °C.

Temperature dependent susceptibility measurements revealed a splitting of ZFC FC curves, which gives strong evidence that we prepared the first magnetic ferecrystals. The splitting of ZFC and FC is reduced with n revealing that the magnetic interlayer coupling depends strongly on n and is non detectable above $n = 2$.

The derived effective magnetic moment of the samples μ_{eff} is much higher for the 1:1 sample than for the bulk values of $CuCrSe_2$ or $CuCr_2Se_4$ indicating either the presence of Cu^+ or the change in Cr-Se-Cr angle. The 1:2 sample annealed at 350 °C has a

slightly higher μ_{eff} than the sample annealed at 400 °C. This reveals that the change in heterostructure due to a different annealing temperature also effects the magnetic properties of the samples. Rietveld refinements indicate increased copper intercalation into the $NbSe_2$ layers with increasing annealing temperature, which effects the change in heterostructure. The change in μ_{eff} might also be based on a change in copper occupation and an increase in concentration of Cu^+ in the Cu_xCrSe_2 layer with decreasing annealing temperature.
The SLD profile derived from XRR data underlined that the $Cu_xCr_ySe_z$ part of the structure is a derivative of $CuCrSe_2$. PNR showed a splitting in R^+ and R^- for the 1:1 sample but not for the 1:3 underlining the results of the ZFC FC measurements. An investigation of the magnetic modulation was not possible as the real space resolution that could be derived from the PNR data is not sufficient to distinguish the different layers in the unit cell. Future experiments should therefore measure at higher Q values to allow a clear assignment of the magnetic contribution to the different layers.

8. Conclusion and summary

Nanolaminates provide outstanding chemical, mechanical, and physical behaviours which are related to size-induced deviations of their atomic structure.[7] Understanding the nucleation process and the atomic structure of the nanolaminates enables the prediction and modification of their properties.

1:1 ferecrystals were investigated using reciprocal space mapping revealing interlayer correlations particular in $[10l]_{\mathrm{TSe_2}}$ $[20l]_{\mathrm{MSe}}$. These correlations may arise due to three different factors: the a_{MSe} and $b'_{\mathrm{TSe_2}}$ need to coincide, the transition metal dichalcogenide (TMD) should crystallize only in the 1T configuration, and the rock salt needs to be able to form a TMD during the nucleation step. This suggest that a wide range of 1:1 ferecrystals should contain interlayer correlations, but 1:1 ferecrystals without interlayer correlations may also exist. This model is critical in explaining the structure related properties in ferecrystals.

Using the modulated elemental reactants (MER) method, a new set of ferecrystals has been prepared exchanging the rock salt with a $\mathrm{Cu}_x\mathrm{Cr}_y\mathrm{Se}_z$ layer. These ferecrystals allow the preparation of four structurally different heterostructures from one precursor by varying the annealing temperature. This demonstrates the ability of the MER method to synthesize kinetic products which are not accessible by other synthesis methods. Future EDX line scans with higher resolution will give a better understanding of the different heterostructures and might enable the preparation of further ferecrystals with controlled heterostructure formation.

Rietveld refinement has been used to gain a better understanding of the structure in the $\mathrm{Cu}_x\mathrm{Cr}_y\mathrm{Se}_z$ layer. Comparing three different starting models, the goodness of fit indicates that the $\mathrm{Cu}_x\mathrm{Cr}_y\mathrm{Se}_z$ layer is made of a $\mathrm{Cu}_x\mathrm{CrSe_2}$ double layer structure. Rietveld studies on samples annealed at 350 and 400 °C indicate that the structural variations in the different heterostructures is based on the copper intercalation. This information is critical in later studies to understand the magnetic properties of the materials. The knowledge that copper might be essential for the heterostructure formation will be crucial for the preparation of future ferecrystals containing copper.

Temperature dependent susceptibility measurements revealed that $[(\mathrm{Cu}_x\mathrm{CrSe_2})_{1+\delta}]_1(\mathrm{NbSe_2})_n$ are the first magnetic ferecrystals. The distinct splitting of the polarized neutron reflectometry curves for the 1:1 raises the interesting question if the magnetism is based solely on the $\mathrm{Cu}_x\mathrm{CrSe_2}$ layer. Future PNR experiments will target a higher real space resolution to resolve the magnetic depth profile.

Furthermore, sample sets with a different TMD will reveal the influence of $NbSe_2$ on the structure and magnetic properties.

9. Experimental section

9.1. Sample preparation

All samples were prepared with the MER method (detailed description is given in section3.2). The deposition parameters for the samples are given in Table 9.1 and 9.2. A detailed explanation how the deposition parameters are calibrated is given in chapter 5.2. The amount of deposited $NbSe_2$ layers n was varied between 1 - 5. For different n no further calibration was necessary and only the amount of Nb|Se repetitions between Se|Cr|Cu|Cr|Se has to be varied according to the desired n. Different amounts of atoms hit the substrate than the crystal monitor due to the different orientation of crystal monitor and substrate to the source. This is regulated by the tooling factor.

Table 9.1: Parameters for preparation of $[(Cu_xCr_ySe_z)_{1+\delta}]_1(NbSe_2)_n$ samples.

	sample 1 and 4			sample 2 and 3			sample 5		
	Få	Rate	Tooling Factor	Få	Rate	Tooling Factor	Få	Rate	Tooling Factor
Nb	7.7	0.2	64	7.8	0.2	64	7.8	0.2	64
Se	8.3	0.5	65	8.3	0.5	68	8.3	0.5	68
Se	7.4	0.5	65	7.4	0.5	68	7.4	0.5	68
Cr	5.1	0.2	64	3.3	0.2	68	64	0.2	64
Cu	4.1	0.2	64	4.5	0.2	68	64	0.2	64
Cr	5.1	0.2	64	3.3	0.2	68	64	0.2	64
Se	7.4	0.5	65	7.4	0.5	64	68	0.5	68

The as deposited precursors were transferred into a glove box and annealed on a hot plate to temperatures between 100 and 600 °C.

9.2. Instruments

9.2.1. Bruker AXS D8

High angle and low angle X-Ray diffraction experiments were carried out on a *Bruker AXS D8* X-ray diffractometer with $CuK_{\alpha 1}$ radiation ($\lambda = 1.54051$ Å) at the University of Oregon *Center for Advanced Materials Characterization* (CAMCORE), Eugene,

Table 9.2: Parameters for preparation of the $[(Cu_xCr_ySe_z)_{0.5}]_{1+\delta}(NbSe_2)_3$ sample 6.

sample 6			
	Få	Rate	Tooling Factor
Nb	7.7	0.2	64
Se	8.3	0.5	65
Se	3.7	0.5	65
Cr	2.6	0.2	64
Cu	2.1	0.2	64
Cr	2.6	0.2	64
Se	3.7	0.5	65

USA. A series of alignment measurements was made with every sample to correct the sample position.
Wide angle $\theta/2\theta$ measurements were performed in the range of $2\,\theta$ = 6.0 - 65.1 and a step size of 0.1. The exit beam was modulated with a 0.6 mm slit and a Nickel filter. X-ray reflectivity measurements were performed in the range of $2\,\theta$ = 0 - 7.0 and a step size of 0.01. The exit beam was modulated with a 0.1 mm slit.

9.2.2. ID03

Synchrotron X-ray scattering was measured at the *ID03*[181] beamline at the *European Synchrotron Radiation Facility (ESRF)*, Grenoble, France. An incident X-ray energy of 24 keV was used. Sample detector (*maxipix* detector) distance was 940 mm, the beam size $100 \cdot 50\,\mu$m with the central pixel at 339, 329 (referred to as ID03-1). The pixel size is 0.055 mm. In a second beamtime (referred to as ID03-2) was the sample detector distance 961 mm, the beam size $600 \cdot 30\,\mu$m with the central pixel at 164, 292. The pixel size is 0.055 mm.
All measurements were performed at room temperature. For data reduction of the X-ray diffraction patterns in in-plane ($hk0$) geometry and the reciprocal space maps the *BINoculars* software was used.[182,183]
Background correction and data reduction of X-ray diffraction patterns in out-of-plane ($00l$) geometry were performed with the *aps_slicereduce* program written by Dominique Dresen, University of Cologne, Germany (section 9.3.2).

9.2.3. BM-33-C

Synchrotron X-ray scattering using a *Pilatus 100K* detector was measured at the *BM-*

33-C beamline at the *Advanced Photon Source (APS)*, Chicago, USA. An incident X-ray energy of 16 keV was used. Sample detector distance was 1115 mm, the beam size 900 · 500 μm with the central pixel at 214, 90. The pixel size is 0.172 mm. All measurements were performed at room temperature. Background of the X-ray diffraction patterns in in-plane ($hk0$) geometry were corrected with the *substract_two_areas* code written by Dominique Dresen. A defined area on the edge of the detector image is defined as background and subtracted form each image. The data reduction was performed with *powderscan* by the APS which works similar to the *BINoculars* code. Background correction and data reduction of X-ray diffraction patterns in out-of-plane ($00l$) geometry were performed with the *aps_slicereduce* code written by Dominique Dresen (section 9.3.2).

9.2.4. Electron probe microanalyzer

The atomic ratios of the amorphous and crystalline materials where determined using the *Cameca SX50* electron probe microanalyzer. An 8 mm square section was cut out of the samples and glued on an aluminium sample holder. The sites of the sections were painted with carbon to provide a conductive path to the sample holder.

9.2.5. XRF

XRF measurements were performed on a *Rigaku ZSX-II* at room temperature. The instrument belongs to the *CAMCORE*, Eugene, USA. The instrument was calibrated with films whose compositions were determined by electron probe microanalyzer. The film contained a range of Cu, Cr, Nb and Se contents.

9.2.6. MARIA

Polarized neutron reflectometry measurements were performed at the *MAgnetic Reflectometer with high Incident Angle (MARIA)*[184] at the *Heinz Maier-Leibnitz Zentrum (MLZ)*, Garching, Germany. The instrument is operated by the *Jülich Center for Neutron Science (JCNS)*. Wavelength selection is achieved by a velocity selector. The incident beam is polarized by a polarizing guide, the expected polarized flux is 5 · 10^7 n cm^{-2} s^{-1} for 3 mrad collimation. The sample detector distance was 1910 mm, the beam size was 50 · 50 mm with the central pixel at 24, 600. The pixel size was 0.63 mm.

The applied field of 1 T was generated by a *Bruker electromagnet*. The sample was cooled by a He closed cycle cryostat to 5 K. The used neutron wavelength was 6 Å. Measurements were performed in the range of Q = 0.01 - 0.44 $Å^{-1}$

9.2.7. STEM

The STEM samples were prepared by the method developed by Schaffer *et al.* using a *FEI Helios D600*.[185] Schaffer *et al.* modified the known in-situ lift out technique[186] by applying a thick protective carbon layer. In second steps wedges are milled with a thinner bottom, while getting thinner the sides are adjusted to get parallel. Therefore, the protective layer will not be destroyed during thinning. An *Omniprobe 200* was used for the in-situ lift-out. STEM images were acquired on an FEI aberration-corrected *Titan 80-300*. All instruments belong to the *CAMCORE*, Eugene, USA. Gray values along the c-axis were determined using *ImageJ* by *National Institute of Health*, USA.[187]

9.2.8. STEM and EDX at PNNL

Samples were prepared according to the description in chapter 9.2.7. STEM images and EDX measurements were performed on an FEI aberration-corrected *Titan G2 80-200* with an acceleration voltage of 200 kV at the *Pacific Northwest National Laboratory (PNNL)*, Portland, USA. The instrument is equipped with array of four *FEI SuperX* windowless X-ray detectors. To improve the quality of the EDX spectrum images, an integration over multiple drift corrected frames was conducted. Measurements and data processing were performed by Dr. Gavin Mitchson and Dr. Jeffrey Ditto.

9.2.9. STEM and EDX at ER-C

Samples were prepared according to the description in section 9.2.7 using an *FEI Helios NanoLab 400S* at the *Ernst Ruska-Centre for Microscopy and Spectroscopy with Electrons (ER-C)*, Jülich, Germany. STEM images and EDX measurements were performed on an FEI aberration-corrected *Titan G2 80-200 CREWLEY* with an acceleration voltage of 200 kV at the *ER-C*. The instrument is equipped with a *FEI SuperX* EDX System with 120 mm^2 Combined Detector Area. Measurements and data processing were performed by Dr. Andras Kovacs.

9.2.10. SQUID

Temperature and field dependent magnetic moment measurements were performed at an *MPMS-XL SQUID Magnetometer* by *QuantumDesign*. The instrument belongs to the *JCNS*, Jülich, Germany. Samples were placed in a plastic straw which was sealed at the bottom with a plastic plug. The width of the sample was slightly larger than the diameter of the straw so the sample would be fixed without any additional attachment. The straw was pulled over the sample holder. Sample holder and plastic plug were secured with kapton tape. To enable the evacuation of the straw and prevent oxygen contamination it was punctured at the bottom with a needle. As all samples were weakly magnetic, a piece of floppy disk was placed on the back of the sample and attached with sticky tape. To protect the straw from contamination the sample was covered with a layer of sticky tape that was removed after the sample alignment. For centering multiple scans were performed until the sample position is 2 cm.

For all scans three measurements per point, with two scans per measurements, were performed. Zero field cooled measurements were performed between 5 and 300 K with a heating rate of 0.5 K/min and measuring in 1 K increments. The samples were cooled down in zero field, and after reaching 5 K the desired magnetic field (0.25 T) was applied and the sample heated to 300 K. Field cooled measurements were performed like ZFC measurements except that the field was applied prior cooling down.

Sample area $A_{\text{Si wafer}}$ was calculated from its weight m_{sample} and thickness h_{wafer} using the density of silicon ρ_{Si} (2.336 g/cm^3) (equation 9.1 and 9.2) as the weight of the sample is below the sensitivity of the used scale. Using the total film thickness h_{film} determined with the XRR data the volume V_{sample} of the film can be calculated (equation 9.3). The wafer thickness was determined with Micrometer by *Multoyo* with an accuracy of 0.01 mm. The susceptibility was calculated with equation 9.4.

$$V_{wafer} = m_{sample} * \rho_{\text{Si}} \tag{9.1}$$

$$A_{\text{Si wafer}} = V_{\text{wafer}}/h_{\text{wafer}} \tag{9.2}$$

$$V_{\text{sample}} = A_{\text{Si wafer}} * h_{\text{film}} \tag{9.3}$$

$$\chi = \frac{M[\text{emu/cm}^3]\cdot 10^3}{H[\text{Oe}]\cdot\frac{10^3}{4\pi}} = \frac{M[\text{emu/cm}^3]}{H[\text{Oe}]}\cdot 4\pi = \frac{M[\text{A/m}]}{H[\text{A/m}]} \tag{9.4}$$

9.3. Programs

9.3.1. Layer thickness

The total layer thickness of the samples was determined from the Kiessig fringes observed using XRR. The critical angle θ_c and fringe angles θ_i were determined with *Diffract Eva* by *Bruker*.

9.3.2. aps slicereduce

The *aps_slicereduce* code was written by Dominique Dresen. In the first step pixel ranges for a background slice and a specular slice were defined. The individual images generated by the 2D detectors then were corrected and rebinned to a rotated coordinate system. Usual rebinning algorithms use a near neighbour method. *aps_slicereduce* uses a pixel splitting. The rebinning algorithm used by *aps_slicereduce* performs a transformation from detector width coordinates into incident angles. The transformed data is saved on an evenly spaced rectangular grid. A rectangular area on the detector is not necessarily rectangular after transformation. The informations of the transformed rectangle is partitioned and assigned to the new rectangle. The new rectangle gets a proportional partition of the information depending on the degree of overlap between the old and new rectangle. The code of the rebinning algorithm is given in appendix chapter E.
The motor positions and corresponding angles are read from the spec file. Especially in the area of high intensity reflections the scaling of the background is not correct, therefore a background roi at the edge of the detector is defined and subtracted.
In a second step the data is transformed to 2θ and in the final step xy-files of the specular and off-specular part of the scan are generated.

9.3.3. Le Bail fits and Rietveld refinements

Le Bail[121] fits and Rietveld[188] refinements were carried out with the *General Structural Analysis System (GSAS)*[189] *EXPGUI*[190] software package. The background was fit using a shifted Chebyschev polynomial.

9.3.4. Fits

All fits that are not stated differently were performed with the built-in fit function of *Gnuplot*.

Yannic Falke, University of Cologne, assisted writing the code for the Gaussian fits of the intensity profiles along Q_z using the python package NumPy.

9.3.5. Refinement of X-ray reflectivity data

For refinement of XRR data the *periodic_reflectometry* code written by Dominique Dresen, University of Cologne was used. The algorithm in *periodic_reflectometry* is based on the algorithm of Bijkerka *et al.*.[180] For the refinement sublayers of the substrate area, the periodic area, and the end area of the sample are defined. The optimum thickness of these sublayers d_{min} is defined by the maximal measured scattering vector Q_{max}:[180]

$$d_{min} = \frac{\pi}{2Q_{max}} \tag{9.5}$$

For the analyzed XRR data d_{min} is 0.8 Å.
χ^2 is supplemented to a regulation factor that reduces big steps in the SLD profile by motivating the second derivative to be minimized. A focus of the refinement on the first data points with high intensity and low deviations was avoided modifying χ^2 to:

$$\chi^2 = \sum (log(\text{model}) - log(\text{data}))^2 \tag{9.6}$$

The SLD of the first point was fixed to the substrate SLD (silicon) and the SLD of the last point (air) was fixed to 0.

9.3.6. Diamond

For visualization of crystal structures *Diamond* - Crystal and Molecular Structure Visualization Software by *Crystal Impact* was used.

Appendix

A. Interlayer correlations in 1:1 ferecrystals

A.1. Le Bail and Rietveld refinement

Table A.1: Le Bail fit results of the X-ray diffraction patterns in in-plane geometry.

	$[SnSe]_{1.14}[VSe_2]$		$[SnSe]_{1.21}[TiSe_2]$		$[PbSe]_{1.11}[VSe_2]$	
	SnSe	VSe_2	SnSe	$TiSe_2$	PbSe	VSe_2
Space group	*I4*	$P\bar{3}m1$	*Pcmn*	$P\bar{3}m1$	*I4*	$P\bar{3}m1$
a [Å]	5.919(1)	3.403(1)	5.969(6)	3.555(2)	6.079(3)	3.435(3)
b [Å]	$= a$	$= a$	6.078(3)	$= a$	$= a$	$= a$
GU	2912(46)	1023(95)	8218(254)	6639(457)	11750(422)	16060(1238)
GV	0	0	0	0	0	0
GW	0	0	0	0	0	0
LX	0	0	0	0	0	0
LY	50.2(9)	45(2)	131(2)	132(5)	189(3)	71(11)
wRp	0.0647		0.0443		0.0605	
RP	0.0469		0.0351		0.0475	
Zero Shift [$Å^{-1}$]	0.0048(2)		0.0022(6)		0.0091(6)	
Instrument	ID03-1		ID03-1	ID03-2	ID03-2	

Table A.2: Le Bail fit results of the X-ray diffraction patterns in in-plane geometry.

	$[BiSe]_{1.11}[NbSe_2]$		$[BiSe]_{1.15}[TiSe_2]$	
	BiSe	$NbSe_2$	BiSe	$TiSe_2$
Space group	*Pcmn*	$P\bar{3}m1$	*Pcmn*	$P\bar{3}m1$
a [Å]	4.50(1)	3.497(6)	4.565(3)	3.590(2)
b [Å]	4.25(1)	$= a$	4.247(3)	$= a$
GU	4.675(199)	32040(3247)	292(41)	4082(368)
GV	0	0	0	0
GW	0	0	0	0
LX	0	0	0	0
LY	432(16)	138(15)	245(4)	106(5)
wRp	0.0374		0.0450	
RP	0.0281		0.0346	
Zero Shift [$Å^{-1}$]	0.019(2)		0.0172(6)	
Instrument	ID03-2		ID03-2	

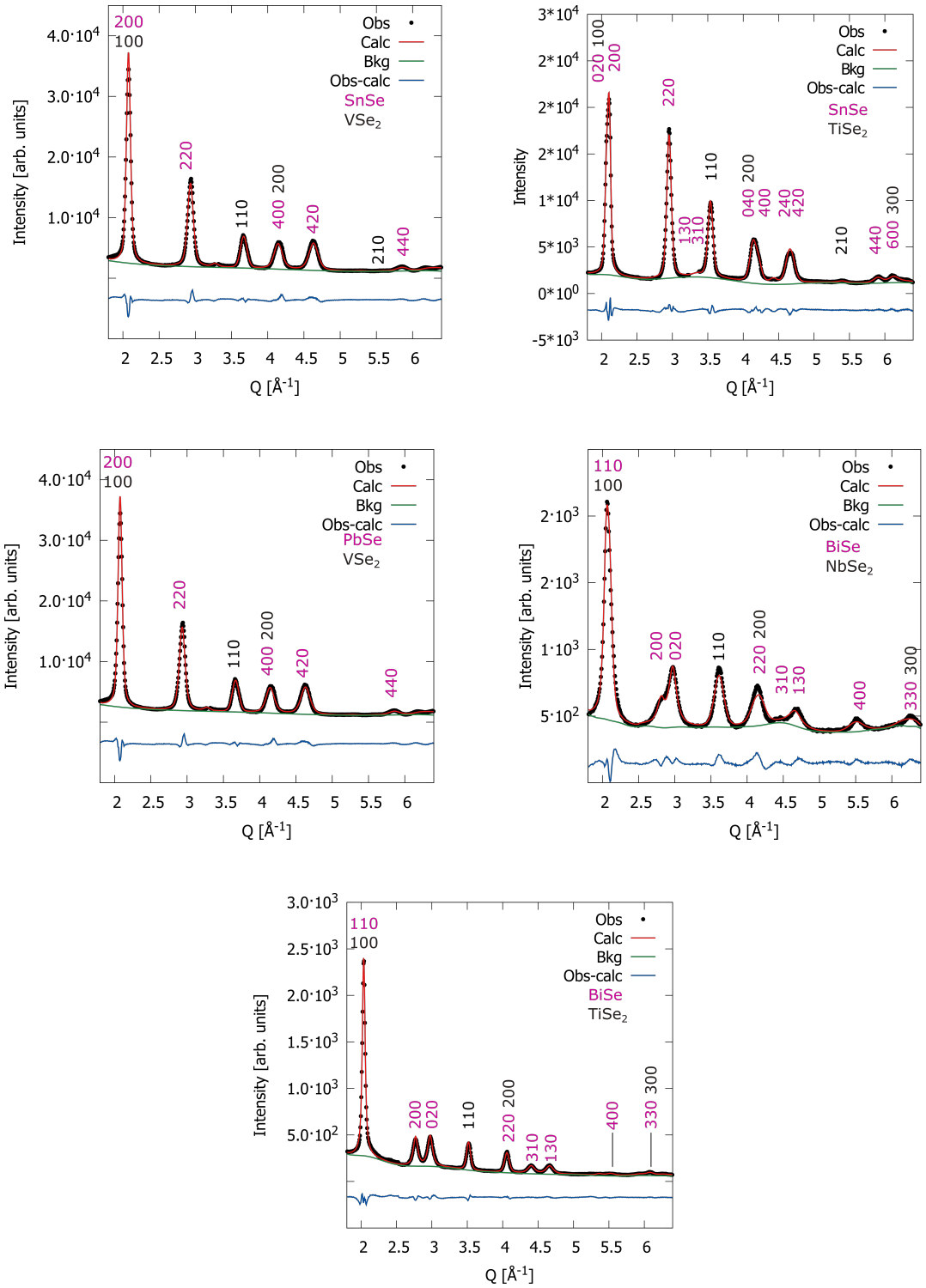

Figure A.1: X-ray diffraction patterns in in-plane geometry with Le Bail fit background and difference between the experimental and the simulated pattern.

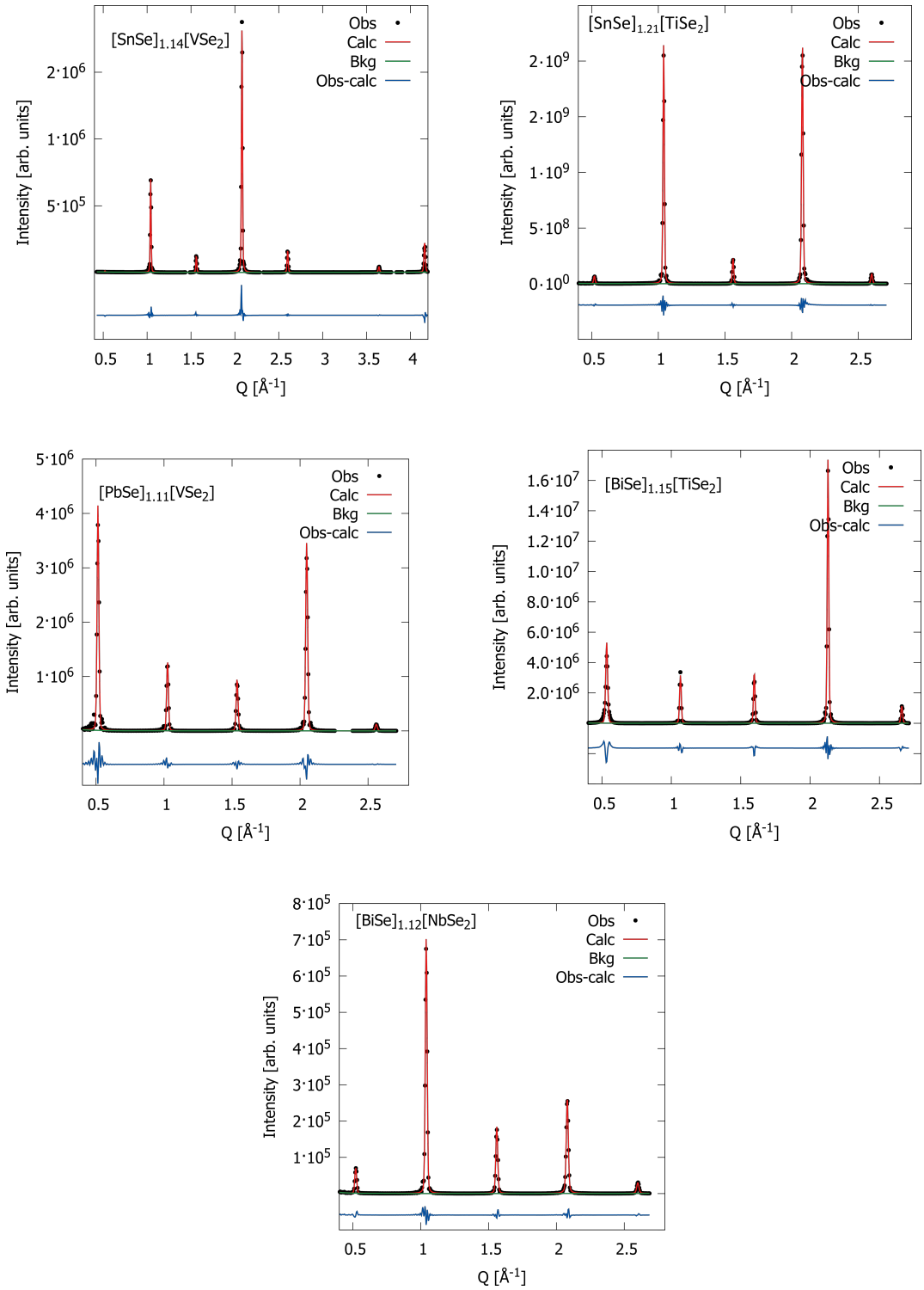

Figure A.2: X-ray diffraction patterns with out of plane geometry with the calculated fit background and difference between the experimental and the simulated pattern.

Table A.3: Le Bail fit and Rietveld results. M = Sn, Pb T = V, Ti * Not refined

	$[SnSe]_{1.14}[VSe_2]$		$[SnSe]_{1.21}[TiSe_2]$		$[PbSe]_{1.11}[VSe_2]$	
	Le Bail	Rietveld	Le Bail	Rietveld	Le Bail	Rietveld
Space group	$P\bar{3}m1$		$P\bar{3}m1$		$P\bar{3}m1$	
c [Å]	12.079(2)		12.083(2)		12.282(6)	
GU	0		229(24)		829(357)	
GV	0		0		-81(39)	
GW	5.3(1)		4.0(1)		8.9(9)	
LX	0		1.34(2)		1.21(8)	
LY	23(5)		0		0	
wRp	0.1039	0.1453	0.1255	0.1595	0.2615	0.2631
RP	0.0949	0.1002	0.0725	0.0765	0.1598	0.1683
Zero Shift [$Å^{-1}$]	0.00057(8)		0.0004(1)		0.0025(2)	
Scale		86(2)		120.6(122)		12
	z	Occ	z	Occ	z	Occ
T	0	1	0	1	0	1
Se	0.1284(2)	1	0.1155(3)	1	0.1294(5)	1
M	0.3729(4)	0.55*	0.3729(4)	0.588(1)	0.3634(7)	0.559(2)
Se	0.4046(5)	0.55*	0.4182(3)	0.588(1)	0.424(2)	0.559(2)
Uios [$Å^2$*100]	1.6(3)		2.5*		20(1)	

Table A.4: Le Bail fit and Rietveld results. M = Sn, Pb T = V, Ti * Not refined

	$[BiSe]_{1.11}[NbSe_2]$		$[BiSe]_{1.15}[TiSe_2]$	
	Le Bail	Rietveld	Le Bail	Rietveld
Space group	$P\bar{3}m1$		$P\bar{3}m1$	
c [Å]	12.091(3)		11.817(3)	
GU	770(287)		1313(259)	
GV	-66(33)		-192(34)	
GW	8.9(9)		11(1)	
LX	0.9(2)		2.02(4)	
LY	1.6(5)		0	
wRp	0.1358	0.1453	0.2322	0.2760
RP	0.0804	0.1002	0.1412	0.1448
Zero Shift [$Å^{-1}$]	0.00057(8)		0.0023(2)	
Scale		86(2)		120.6(122)
	z	Occ	z	Occ
T	0	1	0	1
Se	0.1284(2)	1	0.1258(6)	1
M	0.3729(4)	0.55*	0.3683(9)	0.536(4)
Se	0.4046(5)	0.55*	0.411(2)	0.536(4)
Uios [$Å^2$*100]	1.6(3)		2.5*	

A.2. Reciprocal space maps and Gaussian fits

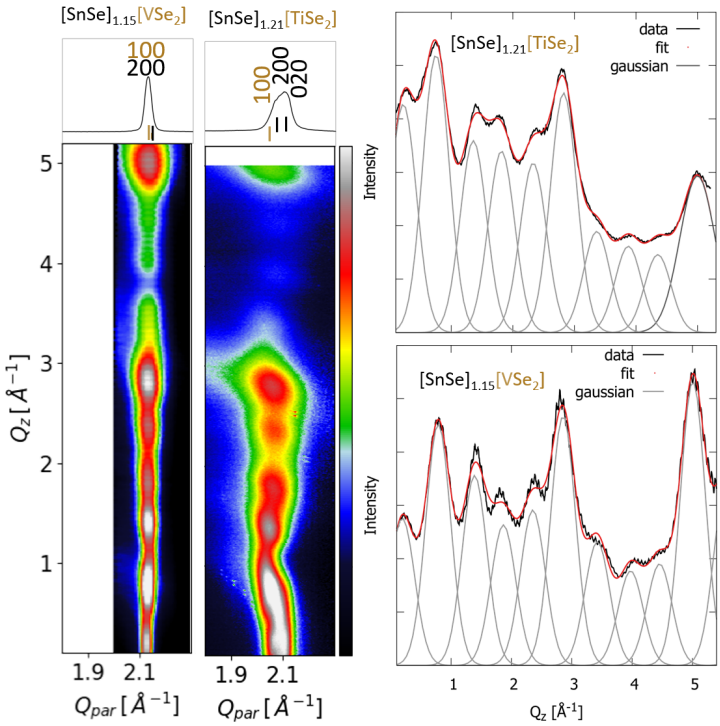

Figure A.3: Intensity profiles of the reciprocal space maps along Q_z (left) with Gaussian fits of SnV (@ID03-1) and SnTi (@ID03-2) (right).

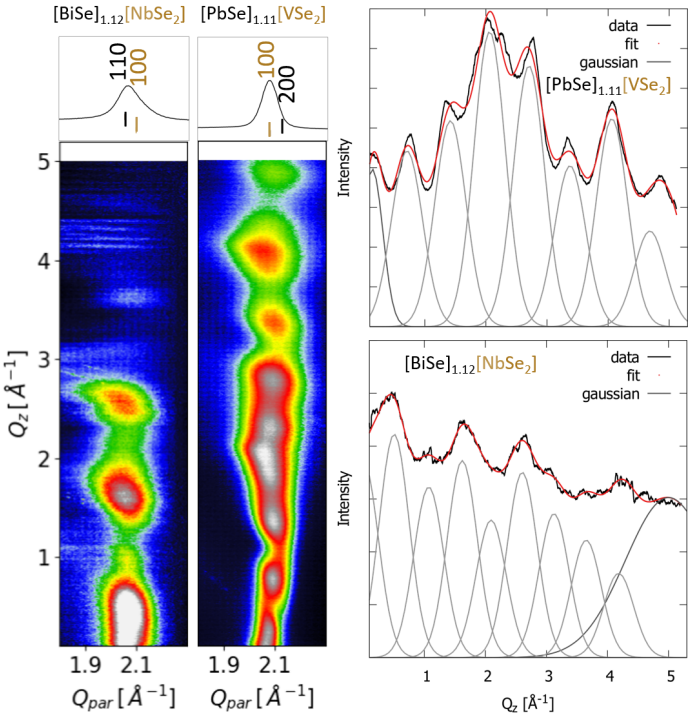

Figure A.4: Intensity profiles of the reciprocal space maps along Q_z (left) with Gaussian fits of PbV (@ID03-2) and BiTi (@ID03-2) (right).

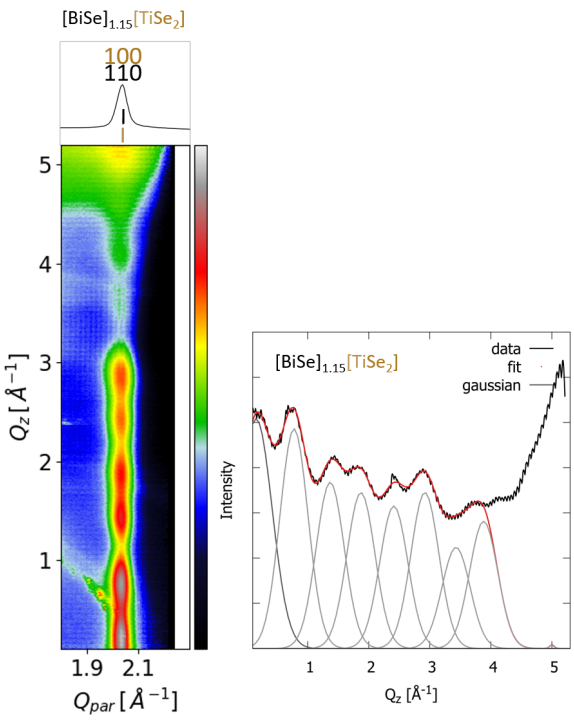

Figure A.5: Intensity profiles of the reciprocal space maps along Q_z (left) with Gaussian fits of BiNb (@ID03-2) (right).

A.3. X-ray diffraction patterns of ferecrystals with m, n $\neq$ 1

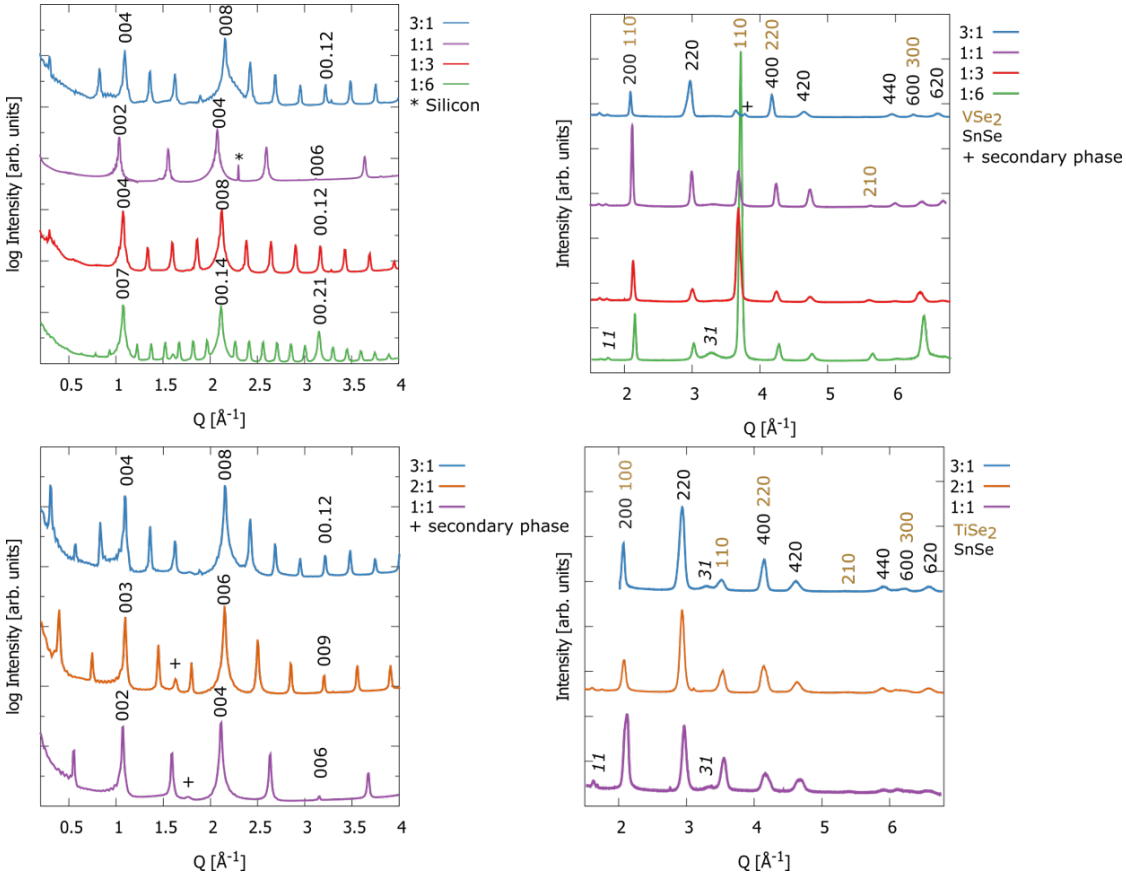

Figure A.6: In-plane and out of plane X-ray diffraction patterns of SnV (top) and SnTi (bottom) ferecrystals.

In the (00l) and (hk0) X-ray diffraction scans, a few Si and secondary phase reflections are present. The in-plane diffraction data displays the increasing relative intensities expected for increasing m,n. Broad (11) and (31) reflections are observed in the rock salt phases. These are systematically extinct for the 3D crystal structures, but allowed for this 2D projection of the structure.[99] The obtained results are consistent with previously published data.[103,108,109] All scans were performed at ID03-2.

B. $[(Cu_xCr_ySe_z)_{1+\delta}]_1(NbSe_2)_3$ ferecrystals

B.1. Total thickness and c-lattice parameter of the 1:3 samples

Table B.1: c-lattice parameters and total thickness of the 1:3 samples 2 and 3 and their corresponding heterostructures

	sample 2		sample 3	
	Total thickness [Å]	c [Å]	Total thickness [Å]	c [Å]
ad	1019(2)	33.20(4)	1010(10)	32.6(1)
350 °C	987(2)	31.95(3)	950(6)	31.77(2)
400 °C	931(1)	31.50(7)	926(4)	31.48(1)
500 °C	932(4)	31.46(2)	-	-
600 °C	926(3)	31.34(4)	919(3)	31.1(1)

All scans on sample 1 and 2 were performed on the Bruker AXS D8.

Table B.2: Instruments used for measuring the out-of-plane diffraction patterns of 1:3 samples 2 and 3 and their corresponding heterostructures

	sample 3	sample 4	sample 5
	Instrument	Instrument	
ad	Bruker AXS D8	Bruker AXS D8	-
350 °C	BM-33-C	BM-33-C	Bruker AXS D8
400 °C	BM-33-C	ID03-2	BM-33-C
600 °C	BM-33-C	Bruker AXS D8	Bruker AXS D8

Table B.3: c-lattice parameters and total thickness of the 1:3 samples 4 and 5 and their corresponding heterostructures

	sample 4		sample 5	
	Total thickness [Å]	c [Å]	Total thickness [Å]	c [Å]
ad	996(12)	32.3(1)	-	-
350 °C	-	-	1012(10)	32.18(7)
400 °C	956(12)	31.87(5)	928(5)	31.6(1)
500 °C	-	-	-	-
600 °C	-	-	812(22)	31.5(1)

B.2. Le Bail fit of hk0 data

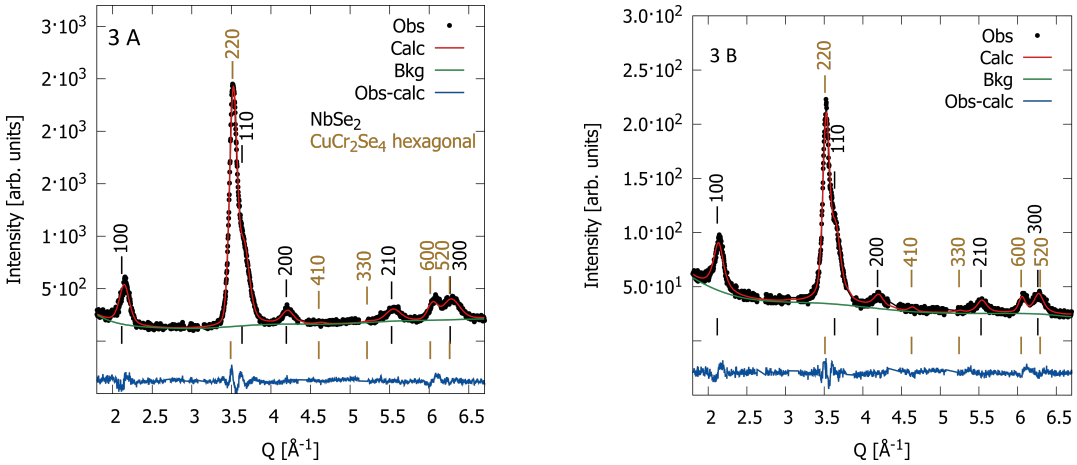

Figure B.1: Gazing incident diffraction patterns of the $[(Cu_xCr_ySe_z)_{1+\delta}]_1[NbSe_2]_3$ samples with Le Bail fit background and difference between experimental and simulated pattern of sample 3 with heterostructure A and B.

In-plane diffraction patterns of samples 3 A, 3 B, and 5 B performed on BM-33-C. In-plane diffraction pattern of sample 4 B was performed on ID03-2.

Table B.4: Le bail fit results of the x-ray diffraction patterns in in-plane geometry of sample 3 with heterostructure A and B.

	Sample 3 A		Sample 3 B	
	$Cu_xCr_ySe_z$	$NbSe_2$	$Cu_xCr_ySe_z$	$NbSe_2$
Space group	$R\bar{3}m$	$P\bar{3}m1$	$R\bar{3}m$	$P\bar{3}m1$
a [Å]	7.293(4)	3.508(6)	7.258(9)	3.504(6)
GU	8293(1207)	54860(5605)	0	0
GV	0	-17390(2559)	0	0
GW	619(64)	2340(292)	586(30)	387(81)
LX	9.5(9)	56(2)	28(1)	92(2)
LY	0	0	0	0
wRp	0.0771		0.0569	
RP	0.0591		0.0450	
Zero Shift [$Å^{-1}$]	0.119(2)		0.096(2)	

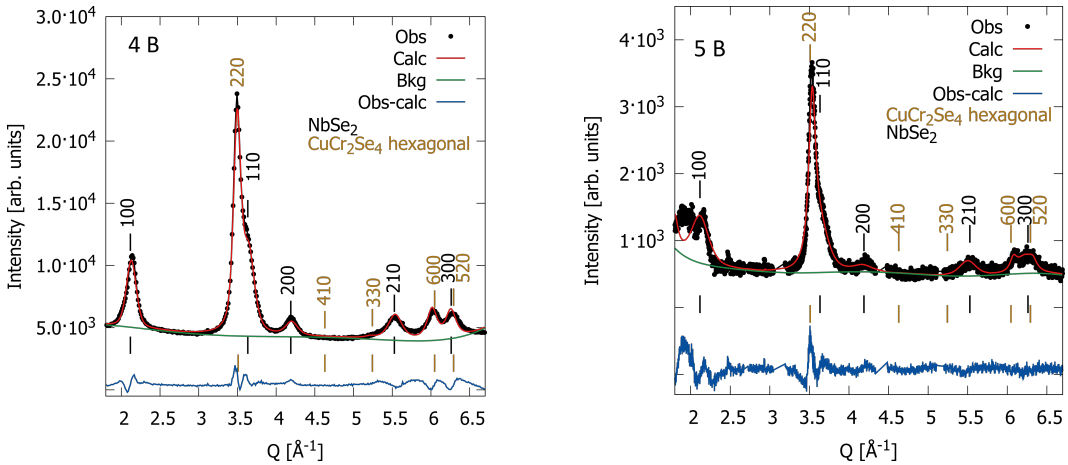

Figure B.2: Gazing incident diffraction patterns of the $[(Cu_xCr_ySe_z)_{1+\delta}]_1[NbSe_2]_3$ samples with Le Bail fit background and difference between experimental and simulated pattern of sample 4 and 5 with heterostructure B.

Table B.5: Le bail fit results of the x-ray diffraction patterns in in-plane geometry of sample 4 and 5 with heterostructure B.

	Sample 4 B		Sample 5 B	
	$Cu_xCr_ySe_z$	$NbSe_2$	$Cu_xCr_ySe_z$	$NbSe_2$
Space group	$R\bar{3}m$	$P\bar{3}m1$	$R\bar{3}m$	$P\bar{3}m1$
a [Å]	7.30(1)	3.501(9)	7.228(9)	3.526(6)
GU	0	0	0	0
GV	0	0	0	0
GW	576(46)	192(20)	2856(354)	110(45)
LX	0	0	96(6)	63(2)
LY	300(13)	235(7)	0	0
wRp	0.0345		0.1141	
RP	0.0282		0.0870	
Zero Shift [$Å^{-1}$]	0.057(2)		0.089(2)	

B.3. XRF data of 1:3 data

Table B.6: Atomic % in sample 3 A, 3 B, 4 B, and 5 B determined by XRF.

Sample	Cr [at %]	Cu [at %]	Nb [at %]	Se [at %]
3 A	10.588	2.933	19.249	67.002
3 B	10.829	2.932	19.870	66.130
4 B	13.443	5.941	17.555	62.928
5 B	7.615	5.759	19.881	66.503

C. Structural investigation of the $Cu_xCr_ySe_z$ constituent

C.1. Rietveld refinement of 1:2 sample of set 3 annealed at 350 °C

The measurements were performed at BM-33-C at the APS.

Table C.1: Le bail fit results of the X-ray diffraction patterns in out-of-plane geometry of 1:2 sample of set 3 annealed at 350 °C.

Space group	$P\bar{3}m1$
c [Å]	25.315(6)
GU	1941(135)
GV	129(27)
GW	21(2)
LX	3.04(6)
LY	0
wRp	0.1443
RP	0.0815
Zero Shift [$Å^{-1}$]	0.0106(2)

Table C.2: Rietveld results for the Cu and Cr-deficient models. * not refined in last refinement

Cu-deficient				Cr-deficient			
wRp	0.1451			wRp	0.1461		
Rp	0.0814			Rp	0.0816		
Scale	345(5)			Scale	451()		
	z	Occ Rietveld	Occ bulk		z	Occ Rietveld	Occ bulk
Se1	0.0767(2)	1	1	Se1	0.7486*	1	1
Nb1	0.1298(1)	1	1	Nb1	0.1300*	1	1
Se2	0.1814(2)	1	1	Se2	0.1886*	1	1
Se3	0.329(2)	0.77(1)	0.910	Se3	0.3204*	0.892(2)	0.910
Cr1	0.322(8)	0.24(4)	0.683	Cu1	0.3704*	0.496(2)	0.228
Se4	0.3828(7)	0.77(1)	0.910	Cr1	0.3743*	0.496(2)	0.228
Cu1	0.4368(3)	0.30(1)	0.228	Cu2	0.4040*	0.496(2)	0.228
Cr2	0.5	0.228	0.228	Se4	0.4420*	0.892(2)	0.910
				Cr2	0.5	0.404(5)	0.683
Uios [Å^2*100]	14.0(5)				14.5*		

Table C.3: Rietveld results for the symmetric and asymmetric $CuCrSe_2$ models. * not refined in last refinement

$CuCrSe_2$ sym			$CuCrSe_2$ asym		
wRp	0.1453		wRp	0.1457	
Rp	0.0822		Rp	0.0822	
Scale	367(5)		Scale	368(5)	
	z	Occ Rietveld		z	Occ Rietveld
Se1	0.0758(2)	1	Se1	0.0758(2)	1
Nb1	0.1298(1)	1	Nb1	0.1297(1)	1
Se2	0.1821(2)	1	Se2	0.1823(2)	1
Se3	0.3282(2)	0.988(2)	Se3	0.3280(3)	0.985(2)
Cr1	0.3841(2)	0.988(2)	Cr1	0.3838(3)	0.985(2)
Se4	0.4338(3)	0.988(2)	Se4	0.4333(3)	0.985(2)
Cu1	0.5	0.30(1)	Cu1	0.4906*	0.33(1)
Uios [Å^2*100]	15.7(4)				15.7(4)

C.2. Le Bail fit and Rietveld refinement of 00l data of 1:3 samples of set 3

The measurements were performed at BM-33-C at the APS.

Table C.4: Le Bail fit and Rietveld results of 1:3 sample of set 3 annealed at 350 °C.

	Le Bail	Rietveld
Space group	$P\bar{3}m1$	
c [Å]	31.687(6)	
GU	1086(84)	
GV	-136(15)	
GW	7.3(6)	
LX	1.49(4)	
LY	0	
wRp	0.2370	0.2686
RP	0.1611	0.2733
Zero Shift [$Å^{-1}$]	0.0022(1)	
Scale		120(3)
	z	Occ
Nb	0	1
Se	0.050(2)	1
Se	0.151(2)	1
Nb	0.205(2)	1
Se	0.254(2)	1
Se3	0.3532(2)	1.120(3)
Cr1	0.4013(1)	1.120(3)
Se4	0.4483(1)	1.120(3)
Cu1	0.5	0.30*
Uios [$Å^2$*100]	24.3(6)	

Table C.5: Le Bail fit and Rietveld results of 1:3 sample of set 3 annealed at 400 °C.

	Le Bail	Rietveld
Space group	$P\bar{3}m1$	
c [Å]	31.488(6)	
GU	0	
GV	0	
GW	6.5(2)	
LX	0	
LY	15.4(6)	
wRp	0.2937	0.3580
RP	0.1897	0.2291
Zero Shift [Å^{-1}]	0.013(2)	
Scale		120(3)
	z	Occ
Nb	0	1
Se	0.0531(3)	1
Se	0.1513(3)	1
Nb	0.2047(2)	1
Se	0.2554(3)	1
Se3	0.3512(2)	1.158(5)
Cr1	0.4020(2)	1.158(5)
Se4	0.4481(2)	1.158(5)
Cu1	0.5	0.30*
Uios [Å^2*100]	16.8(7)	

C.3. Le Bail fit and Rietveld refinement of 00l data of sample 6

The measurements of sample 6 $[(Cu_xCr_ySe_z)_{0.5}]_{1+\delta}(NbSe_2)_3$ were performed at ID03-2 at the ESRF.

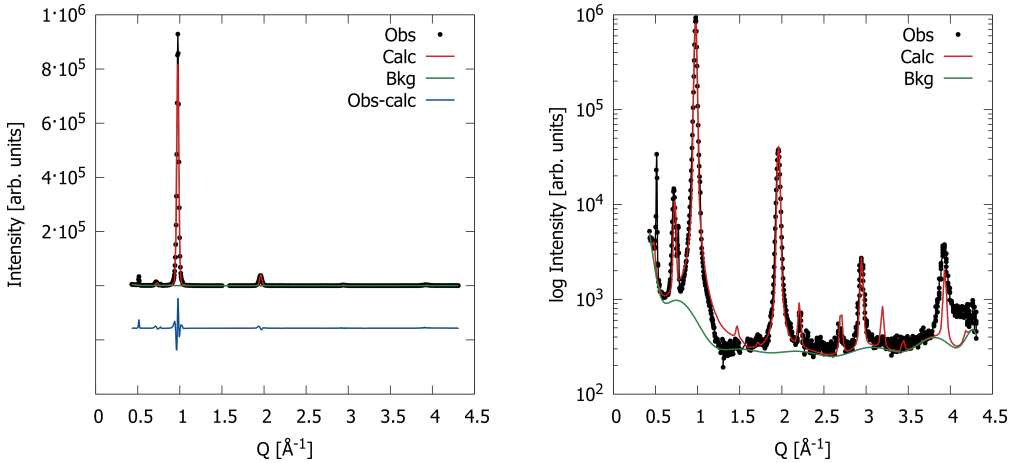

Figure C.1: X-ray diffraction patterns of sample 6 with the calculated background and difference between experimental and simulated pattern using the $CuCrSe_2$ model in linear (left) and log scale (right).

Table C.6: Le Bail fit and Rietveld results of sample 6.

	Le Bail	Rietveld
Space group	$P\bar{3}m1$	
c [Å]	24.48(3)	
GU	0	
GV	0	
GW	34.3(8)	
LX	0	
LY	42(2)	
wRp	0.2766	0.2680
RP	0.1573	0.1543
Zero Shift [$Å^{-1}$]	0.0115(6)	
Scale		4.2(9)
	z	Occ
Nb	0	1
Se	0.0320(8)	1
Se	0.220(1)	1
Nb	0.2536(8)	1
Se	0.2857(8)	1
Cu	0.3751*	0.49(4)
Se	0.470(2)	1.25(2)
Cr	0.5	1.25(2)
Uios [$Å^2$*100]	0.734*	

C.4. Le Bail fit of hk0 data of 6

The measurements were performed at ID03-2 at the ESRF.

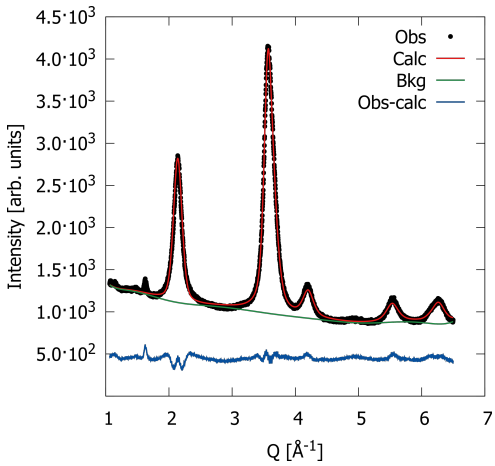

Figure C.2: X-ray diffraction pattern in in-plane geometry of sample 6 with Le Bail fit background and difference between the experimental and the simulated pattern.

Table C.7: Le bail fit results of the X-ray diffraction patterns in in-plane geometry of 6 annealed at 400 °C.

	$Cu_xCr_ySe_z$	$NbSe_2$
Space group	$R\bar{3}m$	$P\bar{3}m1$
a [Å]	7.203(6)	3.515(3)
GU	0	0
GV	0	0
GW	368(12)	634(12)
LX	0	0
LY	259(4)	329(4)
wRp	0.0241	
RP	0.0187	
Zero Shift [$Å^{-1}$]	0.076(1)	

D. $[(Cu_xCr_ySe_z)_{1+\delta}]_1[NbSe_2]_n$ ferecrystals

D.1. c-lattice parameters

All scans on set 3 were performed on BM-33-C. All scans on set 4 were performed on ID03-2.

Table D.1: Calculated c-lattice parameters of set 3 and 4.

	set 3 350 °C	set 3 400 °C	set 4
	c [Å]	c [Å]	c [Å]
1:1	18.402(2)	18.464(9)	15.1(6)
1:2	25.315(6)	25.2(1)	23.3 (1.6)
1:3	31.687(6)	31.5(1)	31.9(4)
1:4	38.21(2)	38.2(1)	38.5(5)
1:5	44.76(1)	44.4(1)	44.4(5)

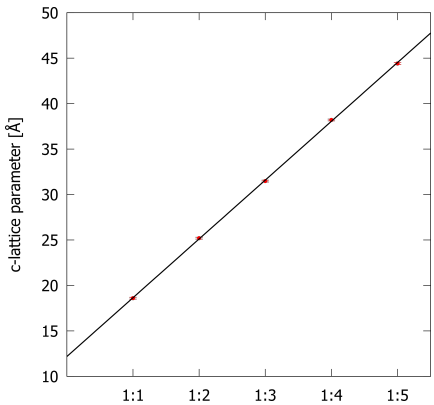

Figure D.1: Change in c-lattice parameter vs. the number of $NbSe_2$ layers of set 3 annealed at 400 °C.

The samples of set 4 have a poor crystallinity and therefor some $00l$ reflections are not visible. As the crystallinity of set 4 is inferior to set 3 a comparison of the intensity profile is pointless. There is no systematic change in the c-lattice parameter with increasing n (Figure D.2). The linear fit of the change in c-lattice parameter vs. n for $n = 3$ - 5 gives lattice parameters with rather high errors for $NbSe_2$ and $CuCr_2Se_4$ reflecting the irregular increase in c-lattice parameter. The estimated c-lattice parameter for $n = 1$ - 3 gives values that are not related to $NbSe_2$, $CuCr_2Se_4$, $CuCrSe_2$ or $CrSe_2$.

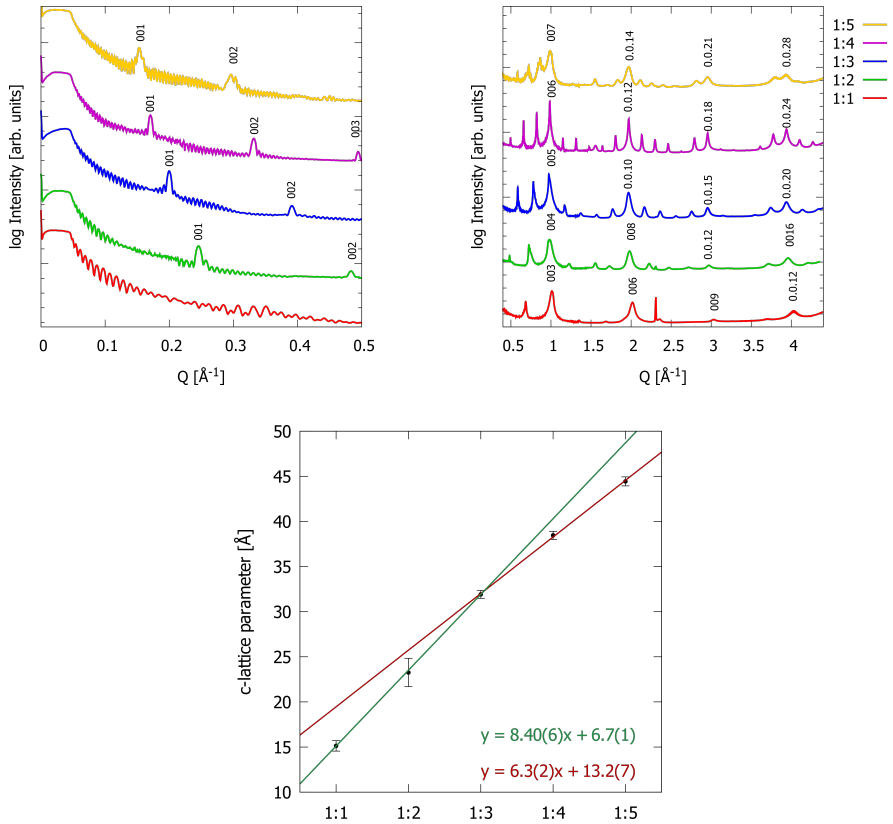

Figure D.2: Specular diffraction patterns of set 4 annealed at 400 °C in the range of 0 - 0.5 Å^{-1} and 0.4 - 4.5 Å^{-1}. The samples of annealed at 350 °C is pictured below in black. Change in c-lattice parameter vs. the number of $NbSe_2$ layers. * = sample holder

D.2. Le Bail fit of hk0 data

High-resolution X-ray diffraction scans in the ($hk0$) direction were performed. The two constituents can be indexed independently for all samples like the corresponding 1:3 samples (see chapter 5.5). The 1:1 samples $NbSe_2$ could not be considered in the LeBail fit due to low reflection intensities. Therefore the a-lattice parameters of $Cu_xCr_ySe_z$ in the 1:1 compounds might be overestimated. All sample sets show a systematic increase of the ($hk0$) reflection intensity for the $NbSe_2$ compound with increasing n. This can be clearly seen for the change of intensity for $(110)_{NbSe_2}$. By increasing the amount of $NbSe_2$ layers in the unit cell the intensity of $(110)_{NbSe_2}$ increases from a shoulder of the $(220)_{CuCr_2Se_4}$ to a distinct reflection ($n = 4$).
Besides the 1:1 and 1:5 sample of set 4, no other samples show reflections of a secondary phase as all reflection can be indexed as $NbSe_2$ or the hexagonal transformation of $CuCr_2Se_4$. The additional reflections (11) and (31) in set 4 are systematically extinct in the 3D crystal, but allowed for the 2D projection of the $CuCr_2Se_4$ structure.[99]
The a-lattice parameter of $NbSe_2$ in the ferecrystal is slightly larger than for the

bulk material (3.446 Å),[56] indicating a certain degree of copper intercalation into Cu_xNbSe_2. For comparison, $Cu_{0.667}NbSe_2$ has an a-lattice parameter of 3.487 Å.[125]

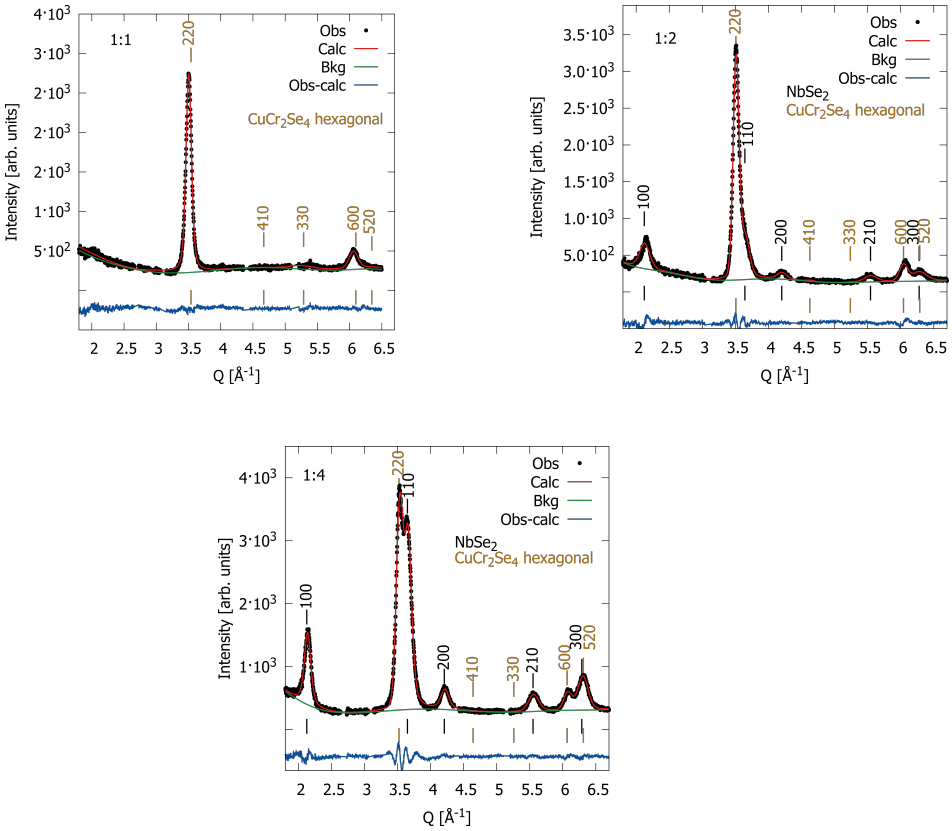

Figure D.3: X-ray diffraction patterns in in-plane geometry with Le Bail fit background and difference between experimental and simulated pattern of set 3 annealed at 400 °C.

Table D.2: Le Bail fit results of the X-ray diffraction patterns in in-plane geometry of set 3 annealed at 400 °C.

	1:1		1:2	
	$CuCr_2Se_4$	$NbSe_2$	$CuCr_2Se_4$	$NbSe_2$
Space group	$R\bar{3}m$	$P\bar{3}m1$	$R\bar{3}m$	$P\bar{3}m1$
a [Å]	7.19(1)	Not refined	7.259(9)	3.491(6)
GU	2349000(1014)	-	9926(8089)	106300(7974)
GV	-1458000(0)	-	0	-45050(3667)
GW	208300(51)	-	446(43)	6039(450)
LX	30.8(6)	-	10.6(7)	46(3)
LY	0	-	0	0
wRp	0.0613		0.0746	
RP	0.0465		0.0577	
Zero Shift [$Å^{-1}$]	0.015(4)		0.076(2)	

Table D.3: Le Bail fit results of the X-ray diffraction patterns in in-plane geometry of set 3 annealed at 400 °C.

	1:4	
	$CuCr_2Se_4$	$NbSe_2$
Space group	$R\bar{3}m$	$P\bar{3}m1$
a [Å]	7.230(6)	3.487(2)
GU	5257(604)	35940(2480)
GV	0	-10090(1042)
GW	1138(34)	1265(110)
LX	0	44.1(8)
LY	0	0
wRp	0.0511	
RP	0.0404	
Zero Shift [$Å^{-1}$]	0.085(1)	

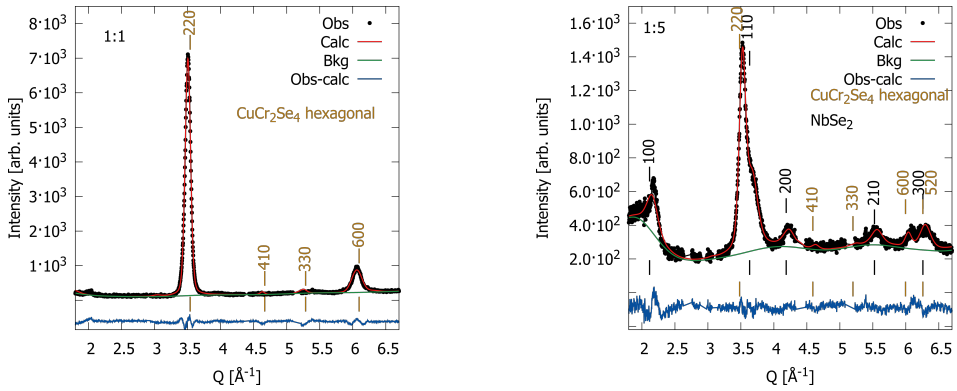

Figure D.4: X-ray diffraction patterns in in-plane geometry with Le Bail fit background and difference between experimental and simulated pattern of set 3 annealed at 350 °C.

Table D.4: Le Bail fit results of the X-ray diffraction patterns in in-plane geometry of set 3 annealed at 350 °C.

	1:1		1:5	
	$CuCr_2Se_4$	$NbSe_2$	$CuCr_2Se_4$	$NbSe_2$
Space group	$R\bar{3}m$	$P\bar{3}m1$	$R\bar{3}m$	$P\bar{3}m1$
a [Å]	7.193(9)	Not refined	7.31(2)	3.51(2)
GU	15460(10450)	-	0	0
GV	-83350(6354)	-	0	0
GW	11570(897)	-	789(49)	1814(187)
LX	16.7(4)	-	31(2)	71(4)
LY	0	-	0	0
wRp	0.1134		0.0694	
RP	0.0731		0.0527	
Zero Shift [$Å^{-1}$]	0.015(2)		0.129(4)	

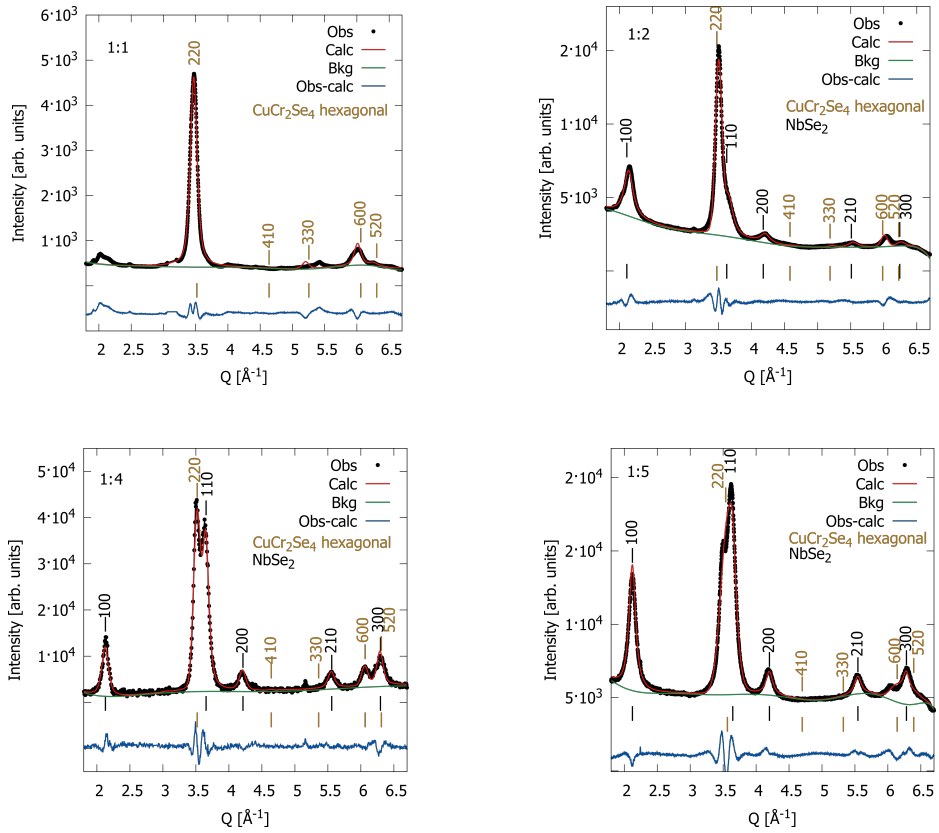

Figure D.5: X-ray diffraction patterns in in-plane geometry with Le Bail fit background and difference between experimental and simulated pattern of set 4 annealed at 400 °C.

Table D.5: Le Bail fit results of the x-ray diffraction patterns in in-plane geometry of set 4 annealed at 400 °C.

	1:1		1:2	
	$CuCr_2Se_4$	$NbSe_2$	$CuCr_2Se_4$	$NbSe_2$
Space group	$R\bar{3}m$	$P\bar{3}m1$	$R\bar{3}m$	$P\bar{3}m1$
a [Å]	7.23(1)	Not refined	7.330(9)	3.513(6)
GU	0	-	0	0
GV	0	-	0	0
GW	299(10)	-	570(4)	73(28)
LX	30.4(5)	-	0	71(1)
LY	0	-	0	0
wRp	0.0813		0.0407	
RP	0.0554		0.0298	
Zero Shift [$Å^{-1}$]	-0.003(2)		0.07(1)	

Table D.6: Le Bail fit results of the X-ray diffraction patterns in in-plane geometry of set 4 annealed at 400 °C.

	1:4		1:5	
	$CuCr_2Se_4$	$NbSe_2$	$CuCr_2Se_4$	$NbSe_2$
Space group	$R\bar{3}m$	$P\bar{3}m1$	$R\bar{3}m$	$P\bar{3}m1$
a [Å]	7.231(1)	3.482(2)	7.140(6)	3.490(3)
GU	0	0	0	0
GV	0	0	0	0
GW	1387(20)	453(52)	2390(17)	53(12)
LX	0	55(2)	0	51.2(7)
LY	0	0	0	0
wRp	0.1102		0.0323	
RP	0.0834		0.0243	
Zero Shift [$Å^{-1}$]	0.061(1)		0.0435(8)	

D.3. XRF data of 1:n data

Table D.7: Atomic % in set 3 annealed at 350 °C determined by XRF.

Sample	Cr [at %]	Cu [at %]	Nb [at %]	Se [at %]
1:1	17.122	5.230	10.890	66.528
1:2	14.369	4.064	15.892	65.455
1:3	10.588	2.933	19.249	67.002
1:4	9.431	2.542	22.111	65.690
1:5	8.085	2.188	20.542	68.931

Table D.8: Atomic % in set 3 annealed at 400 °C determined by XRF.

Sample	Cr [at %]	Cu [at %]	Nb [at %]	Se [at %]
1:1	17.425	5.624	11.219	65.501
1:2	14.662	3.961	15.436	65.716
1:3	10.829	2.932	19.870	66.130
1:4	9.549	2.516	21.875	65.832
1:5	7.889	2.358	21.370	68.149

Table D.9: Atomic % in set 4 annealed at 400 °C determined by XRF.

Sample	Cr [at %]	Cu [at %]	Nb [at %]	Se [at %]
1:1	19.538	10.324	9.752	60.110
1:2	15.719	7.219	14.713	62.159
1:3	13.443	5.941	17.555	62.928
1:4	11.655	4.734	19.976	63.579
1:5	9.425	4.539	22.547	63.461

E. Rebinning algorithm of aps slicereduce

```
subroutine does_ray_intersect(ipoint, ipA, ipB, intersect_val)
    ! Given a point, does a ray going horizontally to the right
    ! intersict with line defined by pA and pB
    ! compare with ray-casting algorithm of rosettacode.org
    implicit none
    double precision, dimension(2), intent(in) :: ipoint, ipA, ipB
    logical, intent(out) :: intersect_val
    double precision, dimension(2) :: pA, pB, point
    double precision :: m_red, m_blue
    double precision, parameter :: eps = 1d-8

    intersect_val=.FALSE.
    ! make sure B is noted as point above A
    if (ipA(2) > ipB(2)) then
        pA = ipB
        pB = ipA
    else
        pA = ipA
        pB = ipB
    endif
    point = ipoint
    ! if point y value is on exactly same height as A or B, shift it upwards
    ! (avoid ray on vertex problem)
    if (point(2) == pA(2) .OR. point(2) == pB(2)) then
        point(2) = point(2) + eps
    endif

    ! is point above or below line or right of the line?
    if (point(2) > pB(2) .OR. point(2) < pA(2) .OR. point(1) > max(pA(1), pB(1))) then
        intersect_val=.FALSE.
    else
        ! is point left of A and B (and not above and not below) -> hit
        if (point(1) < min(pA(1), pB(1))) then
            intersect_val=.TRUE.
        ! point is in between, is it left or right of it?
        else
            ! find slope of AB
            if (abs(pB(1) - pA(1)) > tiny(0.d0)) then
                m_red = (pB(2) - pA(2)) / (pB(1) - pA(1))
            else
                m_red = huge(0.d0)
            end if

            ! find slope of AP
            if (abs(point(1) - pA(1)) > tiny(0.d0)) then
                m_blue = (point(2) - pA(2)) / (point(1) - pA(1))
            else
                m_blue = huge(0.d0)
            end if

            ! if slope of AP is greater than AB, it is left and therefore it hits
            if (m_blue >= m_red) then
                intersect_val = .TRUE.
            else
                intersect_val = .FALSE.
            end if
        end if
    end if
end subroutine does_ray_intersect

subroutine point_inside_polygon(point, polygon_trail, pip, Npolygon)
    implicit none
    !Check if pip using "Ray-casting algorithm"
    ! check whether point is inside polygon defined by polygon trail
    double precision, dimension(2), intent(in) :: point
    double precision, dimension(Npolygon, 2), intent(in) :: polygon_trail
    integer, intent(in) :: Npolygon
    logical, intent(out) :: pip
```

```

    double precision, dimension(2) :: pA, pB
    integer :: ipoly, jpoly, sumval
    logical :: pipaddend

    sumval = 0
    pip = .FALSE.

    do ipoly=1, Npolygon
        jpoly = mod(ipoly+1, Npolygon+1)
        if (jpoly .EQ. 0) jpoly = 1
        pA = polygon_trail(ipoly, :)
        pB = polygon_trail(jpoly, :)
        call does_ray_intersect(point, pA, pB, pipaddend)
        if (pipaddend) sumval = sumval + 1
    end do

    if (mod(sumval, 2) == 0) then
        pip = .FALSE.
    else
        pip = .TRUE.
    end if
end subroutine point_inside_polygon

subroutine append_point_to_polygon(point, poly_in, Npoly, poly_out)
    implicit none
    double precision, dimension(2), intent(in) :: point
    double precision, dimension(Npoly, 2), intent(in) :: poly_in
    integer, intent(in) :: Npoly
    double precision, dimension(Npoly+1, 2), intent(out) :: poly_out
    integer :: i

    do i=1,Npoly
        poly_out(i,:) = poly_in(i,:)
    end do
        poly_out(Npoly+1,:) = point
end subroutine append_point_to_polygon

subroutine append_point_to_poslist(point, poslist_in, Nposlist, poslist_out)
    implicit none
    integer, dimension(2), intent(in) :: point
    integer, dimension(Nposlist, 2), intent(in) :: poslist_in
    integer, intent(in) :: Nposlist
    integer, dimension(Nposlist+1, 2), intent(out) :: poslist_out
    integer :: i

    do i=1,Nposlist
        poslist_out(i,:) = poslist_in(i,:)
    end do
        poslist_out(Nposlist+1,:) = point
end subroutine append_point_to_poslist

subroutine append_point_to_list(point, list_in, Nlist, list_out)
    implicit none
    double precision, intent(in) :: point
    double precision, dimension(Nlist), intent(in) :: list_in
    integer, intent(in) :: Nlist
    double precision, dimension(Nlist+1), intent(out) :: list_out
    integer :: i

    do i=1,Nlist
        list_out(i) = list_in(i)
    end do
        list_out(Nlist+1) = point
end subroutine append_point_to_list

subroutine check_if_vector_on_vertical_bin_edge(point, vector, bin_edge_point, binheight, crosses,
    crosspoint)
    implicit none
    double precision, dimension(2), intent(in) :: point, vector, bin_edge_point
    double precision, intent(in) :: binheight
```

```
    logical, intent(out) :: crosses
    double precision, dimension(2), intent(out) :: crosspoint

    double precision :: m, cross_y, inner_length
    crosses = .FALSE.
    crosspoint = (/-1,-1/)

    if (vector(1) /= 0) then
        m = (bin_edge_point(1) - point(1))/vector(1)
    else
        m = huge(0.d0)
    end if

    if (0 <= m .AND. m <= 1) then
        cross_y = point(2) + m*vector(2)
        inner_length = (cross_y - bin_edge_point(2))/binheight
        if (0 <= inner_length .AND. inner_length <= 1) then
            crosses = .TRUE.
            crosspoint = (/bin_edge_point(1), cross_y/)
        end if
    end if
end subroutine check_if_vector_on_vertical_bin_edge

subroutine check_if_vector_on_horizontal_bin_edge(point, vector, bin_edge_point, binwidth, crosses
    , crosspoint)
    implicit none
    double precision, dimension(2), intent(in) :: point, vector, bin_edge_point
    double precision, intent(in) :: binwidth
    logical, intent(out) :: crosses
    double precision, dimension(2), intent(out) :: crosspoint

    double precision :: m, cross_x, inner_length
    crosses = .FALSE.
    crosspoint = (/-1,-1/)

    if (vector(2) /= 0) then
        m = (bin_edge_point(2) - point(2))/vector(2)
    else
        m = huge(0.d0)
    end if

    if (0 <= m .AND. m <= 1) then
        cross_x = point(1) + m*vector(1)
        inner_length = (cross_x - bin_edge_point(1))/binwidth
        if (0 <= inner_length .AND. inner_length <= 1) then
            crosses = .TRUE.
            crosspoint = (/cross_x, bin_edge_point(2)/)
        end if
    end if
end subroutine check_if_vector_on_horizontal_bin_edge

subroutine rebin(L, input_x, input_y, input_data, input_scale, input_bin_width_x,
    input_bin_width_y,&
                output_x, output_y, Nx, Ny, Mx, My, output_data, output_scale)
    implicit none

    double precision, intent(in):: L
    double precision, intent(in), dimension(Nx) :: input_x
    double precision, intent(in), dimension(Ny) :: input_y
    double precision, intent(in), dimension(Nx, Ny) :: input_data, input_scale
    double precision, intent(in):: input_bin_width_x, input_bin_width_y
    double precision, intent(in), dimension(Mx) :: output_x
    double precision, intent(in), dimension(My) :: output_y
    integer, intent(in):: Nx, Ny, Mx, My

    double precision, intent(out), dimension(Mx, My) :: output_data, output_scale


    double precision, dimension(Mx, My) :: scale_factors
    integer:: ix, iy, jx, jy, ihelp, jhelp
    double precision :: x, y
```

```
    double precision :: dat_value, sca_value

    double precision, dimension(2) :: pA, pB, pC, pD
    double precision, dimension(2) :: rpA, rpB, rpC, rpD, bin_edge_point
    double precision, dimension(2) :: vAB, vBC, vCD, vDA
    double precision, dimension(2) :: hvector, h2vector, hpoint, h2point, h3point
    double precision, dimension(4, 2):: transformed_polygon
    double precision, dimension(4, 2):: rectangle_polygon
    double precision, dimension(:, :), allocatable :: polygon_trail, hpolygon_trail

    !for cleaning
    double precision, dimension(:, :), allocatable :: polygon_trail_cleaned
    integer :: Npoly_trail, Npoly_trail_cleaned
    logical :: point_is_double

    !for sorting
    double precision, dimension(:, :), allocatable :: points_above
    double precision, dimension(:, :), allocatable :: points_below
    integer :: num_points_above, num_points_below
    double precision, dimension(:, :), allocatable :: polygon_trail_sorted
    double precision, dimension(2) :: sort_min_point, sort_max_point
    double precision :: crossproduct
    integer :: sort_left_pos, sort_right_pos

    double precision, dimension(:), allocatable :: new_count_list, hnew_count_list
    integer, dimension(:, :), allocatable :: new_count_list_positions, hnew_count_list_positions
    integer:: number_of_new_counts


    double precision :: minx, miny, maxx, maxy
    double precision :: output_bin_width_x, output_bin_width_y, output_xmin, output_ymin
    double precision :: area_polygon, area_rectangle, overlap_area
    double precision :: rectbin_x, rectbin_y
    LOGICAL:: cf1, cf2, cf3, cf4, chelp
    double precision :: hbin_minx, hbin_maxx, hbin_miny, hbin_maxy
    integer:: bin_minx, bin_maxx, bin_miny, bin_maxy

    double precision :: current_polygon_area, triangle_area, normvalue, dot_result
    integer::sign_of_area

    double precision :: initial_total_count, final_total_count

    !output arrays are supposed to be equidistant grids!
    !rectangular pattern is put around points
    output_bin_width_x = output_x(2) - output_x(1)
    output_xmin = output_x(1) - 0.5d0*output_bin_width_x
    output_bin_width_y = output_y(2) - output_y(1)
    output_ymin = output_y(1) - 0.5d0*output_bin_width_y
    area_rectangle = output_bin_width_x*output_bin_width_y

    initial_total_count = 0d0
    do ix=1, Nx
        do iy=1, Ny
            initial_total_count  = initial_total_count + input_data(ix, iy)
        end do
    end do
    ! Initialize output arrays
    output_data = 0d0
    output_scale = 0d0
    scale_factors = 0d0

    do ix=1, Nx
        x = input_x(ix)
        do iy=1, Ny
            y = input_y(iy)
            dat_value = input_data(ix, iy)
            sca_value = input_scale(ix, iy)
            ! obtained x, y, and count + monitor value for an input point

            ! span rectangle around given point
            pA = (/x - 0.5d0*input_bin_width_x, y - 0.5d0*input_bin_width_y/)
```

```
            pB = (/x + 0.5d0*input_bin_width_x, y - 0.5d0*input_bin_width_y/)
            pC = (/x + 0.5d0*input_bin_width_x, y + 0.5d0*input_bin_width_y/)
            pD = (/x - 0.5d0*input_bin_width_x, y + 0.5d0*input_bin_width_y/)

            ! transform to quadrangle in new space
            call coordinate_transform(pA, L)
            call coordinate_transform(pB, L)
            call coordinate_transform(pC, L)
            call coordinate_transform(pD, L)

            ! save corner points in polygon list
            transformed_polygon(1, :) = pA
            transformed_polygon(2, :) = pB
            transformed_polygon(3, :) = pC
            transformed_polygon(4, :) = pD

            ! get most left, right up and down points from the four corners
            minx = min(pA(1), pB(1), pC(1), pD(1))
            maxx = max(pA(1), pB(1), pC(1), pD(1))
            miny = min(pA(2), pB(2), pC(2), pD(2))
            maxy = max(pA(2), pB(2), pC(2), pD(2))

            !get idx position of corner points in new grid
            hbin_minx = (minx - output_xmin)/output_bin_width_x
            hbin_maxx = (maxx - output_xmin)/output_bin_width_x
            hbin_miny = (miny - output_ymin)/output_bin_width_y
            hbin_maxy = (maxy - output_ymin)/output_bin_width_y

            ! Transformed Point outside of new grid? Then don't include it. Move on
            if (hbin_minx < 0 .OR. hbin_maxx < 0 .OR. &
                hbin_miny < 0 .OR. hbin_maxy < 0 .OR. &
                hbin_minx >= Mx .OR. hbin_maxx >= Mx .OR. &
                hbin_miny >= My .OR. hbin_maxy >= My) cycle

            ! to integer, remember that array counting starts with 1
            bin_minx = int(hbin_minx)+1
            bin_maxx = int(hbin_maxx)+1
            bin_miny = int(hbin_miny)+1
            bin_maxy = int(hbin_maxy)+1

            ! Is the transformed Point completly in new bin? Add and move on
            if (bin_minx == bin_maxx .AND. bin_miny == bin_maxy) then
                output_data(bin_minx, bin_miny) =&
                    output_data(bin_minx, bin_miny) + dat_value
                output_scale(bin_minx, bin_miny) =&
                    output_scale(bin_minx, bin_miny) + sca_value
                scale_factors(bin_minx, bin_miny) =&
                    scale_factors(bin_minx, bin_miny) + 1.d0
                cycle
            end if

            ! Point inside new grid and streches over multiply bins...
            ! so we will have to split it across the new bins
            area_polygon = 0d0

            if(allocated(new_count_list)) then
                deallocate(new_count_list)
            end if
            allocate(new_count_list(0))

            if(allocated(new_count_list_positions)) then
                deallocate(new_count_list_positions)
            end if
            allocate(new_count_list_positions(0,2))
            number_of_new_counts = 0

            vAB = pB - pA
            vBC = pC - pB
            vCD = pD - pC
            vDA = pA - pD

```

```
350             ! Loop over all considerable grid points in new grid
351             do jx=bin_minx, bin_maxx
352                 if (jx > Mx .OR. jx < 1) cycle
353                 rectbin_x = output_x(jx) - 0.5d0*output_bin_width_x
354                 do jy=bin_miny, bin_maxy
355                     if (jy > My .OR. jy < 1) cycle
356                     rectbin_y = output_y(jy) - 0.5d0*output_bin_width_y
357
358                     ! Current rectangle, find overlap area
359                     rpA = (/rectbin_x, rectbin_y/)
360                     rpB = (/rectbin_x + output_bin_width_x, rectbin_y/)
361                     rpC = (/rectbin_x + output_bin_width_x, rectbin_y +&
362                         output_bin_width_y/)
363                     rpD = (/rectbin_x, rectbin_y + output_bin_width_y/)
364
365                     rectangle_polygon(1, :) = rpA
366                     rectangle_polygon(2, :) = rpB
367                     rectangle_polygon(3, :) = rpC
368                     rectangle_polygon(4, :) = rpD
369
370                     ! check whether one of the four points is inside the new
371                     if(allocated(polygon_trail)) then
372                         deallocate(polygon_trail)
373                     end if
374                     allocate(polygon_trail(0,2))
375                     Npoly_trail = 0
376
377                     call point_inside_polygon(rpA, transformed_polygon, cf1, 4)
378                     if(cf1) then
379                         allocate(hpolygon_trail(Npoly_trail+1,2))
380                         call append_point_to_polygon(rpA, polygon_trail,&
381                             Npoly_trail, hpolygon_trail)
382                         call move_alloc(hpolygon_trail, polygon_trail)
383                         Npoly_trail = Npoly_trail + 1
384                     end if
385
386                     call point_inside_polygon(rpB, transformed_polygon, cf2, 4)
387                     if(cf2) then
388                         allocate(hpolygon_trail(Npoly_trail+1,2))
389                         call append_point_to_polygon(rpB, polygon_trail,&
390                             Npoly_trail, hpolygon_trail)
391                         call move_alloc(hpolygon_trail, polygon_trail)
392                         Npoly_trail = Npoly_trail + 1
393                     end if
394
395                     call point_inside_polygon(rpC, transformed_polygon, cf3, 4)
396                     if(cf3) then
397                         allocate(hpolygon_trail(Npoly_trail+1,2))
398                         call append_point_to_polygon(rpC, polygon_trail,&
399                             Npoly_trail, hpolygon_trail)
400                         call move_alloc(hpolygon_trail, polygon_trail)
401                         Npoly_trail = Npoly_trail + 1
402                     end if
403
404                     call point_inside_polygon(rpD, transformed_polygon, cf4, 4)
405                     if(cf4) then
406                         allocate(hpolygon_trail(Npoly_trail+1,2))
407                         call append_point_to_polygon(rpD, polygon_trail,&
408                             Npoly_trail, hpolygon_trail)
409                         call move_alloc(hpolygon_trail, polygon_trail)
410                         Npoly_trail = Npoly_trail + 1
411                     end if
412
413                     ! All four points inside the new polygon? easy case
414                     ! Fraction of area count fills grid point completly
415                     if (cf1 .AND. cf2 .AND. cf3 .AND. cf4) then
416                         area_polygon = area_polygon + area_rectangle
417                         allocate(hnew_count_list(number_of_new_counts+1))
418                         allocate(hnew_count_list_positions(number_of_new_counts+1,2))
419
420                         call append_point_to_list(area_rectangle,&
```

```
                        new_count_list, number_of_new_counts, hnew_count_list)
                    call append_point_to_poslist((/jx, jy/),&
                        new_count_list_positions, number_of_new_counts,&
                        hnew_count_list_positions)
                    call move_alloc(hnew_count_list, new_count_list)
                    call move_alloc(hnew_count_list_positions, new_count_list_positions)
                    number_of_new_counts = number_of_new_counts + 1
                    cycle ! back to the top
                end if

                ! Not the case
                ! check whether edge points of polygon are inside the investigated rectangle
                call point_inside_polygon(pA, rectangle_polygon, chelp, 4)
                if (chelp) then
                    allocate(hpolygon_trail(Npoly_trail+1,2))
                    call append_point_to_polygon(pA, polygon_trail,&
                        Npoly_trail, hpolygon_trail)
                    call move_alloc(hpolygon_trail, polygon_trail)
                    Npoly_trail = Npoly_trail + 1
                end if

                call point_inside_polygon(pB, rectangle_polygon, chelp, 4)
                if (chelp) then
                    allocate(hpolygon_trail(Npoly_trail+1,2))
                    call append_point_to_polygon(pB, polygon_trail,&
                        Npoly_trail, hpolygon_trail)
                    call move_alloc(hpolygon_trail, polygon_trail)
                    Npoly_trail = Npoly_trail + 1
                end if

                call point_inside_polygon(pC, rectangle_polygon, chelp, 4)
                if (chelp) then
                    allocate(hpolygon_trail(Npoly_trail+1,2))
                    call append_point_to_polygon(pC, polygon_trail,&
                        Npoly_trail, hpolygon_trail)
                    call move_alloc(hpolygon_trail, polygon_trail)
                    Npoly_trail = Npoly_trail + 1
                end if

                call point_inside_polygon(pD, rectangle_polygon, chelp, 4)
                if (chelp) then
                    allocate(hpolygon_trail(Npoly_trail+1,2))
                    call append_point_to_polygon(pD, polygon_trail,&
                        Npoly_trail, hpolygon_trail)
                    call move_alloc(hpolygon_trail, polygon_trail)
                    Npoly_trail = Npoly_trail + 1
                end if

                ! check whether edge lines of polygon cross rectangle edges
                bin_edge_point = (/rectbin_x, rectbin_y/)

                !pA, vAB
                call check_if_vector_on_horizontal_bin_edge(pA, vAB, bin_edge_point,&
                    output_bin_width_x, chelp, hpoint)
                if (chelp) then
                    allocate(hpolygon_trail(Npoly_trail+1,2))
                    call append_point_to_polygon(hpoint, polygon_trail,&
                        Npoly_trail, hpolygon_trail)
                    call move_alloc(hpolygon_trail, polygon_trail)
                    Npoly_trail = Npoly_trail + 1
                end if

                call check_if_vector_on_horizontal_bin_edge(pA, vAB, bin_edge_point+(/0d0,
    output_bin_width_y/),&
                    output_bin_width_x, chelp, hpoint)
                if (chelp) then
                    allocate(hpolygon_trail(Npoly_trail+1,2))
                    call append_point_to_polygon(hpoint, polygon_trail,&
                        Npoly_trail, hpolygon_trail)
                    call move_alloc(hpolygon_trail, polygon_trail)
                    Npoly_trail = Npoly_trail + 1
```

```
                    end if

                    call check_if_vector_on_vertical_bin_edge(pA, vAB, bin_edge_point, &
                        output_bin_width_y, chelp, hpoint)
                    if (chelp) then
                        allocate(hpolygon_trail(Npoly_trail+1,2))
                        call append_point_to_polygon(hpoint, polygon_trail,&
                            Npoly_trail, hpolygon_trail)
                        call move_alloc(hpolygon_trail, polygon_trail)
                        Npoly_trail = Npoly_trail + 1
                    end if

                    call check_if_vector_on_vertical_bin_edge(pA, vAB, bin_edge_point+(/output_bin_width_x, 0d0/),&
                        output_bin_width_y, chelp, hpoint)
                    if (chelp) then
                        allocate(hpolygon_trail(Npoly_trail+1,2))
                        call append_point_to_polygon(hpoint, polygon_trail,&
                            Npoly_trail, hpolygon_trail)
                        call move_alloc(hpolygon_trail, polygon_trail)
                        Npoly_trail = Npoly_trail + 1
                    end if

                    !pB, vBC
                    call check_if_vector_on_horizontal_bin_edge(pB, vBC, bin_edge_point,&
                        output_bin_width_x, chelp, hpoint)
                    if (chelp) then
                        allocate(hpolygon_trail(Npoly_trail+1,2))
                        call append_point_to_polygon(hpoint, polygon_trail,&
                            Npoly_trail, hpolygon_trail)
                        call move_alloc(hpolygon_trail, polygon_trail)
                        Npoly_trail = Npoly_trail + 1
                    end if

                    call check_if_vector_on_horizontal_bin_edge(pB, vBC, bin_edge_point+(/0d0, output_bin_width_y/),&
                        output_bin_width_x, chelp, hpoint)
                    if (chelp) then
                        allocate(hpolygon_trail(Npoly_trail+1,2))
                        call append_point_to_polygon(hpoint, polygon_trail,&
                            Npoly_trail, hpolygon_trail)
                        call move_alloc(hpolygon_trail, polygon_trail)
                        Npoly_trail = Npoly_trail + 1
                    end if

                    call check_if_vector_on_vertical_bin_edge(pB, vBC, bin_edge_point, &
                        output_bin_width_y, chelp, hpoint)
                    if (chelp) then
                        allocate(hpolygon_trail(Npoly_trail+1,2))
                        call append_point_to_polygon(hpoint, polygon_trail,&
                            Npoly_trail, hpolygon_trail)
                        call move_alloc(hpolygon_trail, polygon_trail)
                        Npoly_trail = Npoly_trail + 1
                    end if

                    call check_if_vector_on_vertical_bin_edge(pB, vBC, bin_edge_point+(/output_bin_width_x, 0d0/),&
                        output_bin_width_y, chelp, hpoint)
                    if (chelp) then
                        allocate(hpolygon_trail(Npoly_trail+1,2))
                        call append_point_to_polygon(hpoint, polygon_trail,&
                            Npoly_trail, hpolygon_trail)
                        call move_alloc(hpolygon_trail, polygon_trail)
                        Npoly_trail = Npoly_trail + 1
                    end if

                    !pC, vCD
                    call check_if_vector_on_horizontal_bin_edge(pC, vCD, bin_edge_point,&
                        output_bin_width_x, chelp, hpoint)
                    if (chelp) then
                        allocate(hpolygon_trail(Npoly_trail+1,2))
```

```
                        call append_point_to_polygon(hpoint, polygon_trail,&
                            Npoly_trail, hpolygon_trail)
                        call move_alloc(hpolygon_trail, polygon_trail)
                        Npoly_trail = Npoly_trail + 1
                    end if

                    call check_if_vector_on_horizontal_bin_edge(pC, vCD, bin_edge_point+(/0d0, output_bin_width_y/),&
                        output_bin_width_x, chelp, hpoint)
                    if (chelp) then
                        allocate(hpolygon_trail(Npoly_trail+1,2))
                        call append_point_to_polygon(hpoint, polygon_trail,&
                            Npoly_trail, hpolygon_trail)
                        call move_alloc(hpolygon_trail, polygon_trail)
                        Npoly_trail = Npoly_trail + 1
                    end if

                    call check_if_vector_on_vertical_bin_edge(pC, vCD, bin_edge_point, &
                        output_bin_width_y, chelp, hpoint)
                    if (chelp) then
                        allocate(hpolygon_trail(Npoly_trail+1,2))
                        call append_point_to_polygon(hpoint, polygon_trail,&
                            Npoly_trail, hpolygon_trail)
                        call move_alloc(hpolygon_trail, polygon_trail)
                        Npoly_trail = Npoly_trail + 1
                    end if

                    call check_if_vector_on_vertical_bin_edge(pC, vCD, bin_edge_point+(/output_bin_width_x, 0d0/),&
                        output_bin_width_y, chelp, hpoint)
                    if (chelp) then
                        allocate(hpolygon_trail(Npoly_trail+1,2))
                        call append_point_to_polygon(hpoint, polygon_trail,&
                            Npoly_trail, hpolygon_trail)
                        call move_alloc(hpolygon_trail, polygon_trail)
                        Npoly_trail = Npoly_trail + 1
                    end if

                    !pD, vDA
                    call check_if_vector_on_horizontal_bin_edge(pD, vDA, bin_edge_point,&
                        output_bin_width_x, chelp, hpoint)
                    if (chelp) then
                        allocate(hpolygon_trail(Npoly_trail+1,2))
                        call append_point_to_polygon(hpoint, polygon_trail,&
                            Npoly_trail, hpolygon_trail)
                        call move_alloc(hpolygon_trail, polygon_trail)
                        Npoly_trail = Npoly_trail + 1
                    end if

                    call check_if_vector_on_horizontal_bin_edge(pD, vDA, bin_edge_point+(/0d0, output_bin_width_y/),&
                        output_bin_width_x, chelp, hpoint)
                    if (chelp) then
                        allocate(hpolygon_trail(Npoly_trail+1,2))
                        call append_point_to_polygon(hpoint, polygon_trail,&
                            Npoly_trail, hpolygon_trail)
                        call move_alloc(hpolygon_trail, polygon_trail)
                        Npoly_trail = Npoly_trail + 1
                    end if

                    call check_if_vector_on_vertical_bin_edge(pD, vDA, bin_edge_point, &
                        output_bin_width_y, chelp, hpoint)
                    if (chelp) then
                        allocate(hpolygon_trail(Npoly_trail+1,2))
                        call append_point_to_polygon(hpoint, polygon_trail,&
                            Npoly_trail, hpolygon_trail)
                        call move_alloc(hpolygon_trail, polygon_trail)
                        Npoly_trail = Npoly_trail + 1
                    end if

```

```
                    call check_if_vector_on_vertical_bin_edge(pD, vDA, bin_edge_point+(/
output_bin_width_x , 0d0/),&
                        output_bin_width_y , chelp , hpoint)
                    if (chelp) then
                        allocate(hpolygon_trail(Npoly_trail+1,2))
                        call append_point_to_polygon(hpoint , polygon_trail,&
                            Npoly_trail , hpolygon_trail)
                        call move_alloc(hpolygon_trail , polygon_trail)
                        Npoly_trail = Npoly_trail + 1
                    end if


                    if (Npoly_trail >= 3) then
                        !clean double points
                        allocate(hpolygon_trail(Npoly_trail,2))
                        hpolygon_trail(1, :) = polygon_trail(1, :)
                        Npoly_trail_cleaned = 1

                        do ihelp=2, Npoly_trail
                            point_is_double = .FALSE.
                            do jhelp=1, Npoly_trail_cleaned
                                if(polygon_trail(ihelp , 1) == hpolygon_trail(jhelp , 1) .AND.&
                                        polygon_trail(ihelp , 2) == hpolygon_trail(jhelp , 2)) then
                                    point_is_double = .TRUE.
                                    exit
                                end if
                            end do

                            if (.NOT. point_is_double) then
                                Npoly_trail_cleaned = Npoly_trail_cleaned + 1
                                hpolygon_trail(Npoly_trail_cleaned , :) = polygon_trail(ihelp , :)
                            end if
                        end do

                        if(allocated(polygon_trail_cleaned)) then
                            deallocate(polygon_trail_cleaned)
                        end if
                        allocate(polygon_trail_cleaned(Npoly_trail_cleaned , 2))
                        do ihelp=1, Npoly_trail_cleaned
                            polygon_trail_cleaned(ihelp , :) = hpolygon_trail(ihelp , :)
                        end do
                        deallocate(hpolygon_trail)

                        if (Npoly_trail_cleaned >= 3) then
                            !sort the polygon
                            sort_min_point = (/huge(0d0), huge(0d0)/)
                            sort_max_point = (/-huge(0d0), -huge(0d0)/)
                            sort_left_pos = -1
                            sort_right_pos = -1

                            !find point that is most left and most right
                            do jhelp=1, Npoly_trail_cleaned
                                hpoint = polygon_trail_cleaned(jhelp , :)
                                if (hpoint(1) < sort_min_point(1)) then
                                    sort_min_point = hpoint
                                    sort_left_pos = jhelp
                                else
                                    if (hpoint(1) == sort_min_point(1) .AND.&
                                        hpoint(2) < sort_min_point(2)) then
                                        sort_min_point = hpoint
                                        sort_left_pos = jhelp
                                    end if
                                end if

                                if (hpoint(1) > sort_max_point(1)) then
                                    sort_max_point = hpoint
                                    sort_right_pos = jhelp
                                else
                                    if (hpoint(1) == sort_max_point(1) .AND.&
                                        hpoint(2) > sort_max_point(2)) then
                                        sort_max_point = hpoint
```

```
                                    sort_right_pos = jhelp
                                end end if
                            end if
                        end do

                        num_points_above = 0
                        if(allocated(points_above)) then
                            deallocate(points_above)
                        end if
                        allocate(points_above(num_points_above,2))
                        num_points_below = 0
                        if(allocated(points_below)) then
                            deallocate(points_below)
                        end if
                        allocate(points_below(num_points_below,2))

                        hvector = sort_max_point - sort_min_point
                        !sort into points above and below min-max connection line
                        do jhelp=1, Npoly_trail_cleaned
                            if (jhelp == sort_left_pos .OR. jhelp == sort_right_pos) cycle

                            hpoint = polygon_trail_cleaned(jhelp, :) - sort_min_point
                            crossproduct = hvector(1)*hpoint(2) - hvector(2)*hpoint(1)
                            if (crossproduct >= 0) then
                                allocate(hpolygon_trail(num_points_above+1,2))
                                call append_point_to_polygon(polygon_trail_cleaned(jhelp, :),&
                                    points_above, num_points_above, hpolygon_trail)
                                call move_alloc(hpolygon_trail, points_above)
                                num_points_above = num_points_above + 1
                            else
                                allocate(hpolygon_trail(num_points_below+1,2))
                                call append_point_to_polygon(polygon_trail_cleaned(jhelp, :),&
                                    points_below, num_points_below, hpolygon_trail)
                                call move_alloc(hpolygon_trail, points_below)
                                num_points_below = num_points_below + 1
                            end if
                        end do

                        ! sort points above connecting line
                        do ihelp=2, num_points_above
                            jhelp = ihelp - 1
                            hpoint = points_above(ihelp, :)
                            do while(jhelp>=1 .AND. points_above(jhelp, 1) > hpoint(1))
                                points_above(jhelp+1,:) = points_above(jhelp,:)
                                jhelp = jhelp - 1
                            end do
                            points_above(jhelp+1,:) = hpoint
                        end do

                        ! sort points below connecting line
                        do ihelp=2, num_points_below
                            jhelp = ihelp - 1
                            hpoint = points_below(ihelp, :)
                            do while(jhelp>=1 .AND. points_below(jhelp, 1) > hpoint(1))
                                points_below(jhelp+1,:) = points_below(jhelp,:)
                                jhelp = jhelp - 1
                            end do
                            points_below(jhelp+1,:) = hpoint
                        end do

                        ! fill into sorted polygon
                        if(allocated(polygon_trail_sorted)) then
                            deallocate(polygon_trail_sorted)
                        end if
                        allocate(polygon_trail_sorted(Npoly_trail_cleaned,2))

                        polygon_trail_sorted(1, :) = sort_min_point
                        do ihelp=1, num_points_below
                            polygon_trail_sorted(1+ihelp,:) = points_below(ihelp,:)
                        end do
                        polygon_trail_sorted(num_points_below+2, :) = sort_max_point
```

```
                                do ihelp=1, num_points_above
                                    polygon_trail_sorted(ihelp+num_points_below+2, :) =&
                                        points_above(num_points_above- (ihelp-1), :)
                                end do

                                current_polygon_area = 0d0
                                do ihelp=1, Npoly_trail_cleaned
                                    jhelp = mod((ihelp+1), Npoly_trail_cleaned+1)
                                    if (jhelp .EQ. 0) jhelp = 1
                                    hpoint = polygon_trail_sorted(ihelp, :)
                                    h2point = polygon_trail_sorted(jhelp, :)
                                    hvector = h2point - hpoint
                                    triangle_area = abs(hpoint(1)*h2point(2) - hpoint(2)*h2point(1))

                                    normvalue = sqrt(hvector(1)**2 + hvector(2)**2)
                                    h2vector(1) = -hvector(2)/normvalue
                                    h2vector(2) = hvector(1)/normvalue

                                    h3point = hpoint + 0.5d0*hvector + h2vector
                                    call point_inside_polygon(h3point, &
                                        polygon_trail_sorted, chelp, Npoly_trail_cleaned)
                                    if (chelp) then
                                        h2vector = -1d0*h2vector
                                    end if

                                    dot_result = hpoint(1)*h2vector(1) + hpoint(2)*h2vector(2)
                                    if (dot_result >= 0) then
                                        sign_of_area = 1
                                    else
                                        sign_of_area = -1
                                    end if
                                    triangle_area = triangle_area * sign_of_area
                                    current_polygon_area = current_polygon_area + triangle_area
                                end do
                                overlap_area = abs(current_polygon_area)/2.
                            else
                                overlap_area = 0d0
                            end if

                            !call calc_area_of_polygon(polygon_trail, Npoly_trail, overlap_area)
                            area_polygon = area_polygon + overlap_area

                            allocate(hnew_count_list(number_of_new_counts+1))
                            allocate(hnew_count_list_positions(number_of_new_counts+1,2))
                            call append_point_to_list(overlap_area,&
                                new_count_list, number_of_new_counts, hnew_count_list)
                            call append_point_to_poslist((/jx, jy/),&
                                new_count_list_positions, number_of_new_counts,&
                                hnew_count_list_positions)
                            call move_alloc(hnew_count_list, new_count_list)
                            call move_alloc(hnew_count_list_positions, new_count_list_positions)
                            number_of_new_counts = number_of_new_counts + 1
                        end if
                    end do
                end do

                do ihelp=1, number_of_new_counts
!                    if (area_polygon > 100) print*,overlap_area,area_polygon
                    jx = new_count_list_positions(ihelp, 1)
                    jy = new_count_list_positions(ihelp, 2)
                    overlap_area = new_count_list(ihelp)
                    output_data(jx, jy) = output_data(jx, jy) + dat_value*overlap_area/area_polygon
                    output_scale(jx, jy) = output_scale(jx, jy) + sca_value*overlap_area/area_polygon
                    scale_factors(jx, jy) = scale_factors(jx, jy) + overlap_area/area_polygon
                end do
            end do
        end do

        final_total_count = 0d0
        do ix=1, Mx
            do iy=1, My
```

```
            final_total_count = final_total_count + output_data(ix, iy)
            sca_value = scale_factors(ix, iy)
            if (sca_value > 0) then
                output_scale(ix, iy) = output_scale(ix, iy)/sca_value
            end if
        end do
    end do
end subroutine rebin
```

F. Abbreviations

$A_{\text{Si wafer}}$	Sample area [cm^2]
Å	Angström; 1 Å = 10^{-10} m
ad	As deposited
B	Applied Field [T]
b	Scattering length of atom
C	Curie constant [K]
d	Layer thickness [Å]
d	Film thickness
D	Coherence length [Å]
d_{min}	Thickness of sublayers
d_N	Material thickness
CDW	Charge density wave
EDX	Energy dispersive X-ray spectroscopy
emu	Electromagnetic unit; 1 emu = 10^{-3} Am^2
eV	Electron Volt
Få	Fåkeström
FC	Field cooled
FCW	Field cooled warming
FWHM	Full width at half maximum
H	Magnetic field [Oe]
h_{film}	Film thickness [cm]
h_{wafer}	Wafer thickness [cm]
HAADF	High-angle annular dark-field imaging
k_B	Boltzmann constant $1.380\,648\,52(79) \cdot 10^{-23}$ JK^{-1}
$\vec{k_i}$	Incident ray
$\vec{k_r}$	Reflected ray
m_i	Diffraction order of i-th maximum
M	Molecular weight
M	Magnetic moment [emu]
M	(Volume) magnetization [A/m]
MER	Modulated elemental reactants
MLC	Misfit layer compound
MPMS	Magnetic property measurement system
N	Amount of layer

n	Refractive index
N_A	Avogadro constant $6.022\,140\,857(74)\cdot 10^{23}\,\mathrm{mol}^{-P1}$
NBED	Nano-beam electron diffraction
NMR	Nuclear magnetic resonance
M_S	Saturation magnetization [A/m]
m_{sample}	Sample mass [g]
Oe	Oersted; $1\,\mathrm{Oe} = \frac{10^3}{4\pi}$ A/m
PLD	Pulsed laser deposition
PNP	Polarized neutron reflectometry
PPMS	Physical property measurement system
PVD	Physical vapour deposition
$\vec{Q}_z$	Scattering vector
r	Reflectivity
r'	Fresnel coefficient
r_e	Electron radius $2.187\,940\,322\,7(19)\cdot 10^{-15}\,\mathrm{m}$
SLD	Scattering length density
STEM	Scanning transmission electron microscope
SQUID	Superconducting quantum interference device
T	Temperature [K] or [°C]
T_C	Superconducting transition temperature [K]
T_C	Curie temperature [K]
T_N	Néel temperature [K]
TEM	Transmission electron microscope
TMD	Transition metal dichalcogenide
V_m	Material volume
V_{sample}	Sample volume [cm^3]
VSM	Vibrating sample magnetometry
XRD	X-ray diffraction
XRF	X-ray fluorescence
XRR	X-ray reflectometry
Z	Thomson scattering
ZFC	Zero field cooled
β	Absorptive dispersion correction
δ	Misfit parameter
δ	Anomalous dispersion correction
$\Delta b'$	Lattice mismatch [Å]

ΔQ	Unidirectional lattice mismatch [Å^{-1}]
ΔQ	Separation of the Kiessig Fring maxima [Å^{-1}]
$\Delta\mu$	Distance between the Gaussian maxima [Å^{-1}]
η	Amount of substance
2θ	Scattering angle [°]
θ_i	Angular position of Kiessig fringes [°]
θ_c	Angular position of critical angle [°]
θ_W	Curie-Weiss temperature [K]
λ	Wavelength [Å]
μ	Integral particle moment
μ_B	Bohr magneton = $9.274\,009\,994(57) * 10^{-24}$ JT^{-1}
ρ	Density [g/cm^3]
χ	Susceptibility
χ^2	Goodness of fit
χ_D	Diamagnetic susceptibility
ρ_D	Density [g/cm^3]
ρ_e	Electron density
ω	Diffracted beam direction

References

[1] T. G. H. James, *Gold Bull.* **1972**, *5*(2), 38–42.

[2] E. Bloch, Transparent Mirror, **1903**.

[3] H. Frey, H. R. Khan, *Handbook of Thin-Film Technology*, Springer Berlin Heidelberg, Berlin, Heidelberg, **2015**.

[4] A. H. Lettington, *Carbon* **1998**, *36*(5-6), 555–560.

[5] T. A. Otitoju, A. L. Ahmad, B. S. Ooi, *J. Ind. Eng. Chem.* **2017**, *47*, 19–40.

[6] F. Samson, *Surf. Coat. Technol.* **1996**, *81*(1), 79–86.

[7] J. Azadmanjiri, C. C. Berndt, J. Wang, A. Kapoor, V. K. Srivastava, *RSC Adv.* **2016**, *6*(111), 109361–109385.

[8] F. Siewert, J. Buchheim, T. Zeschke, M. Störmer, G. Falkenberg, R. Sankari, *J. Synchrotron Radiat.* **2014**, *21*(5), 968–975.

[9] X. Cheng, L. Zhang, C. Morawe, M. Sanchez Del Rio, *J. Synchrotron Radiat.* **2015**, *22*(2), 317–327.

[10] B. Tudu, A. Tiwari, *Vacuum* **2017**, *146*, 329–341.

[11] D. Richardson, K. Srinivasan, S. Katz, M. Wu, *Appl. Phys. Lett.* **2017**, *111*(18).

[12] A. Kingon, *Nature* **1999**, *401*(6754), 658–659.

[13] Z. Su, M. Yao, M. Li, W. Gao, Q. Li, Q. Feng, X. Yao, *J. Mater. Chem. C* **2018**, *6*(21), 5616–5623.

[14] A. Pearse, T. Schmitt, E. Sahadeo, D. M. Stewart, A. Kozen, K. Gerasopoulos, A. A. Talin, S. B. Lee, G. W. Rubloff, K. E. Gregorczyk, *ACS Nano* **2018**, *12*(5), 4286–4294.

[15] J. H. Choi, Y. M. Kim, Y. W. Park, T. H. Park, J. W. Jeong, H. J. Choi, E. H. Song, J. W. Lee, C. H. Kim, B. K. Ju, *Nanotechnology* **2010**, *21*(47).

[16] J. Meyer, H. Schmidt, W. Kowalsky, T. Riedl, A. Kahn, *App. Phys. Lett.* **2010**, *96*(24), 1–4.

[17] S. H. Lim, S. W. Seo, H. Lee, H. Chae, S. M. Cho, *Korean J. Chem. Eng.* **2016**, *33*(6), 1971–1976.

[18] Y. Zhang, J. Hao, *J. Mater. Chem. C* **2013**, *1*(36), 5607.

[19] F. M. Koehler, M. Rossier, M. Waelle, E. K. Athanassiou, L. K. Limbach, R. N. Grass, D. Günther, W. J. Stark, *Chem. commun.* **2009**, 4862–4864.

[20] S. D. Bader, *Rev. Mod. Phys.* **2006**, *78*, 1–15.

[21] A.-H. Lu, E. L. Salabas, F. Schüth, *Angew. Chem. Int. Ed* **2007**, *46*, 1222–1244.

[22] M. Wankhede, A. Bouras, M. Kaluzova, C. G. Hadjipanayis, *Expert Rev Clin Pharmacol.* **2012**, *5*(2), 173–186.

[23] S. Disch, E. Wetterskog, R. P. Hermann, A. Wiedenmann, U. Vainio, G. Salazar-Alvarez, L. Bergström, T. Brückel, *New J. Phys.* **2012**, *14*, 0130205–0130216.

[24] Eds., J. Li, J. Li, Y. Chu, *Crystal Growth - Concepts, Machanisms and Applications*, nova Science Publisher, New York, **2015**, 1–345.

[25] L. Fister, X. Li, J. McConnell, T. Novet, D. C. Johnson, *J. Vac. Sci. Technol. A* **1993**, *11*(6), 3014–3019.

[26] D. C. Johnson, *Curr. Opin. Solid State Mater. Sci.* **1998**, *3*, 159–167.

[27] R. Westover, R. A. Atkins, M. Falmbigl, J. J. Ditto, D. C. Johnson, *J. Solid State Chem.* **2016**, *236*, 173–185.

[28] M. Esters, M. B. Alemayehu, Z. Jones, N. T. Nguyen, M. D. Anderson, C. Grosse, S. F. Fischer, D. C. Johnson, *Angew. Chem. Int. Ed* **2015**, *127*, 1146–1150.

[29] G. Hautier, C. Fischer, V. Ehrlacher, A. Jain, G. Ceder, *Inorg. Chem.* **2011**, *50*(17), 656–663.

[30] W. Sun, S. T. Dacek, S. P. Ong, G. Hautier, A. Jain, W. D. Richards, A. C. Gamst, K. A. Persson, G. Ceder, *Sci. Adv.* **2016**, *2*, 1–8.

[31] R. Atkins, D. B. Moore, D. C. Johnson, *Chem. Mater.* **2013**, *25*, 1744–1750.

[32] M. B. Alemayehu, M. Falmbigl, C. Grosse, K. Ta, S. F. Fischer, D. C. Johnson, *J. Alloys Compd.* **2015**, *619*, 861–868.

[33] I. Häusler, R. Atkins, M. Falmbigl, S. P. Rudin, W. Neumann, D. C. Johnson, *Z. Kristallogr.* **2015**, *230*(1), 45–54.

[34] G. A. Wiegers, *Prog. Solid St. Chem.* **1996**, *24*(1-2), 1–139.

[35] J. Wulff, A. Meetsma, S. Van Smaalen, R. J. Haange, J. L. De Boer, G. A. Wiegers, *J. Solid State Chem.* **1990**, *84*(1), 118–129.

[36] A. Meerschaut, Y. Moëlo, L. Cario, A. Lafond, C. Deudon, *Mol. Cryst. Liq. Cryst. Sci. Technol., Sect. A* **2000**, *341*(2), 1–8.

[37] J. Brandt, L. Kipp, M. Skibowski, E. E. Krasovskii, W. Schattke, E. Spiecker, C. Dieker, W. Jäger, *Surf. Sci.* **2003**, *532-535*, 705–710.

[38] G. Radovsky, R. Popovitz-Biro, T. Lorenz, J.-O. Joswig, G. Seifert, L. Houben, R. E. Dunin-Borkowski, R. Tenne, *J. Mater. Chem. C* **2016**, *4*, 89.

[39] J. Rouxel, A. Meerschaut, G. A. Wiegers, *J. Alloys Compd.* **1995**, *229*(1), 144–157.

[40] C. M. Fang, A. R. H. . F. Ettema, C. Haas, G. A. Wiegers, *Phys. Rev. B* **1995**, *52*(4), 2336–2347.

[41] A. R. H. . F. Ettema, C. Haas, *J. Phys.: Condens. Matter* **1993**, *5*, 3817–3826.

[42] E. Kabliman, P. Blaha, K. Schwarz, *Phys. Rev. B* **2010**, *82*(12), 1–8.

[43] D. Merrill, D. Moore, S. Bauers, M. Falmbigl, D. Johnson, *Materials* **2015**, *8*(4), 2000–2029.

[44] C. Heideman, N. Nyugen, J. Hanni, Q. Lin, S. Duncombe, D. C. Johnson, P. Zschack, *J. Solid State Chem.* **2008**, *181*(7), 1701–1706.

[45] M. Beekman, S. Disch, S. Rouvimov, D. Kasinathan, K. Koepernik, H. Rosner, P. Zschack, W. S. Neumann, D. C. Johnson, *Angew. Chem. Int. Ed* **2013**, *52*(50), 13211–13214.

[46] M. D. Anderson, Dissertation, University of Oregon, **2011**.

[47] M. Falmbigl, M. Esters, D. C. Johnson, *Cryst. Res. Technol.* **2017**, *52*(10), 1700067.

[48] M. D. Hornbostel, E. J. Hyer, J. Thiel, D. C. Johnson, *J. Am. Chem. Soc.* **1997**, *119*(11), 2665–2668.

[49] M. Beekman, G. Cogburn, C. Heideman, S. Rouvimov, P. Zschack, W. Neumann, D. Johnson, *J. Electron. Mater.* **2012**, *41*(6), 1476–1480.

[50] D. R. Merrill, D. R. Sutherland, J. J. Ditto, D. B. Moore, M. Falmbigl, D. L. Medlin, D. C. Johnson, *Nanoscale* **2016**, *8*(28), 13646–13651.

[51] R. D. Westover, G. Mitchson, J. J. Ditto, D. C. Johnson, *Eur. J. Inorg. Chem.* **2016**, *2016*(8), 1225–1231.

[52] M. Falmbigl, Z. Hay, J. Ditto, G. Mitchson, D. C. Johnson, *J. Mater. Chem. C* **2015**, *3*(47), 12308–12315.

[53] R. D. Westover, G. Mitchson, O. K. Hite, K. Hill, D. C. Johnson, *J. Electron. Mater.* **2016**, *45*(10), 4898–4902.

[54] S. R. Wood, D. R. Merrill, G. Mitchson, A. C. Lygo, S. R. Bauers, D. M. Hamann, D. R. Sutherland, J. Ditto, D. C. Johnson, *Chem. Mater.* **2017**, *29*, 773–779.

[55] G. Mitchson, S. R. Bauers, P. Schädlich, J. J. Ditto, D. C. Johnson, *Eur. J. Inorg. Chem.* **2016**, 950–957.

[56] I. Okońska-Kozlowska, J. Kopyczok, H. D. Lutz, T. Stingl, *Acta Cryst. C* **1993**, *49*, 1448–1449.

[57] J. S. Bettinger, R. V. Chopdekar, M. Liberati, J. R. Neulinger, M. Chshiev, Y. Takamura, L. M. B. Alldredge, E. Arenholz, Y. U. Idzerda, A. M. Stacy, W. H. Butler, Y. Suzuki, *J. Magn. Magn. Mater.* **2007**, *318*, 65–73.

[58] M. Esters, A. Liebig, J. J. Ditto, M. Falmbigl, M. Albrecht, D. C. Johnson, *J. Alloys Compd.* **2016**, *671*, 220–225.

[59] M. D. Anderson, J. O. Thompson, D. C. Johnson, *Chem. Mater.* **2013**, *25*, 3996–4002.

[60] C. Zhang, Y. Yan, Y. Sheng Zhao, J. Yao, *Annu. Rep. Prog. Chem., Sect. C: Phys. Chem.* **2013**, *109*, 211–239.

[61] M. L. Rao, M. Shamsuzzoha, A. Gupta, *J. Cryst. Growth* **2007**, *306*(2), 321–325.

[62] N. Daneu, A. Rečnik, T. Yamazaki, T. Dolenec, *Phys. Chem. Miner.* **2007**, *34*(4), 233–247.

[63] M. Noh, J. Thiel, D. C. Johnson, *Science* **1995**, *270*(5239), 1181–1184.

[64] C. Pang, R. Yang, A. Singh, H. Chen, M. K. Bowman, N. Bao, L. Shen, A. Gupta, *RSC Adv.* **2017**, *7*, 31173–31179.

[65] S. Q. Wang, *MRS Bull.* **1994**, *19*(8), 30–40.

[66] J. DuMond, J. P. Youtz, *J. Appl. Phys.* **1940**, *11*(5), 357–365.

[67] G. S. Chen, S. T. Chen, *J. Appl. Phys.* **2000**, *87*(12), 8473.

[68] M. A. Nicolet, *Thin Solid Films* **1978**, *52*(3), 415–443.

[69] D. Appy, M. Wallingford, D. Jing, R. Ott, M. C. Tringides, G. Richter, P. A. Thiel, *J. Vac. Sci. Technol. A* **2017**, *35*(6), 061401.

[70] A. Babitsyna, T. Emel'yanova, T. Koneshova, M. Chernitsyna, V. Kalinnikov, *Russ. J. Inorg. Chem.* **1980**, *25*, 603–604. ASM Alloy Phase Diagrams Database.

[71] F. Hulliger, *Struct. Bonding* **1968**, *4*, 83–216.

[72] G. Z. Magda, J. Petõ, G. Dobrik, C. Hwang, L. P. Biró, L. Tapasztó, *Sci. Rep.* **2015**, *5*, 3–7.

[73] M. Kertesz, R. Hoffmann, *J. Am. Chem. Soc.* **1984**, *106*(12), 3453–3460.

[74] W. Choi, N. Choudhary, G. H. Han, J. Park, D. Akinwande, Y. H. Lee, *Mater. Today* **2017**, *20*(3), 116–130.

[75] D. Voiry, A. Mohite, M. Chhowalla, *Chem. Soc. Rev.* **2015**, *44*(9), 2702–2712.

[76] M. Chhowalla, H. S. Shin, G. Eda, L.-J. Li, K. P. Loh, H. Zhang, *Nat. Chem.* **2013**, *5*(4), 263–275.

[77] H. Katzke, P. Tolédano, W. Depmeier, *Phys. Rev. B* **2004**, *69*(13), 1–8.

[78] R. E. Atkins, Dissertation, University of Oregon, **2013**.

[79] M. B. Alemayehu, M. Falmbigl, K. Ta, D. C. Johnson, *Chem. Mater.* **2015**, *27*(6), 2158–2164.

[80] J. R. Lu, E. M. Lee, R. K. Thomas, *Acta Cryst.* **1996**, *52*, 11–41.

[81] T. Brückel, D. Richter, G. Roth, A. Wischnewski, R. Zorn, *Neutron scattering*, Forschungszentrum Jülich, **2015**.

[82] Mario Birkholz, P. F. Fewster, C. Genzel, *Thin Film Analysis by X-Ray Scattering*, Wiley-VCH, **2006**.

[83] H. Kiessig, *Ann. Phys.* **1933**, *5*(10), 769–788.

[84] T. M. Phung, J. M. Jensen, D. C. Johnson, J. J. Donovan, B. G. McBurnett, *X-Ray Spectrom.* **2008**, *37*, 608–617.

[85] T. M. Phung, D. C. Johnson, G. A. Antonelli, *J. Appl. Phys.* **2006**, *100*, 063317–1–6.

[86] H. Zabel, *Appl. Phys. A.* **1994**, *58*, 159–168.

[87] C. E. Pfluger, *Anal. Chem* **1972**, *44*(5), 563–572.

[88] R. A. Cowley, T. W. Ryan, *J. Phys. D.* **1987**, *20*(1), 61–66.

[89] P. F. Fewster, *Rep. Prog. Phys.* **1996**, *59*, 1339–1407.

[90] T. Chatterji, *Neutron Scattering from Magnetic Material*, Elsevier Science, **2006**.

[91] S. J. Blundell, J. A. C. Bland, *Phys. Rev. B* **1992**, *46*(6), 3391–3400.

[92] J. F. Ankner, G. P. Felcher, *J. Magn. Magn. Mater.* **1999**, *200*, 741–754.

[93] Q. Liang, J. Liu, Z. Cheng, Y. Li, L. Chen, R. Zhang, J. Zhang, Y. Han, *J. Mater. Chem. A* **2016**, *4*(1), 223–232.

[94] D. R. Merrill, D. B. Moore, M. N. Coffey, A. W. Jansons, M. Falmbigl, D. C. Johnson, *Semicond. Sci. Technol.* **2014**, *29*(6), 064004.

[95] G. Mitchson, M. Falmbigl, J. Ditto, D. C. Johnson, *Inorg. Chem.* **2015**, *54*(21), 10309–10315.

[96] C. L. Heideman, R. Rostek, M. D. Anderson, A. a. Herzing, I. M. Anderson, D. C. Johnson, *J. Electron. Mater.* **2010**, *39*(9), 1476–1481.

[97] M. M. Smeller, C. L. Heideman, Q. Lin, M. Beekman, M. D. Anderson, P. Zschack, I. M. Anderson, D. C. Johnson, *Z. anorg. allg. Chem.* **2012**, *638*(15), 2632–2639.

[98] A. C. Lygo, D. M. Hamann, D. B. Moore, D. R. Merrill, J. Ditto, M. Esters, J. Orlowicz, S. R. Wood, D. C. Johnson, *J. Am. Chem. Soc.* **2018**, *140*(9), 3385–3393.

[99] M. Falmbigl, M. B. Alemayehu, D. R. Merrill, M. Beekman, D. C. Johnson, *Cryst. Res. Technol.* **2015**.

[100] G. A. Wiegers, A. Meetsma, R. J. Haange, J. Wulff, J. L. de Boer, S. Kuypers, G. Van Tendeloo, J. Van Landuyt, S. Amelinckx, A. Meersehaut, P. Rabu, J. Rouxel, *Solid State Commun.* **1989**, *70*(4), 409–413.

[101] I. Häusler, R. Atkins, M. Falmbigl, S. P. Rudin, W. Neumann, D. C. Johnson, *Z. Kristallogr.* **2015**, *230*(1), 45–54.

[102] D. M. Hamann, D. R. Merrill, S. R. Bauers, G. Mitchson, J. Ditto, S. P. Rudin, D. C. Johnson, *Inorg. Chem.* **2017**, *56*(6), 3499–3505.

[103] R. Atkins, M. Dolgos, A. Fiedler, C. Grosse, S. F. Fischer, S. P. Rudin, D. C. Johnson, *Chem. Mater. Mater.* **2014**, *26*, 2862–2872.

[104] O. K. Hite, M. Falmbigl, M. B. Alemayehu, M. Esters, S. R. Wood, D. C. Johnson, *Chem. Mater.* **2017**, *29*(13), 5646–5653.

[105] D. B. Moore, M. Beekman, S. Disch, P. Zschack, I. Häusler, W. Neumann, D. C. Johnson, *Chem. Mater.* **2013**, *25*, 2404–249.

[106] C. L. Heideman, S. Tepfer, Q. Lin, R. Rostek, P. Zschack, M. D. Anderson, I. M. Anderson, D. C. Johnson, *J. Am. Chem. Soc.* **2013**, *135*(30), 11055–11062.

[107] M. D. Anderson, C. L. Heideman, Q. Lin, M. Smeller, R. Kokenyesi, A. a. Herzing, I. M. Anderson, D. a. Keszler, P. Zschack, D. C. Johnson, *Angew. Chem. Int. Ed* **2013**, *125*, 2036–2039.

[108] M. Falmbigl, A. Fiedler, R. E. Atkins, S. F. Fischer, D. C. Johnson, *Nano Lett.* **2015**, *15*, 943–948.

[109] D. M. Hamann, A. C. Lygo, M. Esters, D. R. Merrill, J. Ditto, D. R. Sutherland, S. R. Bauers, D. C. Johnson, *ACS Nano* **2018**, *12*(2), 1285–1295.

[110] S. P. Rudin, D. C. Johnson, *Phys. Rev. B* **2015**, *91*(14), 144203.

[111] E. von Horschek, W. Klemm, *Z. anorg. allg. Chem.* **1939**, *242*, 49–62.

[112] C. Riekel, *J. Solid State Chem.* **1976**, *17*(4), 389–392.

[113] I. S. Braude, A. A. Mamalui, O. N. Onishko, *J. Alloys Compd.* **2009**, *486*(1-2), 859–863.

[114] M. Bremholm, Y. S. Hor, R. J. Cava, *Solid State Sci.* **2011**, *13*(1), 38–41.

[115] M. Falmbigl, D. Putzky, J. Ditto, M. Esters, S. R. Bauers, F. Ronning, D. C. Johnson, *ACS Nano* **2015**, *9*(8), 8440–8448.

[116] T. Chattopadhyay, J. Pannetier, H. G. Von Schnering, *J. Phys. Chem. Solids* **1986**, *47*(9), 879–885.

[117] M. B. Alemayehu, M. Falmbigl, K. Ta, C. Grosse, R. D. Westover, S. R. Bauers, S. F. Fischer, D. C. Johnson, *Chem. Mater.* **2015**, *27*, 867–875.

[118] D. B. Moore, M. Beekman, S. Disch, D. C. Johnson, *Angew. Chem. Int. Ed* **2014**, *126*(22), 5778–5781.

[119] I. V. Golosovsky, M. Tovar, U. Hoffman, I. Mirebeau, F. Fauth, D. a. Kurdyukov, Y. a. Kumzerov, *JETP Letters* **2006**, *83*(7), 298–301.

[120] M. Esters, Dissertation, University of Oregon, **2017**.

[121] A. Le Bail, H. Duroy, J. Fourquet, *Mater. Res. Bull.* **1988**, *23*(3), 447–452.

[122] G. Wiegers, *Physica B+C* **1980**, *99*(1-4), 151–165.

[123] G. C. Tewari, M. Karppinen, A. K. Rastogi, *J. Solid State Chem.* **2013**, *198*, 108–113.

[124] L. M. Kulikov, A. A. Semjonov-Kobzar, M. M. Antonova, A. A. Chechovsky, L. G. Akselrud, R. V. Skolozdra, D. Fruchart, J. L. Soubeyroux, *J. Alloys Compd.* **1996**, *244*(96), 11–15.

[125] J. V.-v. D. Berg, R. Sherwood, *J. Phys. Chem. Solids* **1971**, *32*, 167–173.

[126] N. S. Gunning, T. Dankwort, M. Falmbigl, U. Ross, G. Mitchson, D. M. Hamann, A. Lotnyk, L. Kienle, D. C. Johnson, *Chem. Mater.* **2017**, *29*(19), 8292–8298.

[127] G. E. Lloyd, *Mineralogical Magazine* **1987**, *51*, 3–19.

[128] C. Grosse, M. B. Alemayehu, M. Falmbigl, A. Mogilatenko, O. Chiatti, D. C. Johnson, S. F. Fischer, *Sci. Rep.* **2016**, *6*, 33457.

[129] Z. Liu, Z. Fei, C. Xu, Y. Jiang, X.-L. Ma, H.-M. Cheng, W. Ren, *Nanoscale* **2017**, *9*, 7501–7507.

[130] S. Susarla, J. A. Hachtel, X. Yang, A. Kutana, A. Apte, Z. Jin, R. Vajtai, J. C. Idrobo, J. Lou, B. I. Yakobson, C. S. Tiwary, *Adv. Mater.* **2018**, *1804218*, 1–6.

[131] S. Singh, N. Khare, *Appl. Surf. Sci.* **2016**, *364*, 783–788.

[132] S. Kattel, G. Wang, *J. Chem. Phys.* **2014**, *141*(12).

[133] P. Strasser, S. Koh, T. Anniyev, J. Greeley, K. More, C. Yu, Z. Liu, S. Kaya, D. Nordlund, H. Ogasawara, M. F. Toney, A. Nilsson, *Nat. Chem.* **2010**, *2*(6), 454–460.

[134] H. Huang, H. Jia, Z. Liu, P. Gao, J. Zhao, Z. Luo, J. Yang, J. Zeng, *Angew. Chem. Int. Ed* **2017**, 3594–3598.

[135] A. Mayence, M. Wéry, D. T. Tran, E. Wetterskog, P. Svedlindh, C.-W. Tai, L. Bergström, *Nanoscale* **2016**, *8*, 14171–14177.

[136] N. Pathak, S. K. Gupta, C. L. Prajapat, S. K. Sharma, P. S. Ghosh, B. Kanrar, P. K. Pujari, R. M. Kadam, *Phys. Chem. Chem. Phys.* **2017**, *19*(19), 11975–11989.

[137] L. Dubau, J. Nelayah, S. Moldovan, O. Ersen, P. Bordet, J. Drnec, T. Asset, R. Chattot, F. Maillard, *ACS Catalysis* **2016**, *6*(7), 4673–4684.

[138] X. Huang, W. Yang, R. Harder, Y. Sun, M. Lu, Y. S. Chu, I. K. Robinson, H. K. Mao, *Nano Letters* **2015**, *15*(11), 7644–7649.

[139] S. K C, C. Zhang, S. Hong, R. M. Wallace, K. Cho, *2D Materials* **2015**, *2*(3), 035019.

[140] C. Cepeda-Jiménez, J. Beltrán, A. Hernando, M. García, F. Ynduráin, A. Zhilyaev, M. Pérez-Prado, *Acta Mater.* **2017**, *123*, 206–213.

[141] D. Srivastava, G. C. Tewari, M. Karppinen, *J. Phys.: Condens. Matter* **2014**, *26*(50), 505501.

[142] C. F. van Bruggen, R. J. Haange, G. A. Wiegers, D. K. G. de Boer, *Physica B+C* **1980**, *99*(1-4), 166–172.

[143] D. C. Freitas, M. Núñez, P. Strobel, A. Sulpice, R. Weht, A. A. Aligia, M. Núñez-Regueiro, *Phys. Rev. B* **2013**, *87*(1), 1–9.

[144] R. Atkins, J. Wilson, P. Zschack, C. Grosse, W. Neumann, D. C. Johnson, *Chem. Mater.* **2012**, *24*(23), 4594–4599.

[145] S. R. Wood, D. R. Merrill, M. Falmbigl, D. B. Moore, J. Ditto, M. Esters, D. C. Johnson, *Chem. Mater.* **2015**, *27*(17), 6067–6076.

[146] C. A. F. Vaz, J. A. C. Bland, G. Lauhoff, *Rep. Prog. Phys.* **2008**, *71*(5), 056501.

[147] S. M. Clarke, D. E. Freedman, *Inorg. Chem.* **2015**, *54*(6), 2765–2771.

[148] Y. Koh, S. Cho, J. Lee, L.-X. Yang, Y. Zhang, C. He, F. Chen, D.-L. Feng, M. Arita, K. Shimada, H. Namatame, M. Taniguchi, C. Kim, *Jpn. J. Appl. Phys., Part 1* **2013**, *52*(10S), 10MC15.

[149] G. C. Tewari, T. S. Tripathi, A. K. Rastogi, *eprint arXiv:1109.1071* **2011**, 1–9.

[150] M. Beekman, G. Rodriguez, R. Atkins, J. Kunert, D. B. Moore, D. C. Johnson, *J. Appl. Phys.* **2015**, *117*(18).

[151] L. Zhang, J. Fan, X. Zhu, W. Ning, Z. Qu, M. Ge, L. Pi, Y. Zhang, *Appl. Phys. A* **2013**, *113*(1), 201–206.

[152] P. S. Behera, P. A. Bhobe, A. K. Nigam, in *DAE Solid State Physics Symposium 2015*, 130009–1–3.

[153] K. Ramasamy, H. Sims, S. Keshavarz, N. Naghibolashrafi, A. Gupta, *J. Mater. Chem. C* **2016**, *4*(16), 3628–3639.

[154] V. N. Berzhansky, N. A. Drokin, V. I. Ivanov, V. P. Kononov, I. S. Edelman, S. A. Havrichkov, V. K. Chernov, A. G. Shishkov, A. M. Pirogova, *Thin Solid Films* **1990**, *190*, 199–215.

[155] F. K. Lotgering, R. P. Stapele, *Solid State Commun.* **1967**, *5*, 143–146.

[156] I. Nakatani, H. Nose, K. Masumoto, *J. Phys. Chem. Solids* **1978**, *39*, 743–749.

[157] M. Robbins, H. Lehmann, J. White, *J. Phys. Chem. Solids* **1967**, *28*(6), 897–902.

[158] T. Kanomata, I. Hideaki, *J. Phys. Soc. Jpn.* **1970**, *29*(2), 332–335.

[159] L. Zhang, L. Ling, J. Fan, R. Li, S. Tan, Y. Zhang, *J. Appl. Phys.* **2011**, *109*(11), 113911.

[160] Y.-H. Wang, Dissertation, University of Alabama, **2010**.

[161] Y.-H. A. Wang, N. Bao, L. Shen, P. Padhan, A. Gupta, *J. Am. Chem. Soc.* **2007**, *129*(41), 12408–12409.

[162] A. I. Pankrats, A. M. Vorotynov, V. I. Tugarinov, S. M. Zharkov, D. A. Velikanov, G. M. Abramova, G. M. Zeer, K. Ramasamy, A. Gupta, *J. Appl. Phys.* **2014**, *116*(5), 054302.

[163] J. B. Goodenough, *Solid State Commun.* **1967**, *5*(8), 577–580.

[164] C. Colominas, *Phys. Rev.* **1967**, *153*(2), 558–560.

[165] H. Yokoyama, R. Watanabe, *J. Phys. Soc. Jpn.* **1967**, *23*, 450.

[166] A. Kimura, J. Matsuno, J. Okabayashi, A. Fujimori, T. Shishidou, E. Kulatov, T. Kanomata, *Phys. Rev. B* **2001**, *63*(22), 2244201–2244207.

[167] Y. H. Wang, A. Gupta, M. Chshiev, W. H. Butler, *App. Phys. Lett.* **2008**, *92*(6), 2–5.

[168] M. Liberati, J. R. Neulinger, R. V. Chopdekar, J. S. Bettinger, E. Arenholz, W. H. Butler, A. M. Stacy, Y. I. Idzerda, Y. Suzuki, *J. Appl. Phys.* **2008**, *103*(7), 2–5.

[169] T. Saha-Dasgupta, M. De Raychaudhury, D. D. Sarma, *Phys. Rev. B* **2007**, *76*(5), 054441.

[170] S. Bordács, I. Kézsmárki, K. Ohgushi, Y. Tokura, *New J. Phys.* **2010**, *12*.

[171] M. Winterberger, Y. Allain, *Solid State Commun.* **1987**, *64*(11), 1343–1346.

[172] G. C. Tewari, T. S. Tripathi, H. Yamauchi, M. Karppinen, *Mater. Chem. Phys.* **2014**, *145*(1-2), 156–161.

[173] G. C. Tewari, M. Karppinen, A. K. Rastogi, *J. Solid State Chem.* **2013**, *198*, 108–113.

[174] C. M. Fang, C. F. van Bruggen, R. A. de Groot, G. A. Wiegers, C. Haas, *J. Phys.: Condens. Matter* **1997**, *9*(46), 10173–10184.

[175] J. Sugiyama, H. Nozaki, I. Umegaki, T. Uyama, K. Miwa, J. H. Brewer, S. Kobayashi, C. Michioka, H. Ueda, K. Yoshimura, *Phys. Rev. B* **2016**, *94*(1), 1–5.

[176] D. Srivastava, G. C. Tewari, M. Karppinen, R. M. Nieminen, *J. Phys.: Condens. Matter* **2013**, *25*(10), 105504.

[177] A. Gagor, D. Gnida, A. Pietraszko, *Mater. Chem. Phys.* **2014**, *146*(3), 283–288.

[178] P. Bongers, C. Van Bruggen, J. Koopstra, W. Omloo, G. Wiegers, F. Jellinek, *J. Phys. Chem. Solids* **1968**, *29*(6), 977–984.

[179] H. Y. Lv, W. J. Lu, D. F. Shao, Y. Liu, Y. P. Sun, *Phys. Rev. B* **2015**, *92*(21), 1–8.

[180] A. Zameshin, I. A. Makhotkin, S. N. Yakunin, R. W. E. van de Kruijs, A. E. Yakshin, F. Bijkerk, *J. Appl. Cryst.* **2016**, *49*, 1300–1307.

[181] O. Balmes, R. van Rijn, D. Wermeille, A. Resta, L. Petit, H. Isern, T. Dufrane, R. Felici, *Catal. Today* **2009**, *145*(3-4), 220–226.

[182] J. Drnec, T. Zhou, S. Pintea, W. Onderwaater, E. Vlieg, G. Renaud, R. Felici, *J. Appl. Cryst.* **2014**, *47*(1), 365–377.

[183] S. Roobol, W. Onderwaater, J. Drnec, R. Felici, J. Frenken, *J. Appl. Cryst.* **2015**, *48*(4), 1–6.

[184] S. Mattauch, A. Koutsioubas, S. Pütter, *J. large-scale research facilities* **2015**, *8*(1), 1–4.

[185] M. Schaffer, B. Schaffer, Q. Ramasse, *Ultramicroscopy* **2012**, *114*, 62–71.

[186] R. M. Langford, M. Rogers, *Micron* **2008**, *39*, 1325–1330.

[187] C. A. Schneider, W. S. Rasband, K. W. Eliceiri, *Nat. Methods* **2012**, *9*(7), 671–675.

[188] H. M. Rietveld, *J. Appl. Cryst.* **1969**, *2*, 65–71.

[189] A. Larson, R. Von Dreele, *General Structure Analysis System (GSAS)*, **2000**.

[190] B. H. Toby, *J. Appl. Cryst.* **2001**, *34*(2), 210–213.

Eidesstattliche Erklärung

Ich versichere, dass ich die von mir vorgelegte Dissertation selbständig angefertigt, die benutzten Quellen und Hilfsmittel vollständig angegeben und die Stellen der Arbeit - einschließlich Tabellen, Karten und Abbildungen -, die anderen Werken im Wortlaut oder dem Sinn nach entnommen sind, in jedem Einzelfall als Entlehnung kenntlich gemacht habe; dass diese Dissertation noch keiner anderen Fakultät oder Universität zur Prüfung vorgelegen hat; dass sie - abgesehen von unten angegebenen Teilpublikationen - noch nicht veröffentlicht worden ist sowie, dass ich eine solche Veröffentlichung vor Abschluss des Promotionsverfahrens nicht vornehmen werde. Die Bestimmungen der Promotionsordnung sind mir bekannt. Die von mir vorgelegte Dissertation ist von Dr. Sabrina Disch betreut worden

Köln, 20th August 2019

(Ort, Datum)

(Unterschrift)